UNICA

UNIVERSITÀ
DEGLI STUDI
DI CAGLIARI

Ph.D. DEGREE IN
Electronic and Computer Engineering

Cycle XXXVII

TITLE OF THE Ph.D. THESIS

Cooperative Hoisting with Dual Crawler Cranes:
Modeling, Motion Planning, and Control under Constraints

Scientific Disciplinary Sector(s)

ING-INF/04

Ph.D. Student:	Chenhao Cui
Supervisor	Prof. Alessandro Giua
Co-Supervisor	Prof. Alessandro Pisano

Final exam. Academic Year 2023/2024
Thesis defence session: February 2026

ABSTRACT

With the rapid development of large scale infrastructure construction and industrial assembly such as wind turbine installation, bridge segment erection, and modular plant construction dual crawler cranes (DCCs) have become essential equipment for handling oversized and heavy loads. Their cooperative hoisting capability enables the manipulation of massive structures beyond the lifting capacity of a single crane. However, due to the cooperative hoisting of DCCs represents a complex nonlinear control problem characterized by strong coupling, underactuation, and multiple motion constraints. Ensuring safe, efficient, and precise load manipulation in such systems poses significant challenges, particularly when considering the bounded nature of rope velocities and the closed chain geometric configuration formed by the cranes and the suspended load.

This thesis investigates the modeling, trajectory design, and control of DCC cooperative hoisting systems with two types of suspended loads: a point-mass load and a rigid-rod load.

For the point-mass case, a comprehensive kinematic model is developed to describe the motion under cable velocity constraints. To achieve time optimal lifting while respecting the rope-velocity bounds, an optimal control method is proposed to minimize the total hoisting duration under physical constraints. Building upon this, an adaptive velocity shaping technique is introduced, which dynamically adjusts the motion speed based on the instantaneous position of the load and the cable dynamic factors. This adaptive mechanism guarantees constraint satisfaction while maintaining high motion efficiency and smooth deceleration as the load approaches the target position, thereby further reducing the total lifting time.

For the rigid-rod load system, a complete nonlinear dynamic model is established without linearization assumptions. Through systematic constraint reduction, the original tenth-order (5 degree of freedom) dynamic model is reduced to a simplified sixth-order (3 degree of freedom) representation that retains essential nonlinear behaviors. This formulation provides an accurate yet tractable foundation for controller design and serves as a reference for similar closed chain mechanical systems. Stability of the closed loop system is analytically verified through both linearized and energy based approaches.

A constraint consistent trajectory generation method is then proposed, in which reference trajectories are directly designed in the cable length domain. By determining the equilibrium configuration at each instant through the system's balance equations, the approach ensures that all reference trajectories inherently satisfy static equilibrium and geometric feasibility. On this basis, a PID-based coupled error compensation control scheme is developed to coordinate the

motions of the two cranes while suppressing load sway. The controller integrates synchronization and attitude error compensation to achieve cooperative stability and high-precision tracking.

Extensive simulation studies are conducted in MATLAB to validate the effectiveness of the proposed models and control strategies. The results demonstrate that the developed methods ensure precise trajectory tracking, strong robustness to system asymmetry, and significant improvements in lifting efficiency and vibration suppression.

Keywords: Dual crawler cranes, Cooperative hoisting, Nonlinear dynamics, Trajectory planning and control, Nonlinear modeling

Contents

List of Figures

List of Tables

Chapter 1

Introduction

1.1 Research Motivation

1.1.1 Background on Crawler Cranes

Crawler cranes as illustrated in Fig. 1.1, are mobile lifting machines designed for heavy duty operations. The *boom* length and *boom angle* of the crawler crane can be adjusted to meet different lifting requirements, and the *turntable* allows full 360-degree rotation to expand the operating range. The *cable* length can be varied to raise or lower the suspended load, while the *crawler* enables the crane to move steadily and adapt to uneven terrain, ensuring strong mobility and stability in demanding working environments. Crawler cranes are widely used in the construction of large-scale infrastructures such as power plants, bridges, petrochemical facilities, stadiums, and nuclear installations [1, 2]. Their high load capacity, operational stability, and flexible boom configuration provide distinct structural advantages that make them well suited for demanding engineering applications [3]. With the continuous development of these industries, the geometry, mass, and installation precision of lifted components have become increasingly complex [4].

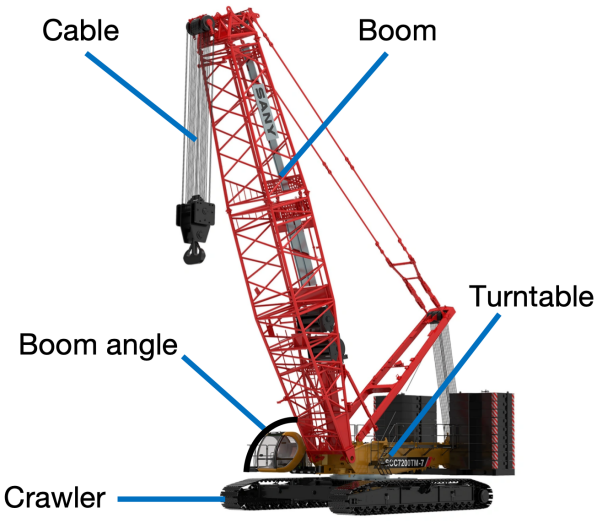

Figure 1.1: Schematic of a crawler crane (SANY SCC7200TM).

For high precision operations such as the installation of wind turbine blades or bridge

girders, a single crane often proves inadequate due to its limited load capacity and inability to regulate the load orientation [5]. Consequently, dual crawler cranes (DCCs) cooperative hoisting has become a necessary solution. However, this collaborative operation introduces considerable challenges, as it requires precise coordination between cranes and increases the overall risk and complexity of the lifting task. In conventional practice, the lifting path is often determined through manual adjustments near the installation site, relying heavily on the experience of multiple skilled operators. This approach is time consuming and prone to uncertainties, which significantly reduces operational efficiency [6].

Furthermore, the demand for high capacity cranes continues to rise in large scale industrial applications, pushing manufacturers to expand the lifting limits of single cranes. Yet, beyond a certain threshold, enhancing the load capacity of a single crane entails a disproportionate increase in cost and design difficulty [7]. In contrast, cooperative lifting using two or more medium capacity crawler cranes has become an economically and technically viable alternative. This configuration allows heavy or oversized structures to be lifted with improved stability while maintaining cost efficiency [8].

1.1.2 Advantages of DCC Systems

The advantages of DCC systems over single crane operations can be summarized as follows:

- **Higher load capacity:** DCCs can share the total load, enabling the lifting of heavier and larger structures that exceed the capacity limits of a single crane.
- **Improved operational stability:** Load distribution between the cranes reduces tipping risk, lateral swing, and excessive boom stress, thereby enhancing overall safety and stability during lifting.
- **Enhanced orientation control:** Coordinated motion of both cranes allows precise adjustment of the load's attitude and position, which is essential in high precision assembly tasks such as wind turbine installation.
- **Cost effectiveness:** Using two medium capacity cranes is often more economical than manufacturing or deploying a single ultra heavy crane with equivalent capacity.
- **Greater flexibility and adaptability:** DCC systems can accommodate a wider range of lifting configurations and operate effectively in confined or irregular workspaces.

A typical example is the installation of high power wind turbines. The blades of a modern turbine, which can exceed 30 meters in length, must be hoisted from a horizontal transport position to a precise vertical alignment for hub assembly [6]. This operation typically requires

the synchronized motion of DCCs to achieve both load sharing and accurate orientation control. Similarly, in petrochemical plant construction, the lifting of large distillation columns and reactor vessels often relies on DCC cooperation to ensure safe and accurate positioning.

The complexity of their mechanical structure, particularly the boom system, results in a strong dependency of lifting performance on boom length and working radius [9–12]. When two crawler cranes are coupled in cooperative operation, this complexity increases further because the motion of one crane directly affects the stability and balance of the entire load system [11–15]. As the construction industry moves toward automation and intelligent operation, the automatic coordinated control of DCC systems has become an inevitable trend to enhance safety, precision, and efficiency in modern lifting operations [16].

1.1.3 Practical Challenges and Safety Issues

In current industrial practice, DCC cooperative hoisting faces multiple challenges. First, the closed kinematic chain formed between the cranes and the lifted load increases the complexity of the system dynamics [17]. Second, the suppression of load swing and the achievement of precise positioning during lifting require highly synchronized motion of the two cranes. In addition, obstacle avoidance and motion path planning in complex industrial environments further increase operational difficulty [18]. These issues make traditional manual operation inadequate to meet the modern requirements of lifting precision and efficiency, which has accelerated the development of automated and intelligent hoisting technologies.

Conventional DCC cooperative hoisting operations mainly rely on manual coordination, where several operators work under the guidance of a supervisor. This approach presents several critical limitations, including low efficiency, poor synchronization, and high safety risk. Operators often rely on visual estimation from long distances or elevated positions, making it difficult to accurately perceive the real time load motion and position [19]. As a result, the lifting process becomes time consuming and error prone. More importantly, manual operation cannot ensure perfect synchronization between cranes. Variations in operator response time and control habits may cause undesirable load sway, deviation, or even overload, posing serious safety hazards.

The limitations of manual control become even more evident in complex lifting tasks that require precise load attitude regulation or movement through confined spaces. Under such conditions, operator workload and psychological stress significantly increase, which further reduces operation reliability and safety [20].

The practical challenges of dual crane coordination have been confirmed by recent engineering accidents. The investigation of the 2024 Shanghai Metro Line 11 crawler crane accident revealed that poor coordination between the two cranes was one of the primary causes of

the incident. The accident site is shown in Fig. 1.2. Specifically, the operation sites and the selection of the 260-ton and 320-ton crawler cranes were inconsistent with the planned lifting scheme. During the 25 minute operation, the two cranes failed to maintain proper synchronization. The 320-ton crane performed almost no cooperative movement, while the 260-ton crane rotated and traveled independently several times, producing excessive lateral forces during the process. This case highlights the limitations of current DCC cooperative hoisting in real world engineering applications.

Figure 1.2: Photograph of the 2024 Shanghai Metro Line 11 crawler crane accident site.

Beyond safety and efficiency concerns, traditional dual crane hoisting also encounters computational and planning challenges. Generating accurate lifting capacity charts requires large scale data processing and significant computational effort. Simplified analytical models and manual calculations often lead to low accuracy and heavy workload, compromising the safety and reliability of the lifting plan [21]. In the case of DCC systems, these challenges are further amplified because both cranes' performance characteristics and their cooperative relationship must be simultaneously considered.

1.1.4 Research Gaps and Academic Motivation

Although extensive research has been conducted on crane control in the academic community, existing studies still exhibit limitations when applied to DCC cooperative hoisting. The control of a single crane has been relatively well developed, with mature results in swing suppression and precise positioning [22]. For instance, adaptive anti sway control strategies have been proposed for three dimensional double pendulum overhead cranes with variable rope lengths to address critical issues such as excessive motor starting torque, system parameter uncertainty, and large swing angles of the hook and load during motion [23].

Other studies have introduced anti-sway control methods for container cranes with variable rope lengths based on phase plane trajectory planning [24]. This approach employs linear approximation to handle time varying systems that lack exact analytical solutions, providing an

effective framework for anti-sway control under complex cooperative conditions.

In the field of dual crane coordination, some research has focused on dual hoisting bridge cranes and proposed control methods combining time varying hierarchical incremental sliding-mode control with adaptive compensation [25]. However, these studies primarily concern bridge cranes or gantry cranes operating along fixed rails, while the cooperative hoisting of crawler cranes has received limited attention.

The modeling complexity of DCC systems is substantially higher than that of bridge cranes because of the increased degrees of freedom and more intricate dynamic characteristics. Furthermore, several key constraints in dual crane cooperative operations have not been sufficiently considered in the existing literature. The closed chain constraint formed between the two cranes and the suspended load significantly increases the difficulty of motion planning. During cooperative lifting, additional coupling constraints such as load distribution, motion synchronization, and collision avoidance must also be addressed to ensure safe and efficient operation.

Regarding load attitude control, several studies have applied the principle of angular momentum exchange to the attitude regulation of suspended objects in space. By varying the angular velocity and acceleration of flywheels, these methods can adjust the horizontal rotation of the suspended payload. However, their effectiveness in DCC cooperative hoisting remains to be verified [26].

Fuzzy PID control has been proven effective in lifting scenarios where the payload mass frequently changes, yet its adaptability to dual crane cooperative systems requires further investigation [27]. Notably, research on tower crane applications has shown that fuzzy PID control may suffer from poor performance due to the limited reliability of expert rules, excessive uncertainty within the fuzzy structure, and inherent blindness in rule definition. These limitations could become even more pronounced in the more complex DCC systems [28].

To overcome the deficiencies of traditional fuzzy PID control, an adaptive PID strategy combining an *improved seagull optimization algorithm* (ISOA) and *neural networks* (NN) has been proposed by Tang *et al.* [28]. This approach optimizes the initial neural network weights and adjusts the PID parameters online, thereby enhancing robustness against load variation and external disturbances. These findings indicate that integrating advanced optimization algorithms with adaptive control techniques could significantly improve control performance in complex crane systems.

Nevertheless, existing control approaches still face challenges in handling system nonlinearity and uncertainty. Research on overhead crane systems shows that most cranes remain heavily dependent on manual operation, with efficiency relying entirely on operator expertise. In practical applications, automatic control is constrained by parameter uncertainty and unmodeled dynamics. For dual crane systems, the strong nonlinear coupling between subsystems makes controller design even more complicated [29–31]. Studies on dual hoisting synchro-

nization reveal that, when frequency converters cannot communicate in real time, asynchronous motor motion may generate impact loads on the braking system. Similar synchronization issues are likely to be more severe in DCC systems [32].

In summary, current research on DCC cooperative hoisting still presents several critical gaps. First, investigations on the cooperative operation of mobile cranes remain limited. Second, key constraint conditions within the system are often not sufficiently modeled. Third, the adaptability of existing control methods to complex dual crane configurations has not been fully validated. Finally, few studies have provided effective solutions to address nonlinearities, parameter uncertainties, and communication delays that occur in real engineering applications. These research gaps define important directions for future academic exploration [33, 34].

1.2 Background and Literature Review

1.2.1 Cooperative Hoisting System

The research on multi crane cooperative systems began in the 1990s, with early studies focusing primarily on fundamental issues such as task coordination and load distribution. Souissi *et al.* [35] and Wang *et al.* [36] were among the first to investigate task allocation strategies for multi crane systems, proposing optimization methods to maximize crane utilization and minimize operational conflicts. These pioneering studies established a theoretical foundation for cooperative lifting but remained largely at the planning level without addressing the challenges of real time dynamic control.

With the advancement of control theory and sensing technology in the current century, research on multi crane systems gradually shifted toward dynamic coordination and control. Drawing inspiration from cooperative manipulator technology, scholars analyzed the differences between dual crane systems and dual manipulator structures, defined several typical modes of cooperative hoisting, and formulated corresponding coordination equations. Based on these theoretical developments, hardware systems utilizing wireless communication were designed to enable real time information exchange between cranes and the lifted load. These systems successfully integrated cooperative control algorithms and achieved experimental validation. This evolution marked a significant transition of multi-crane systems from static planning under human supervision to automated and information driven dynamic coordination control [37].

As a specialized form of cooperative operation, the DCC system follows a similar developmental path but exhibits distinctive technical characteristics. The crawler undercarriage provides high mobility and expands the working range, yet it also introduces new complexities such as ground unevenness and crawler soil interaction dynamics [38]. Furthermore, compared

with *dual rotary cranes* (DRCs), the cooperative control of DCCs is inherently more challenging due to the nonlinear coupling between the two cranes and the additional constraints introduced by ground contact and motion coordination [39, 40].

Cai *et al.* [41] clearly pointed out in their study on path planning for dual crane cooperative hoisting that the dual crane system forms a closed kinematic chain, and the motion of the suspended load exhibits strong nonlinearity that depends critically on the coordination between the two cranes. The study divided the dual crane system into two subsystems: a manipulator subsystem, which includes the active swing and pitch motion of the crane booms, and a suspension subsystem, which involves the passive swing dynamics of the cables and the suspended load. This modeling framework provides an important theoretical basis for understanding the dynamic behavior and control design of complex crane systems, including DCC systems.

The study further emphasized that treating the system as two independent cranes while neglecting cooperative constraints during planning and control leads to unsafe trajectories and poor coordination. This conclusion is equally valid for DCC cooperative hoisting. In the practical implementation of such systems, coordination plays a vital role in ensuring operational safety. Any lack of synchronization between the two cranes can easily induce severe load swing, which may result in excessive cable tension or even structural damage to the cranes.

For crawler cranes in particular, the unevenness of the ground and other environmental uncertainties during motion can introduce additional kinematic discrepancies, making coordinated control even more challenging. Therefore, motion synchronization, load stability, and operational safety constitute the three primary objectives in the research and optimization of DCC systems.

1.2.2 Dynamic Modeling Methods

Accurate dynamic modeling of DCC systems serves as the foundation for control system design and remains one of the major challenges in this research field. The system involves multiple rigid and flexible bodies, including the crane structure, booms, cables, and the suspended load, together with complex kinematic and dynamic constraints. As a result, the modeling process is considerably more complicated than that of a single crane system.

Among various modeling approaches, the *Lagrangian formulation* is one of the most widely used methods for the dynamic analysis of crane systems. By establishing the equations of motion from the system's energy relationships, it effectively handles systems with multiple constraints and nonlinear couplings [42]. The study by Liu *et al.* [40] on DRCs provides an important reference for the modeling of DCC systems. This nonlinear dynamic modeling approach, based on the complete Euler–Lagrange equations, can also be effectively applied to DCC cooperative hoisting to describe its coupled mechanical behavior and dynamic

interactions.

The DCC system is a strongly coupled structure that integrates boom motion and load swing. Large amplitude load oscillations generate dynamic moments that significantly affect the overall stability of the system [43, 44]. In this context, the kinematic coupling trajectory planning method proposed by Li *et al.* [45] is particularly important. For DCC cooperative hoisting, trajectory planning must not only suppress the double pendulum effect but also incorporate stability related constraints such as center of gravity envelope and ground pressure distribution as hard conditions in the optimization algorithm [46]. The goal is to generate an optimal trajectory that achieves both precise positioning and absolute operational safety [37, 47–49].

Large crawler cranes usually employ lattice type booms, whose structural flexibility cannot be neglected. This introduces a higher dimensional coupled vibration problem involving a rigid body, flexible boom, cable, and suspended load. The flexible deformation of the boom interacts with the double pendulum oscillation of the load, resulting in complex vibration modes. Consequently, models based solely on rigid-rod assumptions, such as basic double pendulum approximations, fail to capture the true dynamic characteristics of the system.

To address this challenge, Maleki *et al.* [50] proposed a two mode input shaper for double pendulum cranes, which provides an important reference for further developments. For DCC systems, it may be necessary to design multi mode input shapers capable of simultaneously suppressing boom structural vibrations and load swing oscillations. In model based control design, the dynamic equations must include the flexible degrees of freedom of the boom to accurately describe and regulate system behavior.

Accurate modeling of DCC systems therefore requires the integration of traditional double pendulum dynamics with the dynamics of the mobile base, ground interaction, and structural flexibility. This represents a complex rigid flexible coupled multibody dynamics problem. The advanced modeling and control methods developed for fixed base cranes provide a solid theoretical foundation, but further extensions and innovations are essential to address the unique engineering challenges of DCC cooperative hoisting.

Different modeling approaches for dual crane systems emphasize different aspects of system dynamics, with an evident trade off between model accuracy and computational efficiency. As summarized in Table 1.1 , common modeling techniques include the *Lagrangian method*, the *Newton–Euler method*, *Kane's method*, and the *geometric mechanics approach*. The Lagrangian method provides a systematic framework and handles constraints effectively, but it is computationally intensive and highly sensitive to parameter variations, making it more suitable for high-fidelity simulation and precise control analysis. The Newton–Euler method is physically intuitive and computationally efficient, yet it becomes cumbersome when dealing with complex constraints, and is therefore often applied in real-time control and dynamic computation. Kane's method eliminates the need to calculate internal forces and is well suited

for multibody dynamic analysis, although its derivation is relatively complex. The geometric mechanics approach focuses on preserving the system's geometric structure, requires rigorous mathematical formulation, and is mainly employed in theoretical analysis and control design.

Table 1.1: Comparison of modeling methods for dual crane systems.

Modeling Method	**Advantages**	**Limitations**	**Applicable Scenarios**
Lagrangian Method	Strong systematic formulation and convenient handling of constraints	Computationally complex and sensitive to parameters	High-precision control and simulation analysis
Newton–Euler Method	Physically intuitive and computationally efficient	Complex constraint handling	Real-time control and dynamic computation
Kane's Method	Avoids internal force calculations	Complex derivation process	Multibody system dynamics analysis
Geometric Mechanics Method	Preserves the geometric structure of the system	Requires high mathematical background	Theoretical analysis and control design

Although energy based methods such as the Lagrangian formulation can produce high-fidelity dynamic models, the resulting complex differential equations and coupling terms impose a significant computational burden, which limits their applicability in real-time control. Consequently, practical engineering applications often require a trade off between model accuracy and computational efficiency.

A commonly adopted strategy is model decomposition, in which the overall system is divided into slow-varying subsystems, such as crane translation and boom actuation, and fast-varying subsystems, such as load swing. Separate controllers can then be designed for each subsystem to simplify control implementation. This idea was concretely demonstrated in the work of Cai *et al.* [51], who developed a comprehensive kinematic model of a dual crane system by analyzing its closed-chain characteristics. Their method innovatively divided the system into a manipulator subsystem and a suspension subsystem. By establishing geometric constraint relationships between the load pose and the crane joint parameters, and introducing a coordination error index to quantify synchronization performance, this framework effectively reduced the complexity of dynamic modeling while preserving essential physical characteristics. It therefore provided a feasible foundation for real time trajectory planning in DCC cooperative hoisting.

1.2.3 Control Strategy

The control strategy of DCC systems represents the core of their automation and intelligence level. Its development has evolved significantly from simple independent control to sophisticated cooperative control. The driving motivation behind this evolution lies in addressing the system's inherent challenges of strong coupling, nonlinearity, and underactuation, with the ultimate goal of improving operational performance, safety, and environmental adaptability.

Early studies primarily adopted *PID-based* independent control strategies, where each crane was individually controlled to achieve basic coordination [52–56]. However, such approaches were incapable of effectively managing the strong coupling and nonlinear dynamics intrinsic to dual crane systems. With a deeper understanding of these coupling characteristics, researchers began to develop nonlinear cooperative control methods that consider the complete system dynamics [57, 58].

Initially, dual crane operations were performed in an independent mode, with two cranes manually coordinated to execute fundamental movements. As the complexity of heavy lifting tasks increased, research attention gradually shifted toward cooperative and coupled control [59]. This evolution is reflected in two main aspects. From the kinematic modeling perspective, the dual crane system fundamentally differs from a single crane system, forming a closed chain kinematic structure. As noted by Liu *et al.* [60], the cranes, the suspended load, and the ground together constitute a highly coupled system, in which the load's pose must be indirectly adjusted by coordinating the motions of both crane booms. From the dynamic coordination perspective, Liu *et al.* [61] established a set of nonlinear equations incorporating geometric, force, and moment balance constraints to accurately describe the coupled dynamics, achieving deep coordination of the dual crane motions. This control strategy not only accounts for kinematic coupling but also addresses the dynamic essence of the system, thereby ensuring stability and safety throughout the lifting process.

The cooperative hoisting of DCCs constitutes a typical multi-objective and multi-constraint optimization problem. The evolution of control strategies is reflected across several dimensions [62]. At the offline planning level, Cai *et al.* [51, 63] proposed a path planner based on a priority based multi objective parallel genetic algorithm. By simultaneously considering collision avoidance, dual crane coordination, and load balance constraints, their method automatically generates optimized lifting trajectories in complex three dimensional environments. At the real time control level, Liu *et al.* [61] designed synchronous and coupling error variables to achieve real time information exchange between the two cranes. This approach not only enhances the synchronization of boom motions but also effectively suppresses load swing, addressing the challenge of searching narrow feasible regions in high dimensional solution spaces. More importantly, the introduction of a multi layer nested continuous terminal sliding surface theoretically guarantees finite time convergence of both positioning and synchronization errors,

thereby ensuring fast response and closed loop stability of the system.

Currently, control strategies exhibit a trend toward multi method integration, combining, for instance, model predictive control with intelligent algorithms [64–69] and integrating open loop trajectory planning with closed loop feedback control [70]. These developments collectively enable dual crane systems to meet the stringent precision requirements of complex industrial applications such as large structure assembly and wind turbine installation.

The evolution of control strategies for dual crane systems clearly demonstrates a technological progression from local independent control to global system optimization, from ensuring feasibility to pursuing optimality, and from human experience based operation to intelligent, model driven autonomous decision making. Future research directions include improving system adaptability in dynamic environments, enhancing robustness against external disturbances, and extending operational capability to full three dimensional lifting tasks. In particular, the incorporation of advanced control methodologies such as finite-time control, real time coordination mechanisms, and nonlinear coupled control provides a solid technical foundation for achieving automation and intelligence in heavy load hoisting and precision assembly tasks.

Load sway suppression is a core challenge in achieving safe and efficient crane operations. For dual cranes that form a closed chain system, this problem becomes particularly complex, as it requires mitigating both the inherent swing caused by individual crane dynamics and the additional oscillations induced by improper cooperative coordination [71]. To address these challenges, multi layer control strategies have been developed.

At the open loop feedforward control level, input shaping techniques are employed to preprocess control commands through specially designed filters based on the system's geometric and dynamic constraints [72, 73]. These filters effectively suppress residual oscillations while maintaining strong robustness against modeling uncertainties [74–76]. Various input shapers have been successfully applied to dual crane systems, demonstrating their capability in vibration attenuation during cooperative lifting operations [77–80].

At the closed loop feedback control level, model-based approaches such as *sliding mode control* [81–86] and *active disturbance rejection control* (ADRC) [87–90] have been widely adopted. These methods utilize state observers such as extended state observers to estimate and compensate for both internal and external disturbances in real time [91, 92], thereby actively and precisely suppressing load sway and ensuring closed loop stability under perturbations.

To further handle strong system nonlinearities and parameter uncertainties, intelligent control techniques have been introduced [93–96]. For instance, neural network based sway suppression methods can adaptively estimate dynamic parameters and system models without relying on precise prior modeling, offering enhanced adaptability and learning capability [97].

The effective implementation of these control strategies fundamentally relies on motion

constraint management at the lower level. By accurately modeling the geometric and mechanical relationships within the closed-chain structure composed of the two cranes and the suspended load, the feasibility and safety of coordinated motion are ensured. This constraint management prevents excessive internal forces or instability caused by uncoordinated motion, thereby providing essential stability boundaries and feasibility conditions for upper layer control algorithms.

Currently, hybrid control frameworks that integrate the advantages of the aforementioned strategies are emerging as the mainstream approach to enhance anti-sway performance and operational efficiency of dual crane systems operating in complex and dynamic environments.

1.3 Structure of the Thesis and Contributions

1.3.1 Structure of the Thesis

The remainder of the thesis is organized as follows.

Chapter 2 reviews the theoretical background and methodology that underpin this work. It summarizes the tools used throughout the thesis, including Lagrangian mechanics for modeling closed–chain systems and the control techniques adopted later.

Chapter 3 develops the DCC system with a point-mass load. A method is proposed to regulate the lengths of the two hoisting ropes so that the suspended load follows a predefined path while satisfying boundedness constraints on rope velocities. The chapter first presents the system description and modeling assumptions, followed by a detailed kinematic analysis of the closed chain configuration. Based on the derived relationships between cable lengths and load motion, the desired trajectories are generated in the cable space domain, ensuring feasible motion profiles. After analyzing the direct approximate solution method and the line–search optimization method, an adaptive velocity shaping strategy is proposed based on the direct approximation framework. This method maintains a relatively high lifting speed under cable velocity constraints while ensuring a smooth deceleration as the system approaches the target. Finally, simulation results verify the effectiveness of the proposed trajectory generation method, compared with the original method, the improved strategy achieves a significant increase in lifting speed.

Chapter 4 investigates the cooperative hoisting dynamics of a DCC system carrying a rigid-rod load. Compared with the point-mass case, the rigid-rod configuration introduces both translational and rotational dynamics, resulting in a higher order and more strongly coupled closed chain system. The chapter begins with the system description and modeling assumptions, followed by a detailed kinematic analysis that establishes the geometric and motion constraints governing the coupled motion of the two cranes and the rigid load. A complete dynamic

model is then formulated through the Lagrangian approach, which systematically incorporates the constraint forces acting within the closed-chain structure.

To simplify the resulting high dimensional equations, an order reduction procedure is introduced to derive a lower order representation that preserves the essential dynamic features of the system. Subsequently, the equilibrium configurations of the cranes and load are analytically derived, providing insight into feasible cooperative postures and tension distributions under static balance. Finally, stability analyses are performed at the equilibrium points. Both linearized and energy based methods are employed to evaluate the stability characteristics, demonstrating that the reduced dynamic model can accurately capture the local and global stability behavior of the cooperative hoisting system.

Chapter 5 presents the design and validation of cooperative control strategies for the DCC system. The chapter begins by defining the control objectives and analyzing the inherent system properties, emphasizing the need for coordinated motion and load-sway suppression under cable velocity constraints.

In the next step, a desired velocity profile is designed to ensure smooth and bounded motion of the cables while satisfying both geometric and dynamic feasibility. The proposed velocity planning method guarantees that the reference trajectories are consistent with the equilibrium conditions derived in previous chapters, enabling safe and efficient load transfer along the predefined path.

Subsequently, a PID-based coupled error compensation control scheme is developed. This controller coordinates the two cranes by compensating for both synchronization and load orientation errors. The proposed control structure combines trajectory based reference generation with feedback error compensation to enhance tracking precision and transient response, suppress oscillations, and ensure asymptotic convergence of the load position and attitude.

Finally, simulation case studies are carried out to assess the performance of the proposed control strategy. Two representative lifting scenarios are first considered, namely a symmetric configuration and an asymmetric configuration under horizontal hoisting tasks. The simulation results confirm the effectiveness and robustness of the control scheme in achieving precise coordination, vibration reduction, and stable lifting motion even under geometric asymmetry. In addition, a third simulation case is considered, in which a combined hoisting task composed of sequential lifting, load rotation, and final vertical positioning is simulated.

Chapter 6 concludes the thesis, summarizing the main findings and discussing the practical implications for heavy duty cooperative hoisting. It also outlines future directions such as adaptation to dynamic environments and full 3D operational extensions.

1.3.2 Contributions

In this thesis, contributions are presented in Chapters 3-5. The contributions are summarized as follows:

1. **Adaptive velocity shaping for time efficient cooperative hoisting.** To further enhance lifting efficiency under rope velocity constraints, an adaptive velocity shaping method is developed as an improvement over the direct approximation approach. Instead of relying on a predefined velocity profile, this method dynamically adjusts the motion velocity in real time based on the instantaneous load position. By introducing a position dependent adjustment function, the horizontal velocity of the load is continuously adapted according to the dynamic cable factors. This adaptive mechanism guarantees full compliance with the cable velocity constraints while maintaining a relatively high operational speed and achieving smooth deceleration as the load approaches the target position. Simulation results demonstrate that the proposed adaptive velocity shaping method significantly reduces the total lifting time compared with conventional manual on-site observation and command operations.

2. **Nonlinear dynamic modeling and constraint based order reduction for rigid-rod loads.** An accurate nonlinear dynamic model of a DCC system lifting a rigid-rod load is developed without adopting any linearization assumptions. The proposed model fully captures the geometric coupling and closed-chain characteristics of the system. By systematically applying motion constraints, the original tenth-order dynamic model is reduced to a simplified sixth-order form, with the degrees of freedom reduced from five to three, while preserving the essential nonlinear behaviors. This reduction significantly decreases the complexity of subsequent controller design and provides a valuable reference for the modeling of similar constrained mechanical systems.

3. **Constraint consistent reference generation.** A constraint consistent trajectory generation method is proposed, in which the desired trajectories are directly designed in the cable length domain. By determining the load orientation at each instant through the equilibrium equations, this approach guarantees that every trajectory point inherently satisfies the static equilibrium and geometric constraints of the system.

4. **Coupled error based cooperative control for coordinated motion and sway suppression.** A PID-based coupled error compensation control strategy is proposed to achieve coordinated motion between the DCCs while suppressing load sway during cooperative hoisting. The method defines coupled error variables that simultaneously capture synchronization deviations between the two cranes and the orientation errors of the suspended load. By designing appropriate PID gains and compensation terms, the controller

ensures asymptotic convergence of the load position and attitude to their desired trajectories. The proposed control framework effectively enhances synchronization accuracy, reduces vibration amplitudes, and guarantees smooth and stable cooperative motion under both symmetric and asymmetric configurations.

Chapter 2

Theoretical Background and Methodology

This chapter introduces the theoretical foundations and control principles that support the subsequent analysis of mechanical systems. It is divided into two main parts, focusing respectively on the formulation of dynamical models and on feedback control strategies.

The first part presents the fundamental concepts of *Lagrangian mechanics* and demonstrates their application through a simple pendulum example. Starting from the energy functions of the system, the *Euler–Lagrange equation* is derived to obtain the nonlinear equation of motion. The discussion then extends to the analysis of equilibrium and stability based on the *Lyapunov method*, showing how the total mechanical energy can serve as a measure of system stability. The geometric interpretation of constrained motion on a *manifold* is also introduced to provide an intuitive understanding of constrained dynamics. Through this example, the essential ideas of energy-based modeling, constraint representation, and stability analysis are clearly illustrated.

The second part introduces the *Proportional Integral Derivative* (PID) control method, which remains one of the most widely used feedback algorithms in industrial and robotic systems. The formulation of the PID law is explained together with the roles of the proportional, integral, and derivative actions. A temperature control example is included to illustrate how the three terms complement each other to achieve fast, accurate, and well damped responses.

Overall, this chapter provides a complete theoretical and practical foundation for the modeling and control techniques employed in the remainder of this dissertation.

The theoretical formulation of Lagrangian mechanics and its geometric interpretation are based on the treatments presented in Hamill [98] and Fasano et al. [99]. The principles of PID control and related tuning methods follow the discussion by Åström et al. [100].

2.1 Lagrangian Mechanics and Stability Analysis

2.1.1 The Principle of Stationary Action

The entire framework of Lagrangian mechanics is founded on *Hamilton's principle*, also known as the principle of stationary action. It states that, among all possible trajectories connecting an initial configuration at time t_1 and a final configuration at time t_2, the actual path followed by

a physical system is the one that makes the action functional stationary, that is, the variation of the action is zero.

The action S is defined as the time integral of the *Lagrangian* $\mathcal{L}$:

$$S = \int_{t_1}^{t_2} \mathcal{L}(q, \dot{q}, t)\, dt, \tag{2.1}$$

where:

- $q = [q_1, q_2, \ldots, q_n]^\top$ is the vector of *generalized coordinates* that describe the configuration of the system;
- $\dot{q} = [\dot{q}_1, \dot{q}_2, \ldots, \dot{q}_n]^\top$ are the corresponding *generalized velocities*, i.e., the time derivatives of q_i;
- $\mathcal{L}(q, \dot{q}, t)$ is the *Lagrangian* of the system, typically defined as the difference between the *kinetic energy* T and the *potential energy* V.

According to Hamilton's principle, the actual motion satisfies

$$\delta S = \delta \int_{t_1}^{t_2} \mathcal{L}(q, \dot{q}, t)\, dt = 0, \tag{2.2}$$

for all admissible infinitesimal variations δq_i that vanish at the endpoints. Applying the *calculus of variations* to Eq. (2.2) yields the Euler–Lagrange equations.

2.1.2 The Euler–Lagrange Equation and Constrained Systems

Starting from Hamilton's principle, the equations of motion for a mechanical system can be obtained by applying the calculus of variations to the action integral. For a system characterized by n generalized coordinates $q_1, q_2, \ldots, q_n$, the resulting equations are known as the Euler–Lagrange equations:

$$\frac{d}{dt}\left(\frac{\partial \mathcal{L}}{\partial \dot{q}_i}\right) - \frac{\partial \mathcal{L}}{\partial q_i} = 0, \qquad i = 1, 2, \ldots, n. \tag{2.3}$$

Generalized coordinates. A generalized coordinate is any independent variable that uniquely defines the configuration of a system. Unlike Cartesian coordinates, which specify absolute positions in space, generalized coordinates may represent distances, angles, or any quantities suited to the system geometry. For example, in a pendulum, a single angular coordinate θ can replace the two Cartesian coordinates (x, y) because the rod length is fixed. If the system has r degrees of freedom, one can always find r generalized coordinates $q_1, \ldots, q_r$ that fully describe its motion. This flexibility allows the Lagrangian approach to represent complex constrained systems with a minimal number of variables.

Generalized forces. When *non-conservative forces* (such as friction, viscous damping, or any force that does not derive from a potential energy function) or external inputs act on the system, they are represented by generalized forces Q_i, which measure the work done by those forces corresponding to infinitesimal virtual displacements δq_i. Their definition follows from the *principle of virtual work*:

$$\delta W = \sum_{i=1}^{n} Q_i \, \delta q_i, \tag{2.4}$$

where δW is the total virtual work produced by all non-conservative forces for a set of virtual displacements δq_i consistent with the system constraints. Each Q_i represents the component of the applied forces or moments that acts along the direction of the generalized coordinate q_i. Including generalized forces, the Euler–Lagrange equations take the extended form:

$$\frac{d}{dt}\left(\frac{\partial \mathcal{L}}{\partial \dot{q}_i}\right) - \frac{\partial \mathcal{L}}{\partial q_i} = Q_i, \qquad i = 1, 2, \ldots, n. \tag{2.5}$$

Each term in Eq. (2.5) carries a distinct physical interpretation:

- $\dfrac{\partial \mathcal{L}}{\partial \dot{q}_i}$ represents the generalized momentum conjugate to q_i;
- $\dfrac{\partial \mathcal{L}}{\partial q_i}$ expresses how the system's energy changes with configuration;
- their difference corresponds to the net generalized force acting along q_i.

Therefore, Eq. (2.5) generalizes Newton's second law to arbitrary coordinate systems, allowing motion equations to be expressed in compact energy-based form.

The Lagrangian function. The Lagrangian is defined as

$$\mathcal{L}(q, \dot{q}, t) = T(q, \dot{q}, t) - V(q, t), \tag{2.6}$$

where T is the kinetic energy and V is the potential energy of the system. The difference $T - V$ serves as a scalar function encapsulating both inertial and energy-storage properties. Because $\mathcal{L}$ is scalar and coordinate-independent, it provides a systematic and unified way to derive dynamic equations even for complex multi-body systems.

In many mechanical systems, not all coordinates are independent because the motion of one part may restrict the motion of others through geometric relations or mechanical linkages. The number of independent quantities required to completely specify the configuration of a system is called the *degree of freedom* (DOF). For example, a particle moving freely in a plane has two degrees of freedom corresponding to its coordinates (x, y), while a pendulum constrained by a rigid rod has only one, since its position can be described by a single angular coordinate θ.

In general, if a system has n coordinates and k independent constraints, its number of degrees of freedom is reduced to

$$r = n - k, \tag{2.7}$$

where r denotes the total number of independent generalized coordinates.

A holonomic constraint is an algebraic equation involving the coordinates and possibly time,

$$\phi_j(q_1, q_2, \ldots, q_n, t) = 0, \tag{2.8}$$

which can be integrated and expressed as a fixed relationship among the coordinates. A simple example is the constraint $x^2 + y^2 - l^2 = 0$ describing the motion of a pendulum mass that must remain at a fixed distance l from the pivot. In contrast, a non-holonomic constraint involves the velocities in a way that cannot be integrated into Eq. (2.8), for instance, the rolling constraint $v_x = R\dot{\theta}$ for a wheel on a plane.

When constraints are present, the system cannot move arbitrarily in the full n-dimensional configuration space but is restricted to an r-dimensional constraint manifold. A convenient and elegant way to incorporate such restrictions into the equations of motion is the *Lagrange multiplier method*. In this approach, each constraint $\phi_j(q, t) = 0$ introduces an auxiliary variable λ_j, known as a Lagrange multiplier. The augmented Lagrangian is written as

$$\mathcal{L}^*(q, \dot{q}, \lambda, t) = \mathcal{L}(q, \dot{q}, t) + \sum_{j=1}^{k} \lambda_j \phi_j(q, t), \tag{2.9}$$

and the stationary condition $\delta S = 0$ applied to $\mathcal{L}^*$ yields the *constrained Euler–Lagrange equations*:

$$\frac{d}{dt}\left(\frac{\partial \mathcal{L}}{\partial \dot{q}_i}\right) - \frac{\partial \mathcal{L}}{\partial q_i} = \sum_{j=1}^{k} \lambda_j \frac{\partial \phi_j}{\partial q_i}, \qquad \phi_j(q, t) = 0. \tag{2.10}$$

Each multiplier λ_j represents the *constraint force* associated with $\phi_j(q, t) = 0$, acting in the direction normal to the constraint surface and ensuring that the system's motion remains within the allowed manifold. Physically, these are the internal reaction forces that enforce the geometric constraints, but they need not be explicitly computed to obtain the correct motion equations.

The Lagrange multiplier method provides a powerful and general framework for analyzing constrained systems. It allows the equations of motion to be derived directly from the energy functions and constraint relations, without separately considering the geometry of the constraint forces. This approach elegantly unifies the treatment of constrained and unconstrained dynamics, and is widely applicable to multibody systems, robotic manipulators, and cable-driven mechanisms. However, for systems involving multiple geometric constraints and a large number of coupled variables, such as the dual crawler crane system studied in this work, the

Lagrange multiplier formulation becomes analytically cumbersome and computationally intensive. In such cases, a approach based on constraint reduction is proposed in this work to handle the complex coupling relations among system variables. This method serves as one of the contributions of the present research and will be described in detail in the following chapters.

The Lagrangian method as a whole offers several advantages over direct Newtonian force analysis:

1. It provides a coordinate-independent formulation: any convenient set of generalized coordinates can be used without altering the physical meaning.
2. It handles constraints naturally through the use of Lagrange multipliers, without requiring explicit computation of reaction forces.
3. It unifies translational and rotational dynamics within a single mathematical framework.
4. It simplifies the derivation of equations for systems with multiple degrees of freedom by working with scalar energy functions instead of vector forces.

These properties make the Lagrangian formulation particularly powerful for modeling complex mechanical systems, while the specific constraint-reduction strategy adopted in this research extends its applicability to highly coupled, high-dimensional configurations such as dual crawler cranes.

2.1.3 Lagrangian Modeling and Stability Analysis of a Simple Pendulum

To illustrate the concepts introduced in the previous sections, this subsection presents a complete example based on a simple pendulum. The pendulum provides a minimal yet representative system that exhibits holonomic constraints, reduced degrees of freedom, and clear equilibrium and stability properties. Through this example, the essential ideas of energy-based modeling, constraint geometry, and Lyapunov stability analysis can be understood in an intuitive and self-contained way.

System modeling and generalized coordinates. Consider a point mass m attached to a massless rigid rod of fixed length l in a uniform gravitational field g, as shown in Fig. 2.1. The position of the mass in the plane is described by the Cartesian coordinates (x, y). Since the distance between the mass and the pivot is constant, the motion is subject to a holonomic constraint

$$\phi(x, y) = x^2 + y^2 - l^2 = 0. \tag{2.11}$$

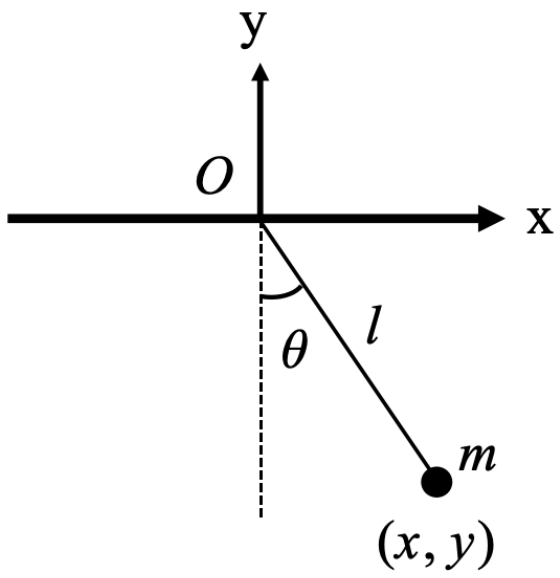

Figure 2.1: Schematic diagram of a single pendulum with a rigid rod.

A holonomic constraint is an algebraic relation among the coordinates (and possibly time) that restricts the admissible configurations of the system. Such constraints reduce the number of independent variables required to describe the system.

The number of independent variables that uniquely determine the configuration of a system is called the degree of freedom. In this example, although the motion occurs in a two-dimensional plane ($n = 2$), the single holonomic constraint given by Eq. (2.11) reduces the system to one independent coordinate ($r = n - k = 1$). Hence, the configuration can be fully described by a single generalized coordinate θ, defined as the angle between the rigid rod and the vertical direction. The Cartesian coordinates of the mass are therefore expressed as

$$x = l \sin\theta, \qquad y = -l \cos\theta.$$

The coordinate system is chosen such that the origin is located at the pivot point and the y-axis is directed upward. With this convention, the pendulum bob is at its lowest point when $\theta = 0$ (i.e., $y = -l$).

The kinetic energy and potential energy of the pendulum are then given by

$$T = \tfrac{1}{2}m(\dot{x}^2 + \dot{y}^2) = \tfrac{1}{2}ml^2\dot{\theta}^2, \qquad V = mg(y + l) = mgl(1 - \cos\theta).$$

Here the potential energy expression $V = mg(y+l)$ corresponds to choosing the zero potential energy level at the lowest position of the pendulum ($y = -l$). This choice ensures that $V \geq 0$ for all configurations and simplifies the subsequent energy and stability analysis. Using the generalized coordinate θ thus allows the system to be represented by a single variable that automatically satisfies the geometric constraint, while the energy functions are conveniently

defined relative to the equilibrium configuration. Thus, the Lagrangian is given by

$$\mathcal{L}(\theta, \dot{\theta}) = T - V = \tfrac{1}{2} m l^2 \dot{\theta}^2 - mgl(1 - \cos\theta). \tag{2.12}$$

we compute

$$\frac{\partial \mathcal{L}}{\partial \dot{\theta}} = ml^2\dot{\theta}, \qquad \frac{d}{dt}\left(\frac{\partial \mathcal{L}}{\partial \dot{\theta}}\right) = ml^2\ddot{\theta},$$

and

$$\frac{\partial \mathcal{L}}{\partial \theta} = -\frac{\partial}{\partial \theta}\Big(mgl(1 - \cos\theta)\Big) = -mgl\sin\theta.$$

The Euler–Lagrange equation with generalized force Q_θ is

$$\frac{d}{dt}\left(\frac{\partial \mathcal{L}}{\partial \dot{\theta}}\right) - \frac{\partial \mathcal{L}}{\partial \theta} = Q_\theta.$$

For the conservative pendulum $Q_\theta = 0$, hence

$$ml^2\ddot{\theta} + mgl\sin\theta = 0. \tag{2.13}$$

Assume a small viscous force acts on the bob and is proportional to its linear speed along the arc. The bob speed is $v = l\dot{\theta}$, so the damping force is

$$F_d = -c\,v = -c\,l\dot{\theta},$$

where $c > 0$ is the damping coefficient (units N·s/m). By the principle of virtual work, the virtual work of nonconservative forces is

$$\delta W = \mathbf{F}_d \cdot \delta\mathbf{r}.$$

Here $\delta\mathbf{r}$ is tangential, with magnitude $l\,\delta\theta$. Thus

$$\delta W = (-c\,l\dot{\theta})\,(l\,\delta\theta) = \big(-c\,l^2\dot{\theta}\big)\,\delta\theta.$$

Comparing with the definition $\delta W = Q_\theta\,\delta\theta$ gives the generalized force

$$Q_\theta = -c\,l^2\dot{\theta}.$$

Substituting Q_θ into the Euler–Lagrange equation yields the damped model

$$ml^2\ddot{\theta} + cl^2\dot{\theta} + mgl\sin\theta = 0. \tag{2.14}$$

Remark. If the viscous effect is modeled instead as a torque at the pivot proportional to the angular velocity, say $\tau_d = -c_\theta\dot{\theta}$ (units N·m·s), then the generalized force is $Q_\theta = -c_\theta\dot{\theta}$ and the

damping term becomes $c_\theta \dot{\theta}$ rather than $cl^2\dot{\theta}$. The present work adopts the linear speed model at the bob, which leads to the factor l^2.

Geometric interpretation on the constraint manifold. The motion of a constrained mechanical system can be viewed geometrically as the evolution of its state on a lower-dimensional surface embedded in a higher-dimensional space. This surface is referred to as a manifold. Formally, a manifold is a set of points that locally resembles the Euclidean space $\mathbb{R}^r$, where r is the number of independent degrees of freedom of the system. In the context of mechanical systems, a manifold represents the subset of the configuration space $\mathbb{R}^n$ that satisfies all constraint equations, and the system's trajectory is confined to this subset.

For the simple pendulum, the holonomic constraint $x^2 + y^2 - l^2 = 0$ defines a one-dimensional constraint manifold

$$\mathcal{M} = \{(x, y) \in \mathbb{R}^2 \mid x^2 + y^2 = l^2\}.$$

This manifold corresponds to a circle of radius l centered at the pivot point in the two-dimensional configuration space. Although the ambient space has two dimensions, the pendulum effectively evolves on the one-dimensional manifold $\mathcal{M}$, which can be parametrized by the single generalized coordinate θ.

At any point (x, y) on $\mathcal{M}$, the admissible velocity vectors $(\dot{x}, \dot{y})$ must satisfy the differential form of the constraint,

$$x\dot{x} + y\dot{y} = 0.$$

This relation defines the *tangent space* $T_{(x,y)}\mathcal{M}$, which is the set of all instantaneous directions in which the pendulum can move while still satisfying the constraint. Geometrically, the tangent space at (x, y) is a line tangent to the circle $\mathcal{M}$, and it represents the allowable motion directions at that instant.

The acceleration of the pendulum can be decomposed into two orthogonal components: a tangential component that determines the actual motion along $\mathcal{M}$, and a normal component that corresponds to the constraint reaction force maintaining the rod length constant. The resulting reduced dynamics describe the evolution of the system solely along the manifold, which leads to the intrinsic one-dimensional equation of motion

$$ml^2\ddot{\theta} + mgl \sin\theta = 0.$$

Hence, the pendulum dynamics can be interpreted as the evolution of a one-dimensional vector field on the constraint manifold $\mathcal{M}$. This geometric viewpoint provides an intuitive understanding of how the Lagrangian formulation inherently enforces constraints, allowing the system's motion to be represented as trajectories on a manifold of admissible configurations.

Equilibrium points and Lyapunov stability. A *state of equilibrium* is a configuration in which all generalized coordinates and velocities remain constant, that is, $\dot{\theta} = \ddot{\theta} = 0$. From Eq. (2.14), this condition is satisfied when $\sin\theta = 0$, leading to two equilibrium points:

$$\theta_d^\star = 0 \quad \text{(downward equilibrium)}, \qquad \theta_u^\star = \pi \quad \text{(upright equilibrium)}.$$

In general, an equilibrium point of a dynamical system is said to be *stable* if any small disturbance in its state produces only small deviations in motion, and the state remains in the neighborhood of the equilibrium. If, in addition, the system state eventually returns to the equilibrium as time tends to infinity, the equilibrium is said to be *asymptotically stable*. Conversely, if small perturbations grow with time and cause the system to diverge, the equilibrium is *unstable*.

The *Lyapunov stability theory* provides a general and intuitive framework for assessing the stability of nonlinear systems without solving their trajectories explicitly. The main idea is to find a scalar function $V(x)$, called a *Lyapunov function*, which behaves like an energy measure of the system: it is positive around the equilibrium and decreases along system trajectories. If such a function exists, the equilibrium is stable; if it decreases strictly with time, the equilibrium is asymptotically stable.

For the pendulum, a natural Lyapunov candidate is the total mechanical energy,

$$E(\theta, \dot{\theta}) = T + V = \tfrac{1}{2} m l^2 \dot{\theta}^2 + mgl(1 - \cos\theta). \tag{2.15}$$

Differentiating Eq. (2.15) along the trajectories of Eq. (2.14) yields

$$\dot{E} = ml^2 \dot{\theta}\ddot{\theta} + mgl \sin\theta\dot{\theta} = -cl^2\dot{\theta}^2 \leq 0. \tag{2.16}$$

The function $E(\theta, \dot{\theta})$ is *positive definite* around the equilibrium $\theta = 0$ (it vanishes only at this point), and its time derivative $\dot{E}$ is *negative semi-definite*, meaning that energy can only decrease or remain constant. Hence, the total mechanical energy plays the role of a Lyapunov function for the damped pendulum.

LaSalle's invariance principle. When $\dot{E}$ is negative semi-definite rather than strictly negative, *LaSalle's invariance principle* provides a stronger conclusion. It states that the system trajectories asymptotically converge to the largest invariant subset of the region where $\dot{E} = 0$. For the pendulum, $\dot{E} = 0$ implies $\dot{\theta} = 0$, and substituting into Eq. (2.14) gives $\sin\theta = 0$. Therefore, the invariant set consists of the two equilibrium points $(\theta, \dot{\theta}) = (0, 0)$ and $(\pi, 0)$. Among them, the downward equilibrium $(\theta, \dot{\theta}) = (0, 0)$ corresponds to the minimum of the potential energy, so it is asymptotically stable; the upright equilibrium $(\pi, 0)$ corresponds to the potential energy maximum and is unstable.

Physically, damping continuously dissipates mechanical energy, causing the pendulum to lose kinetic energy until it comes to rest at the lowest potential point. The Lyapunov approach provides a rigorous mathematical framework to formalize this intuitive behavior: stability is guaranteed by the monotonic decrease of a suitable energy-like function.

This example demonstrates how a holonomic constraint reduces the degrees of freedom of a system and confines its motion to a lower-dimensional manifold. The Lagrangian formulation automatically incorporates the constraint through the choice of generalized coordinates, and the resulting energy function provides a natural Lyapunov candidate for assessing stability. The same geometric and energy-based reasoning will be extended in subsequent chapters to address the modeling and stability analysis of more complex constrained systems, such as the dual crawler crane under cooperative hoisting.

2.2 PID Control

The Proportional Integral Derivative (PID) controller is among the most extensively used feedback control strategies in industrial and robotic applications. Its appeal lies in its simplicity, intuitive tuning procedure, and reliable performance for a wide variety of linear and mildly nonlinear systems. Despite being developed nearly a century ago, the PID controller remains a cornerstone of modern automation because it encapsulates the essential principles of feedback regulation: reacting to present deviations, compensating for accumulated errors, and anticipating future trends.

2.2.1 Fundamental Formulation

Let the *set point* be $SP(t)$ and the *process variable* be $PV(t)$. The control objective is to minimize the *error* $e(t) = SP(t) - PV(t)$, which represents the instantaneous deviation between the desired and measured outputs. The PID algorithm computes the control input $u(t)$ as a weighted combination of three terms that respectively respond to the present, past, and rate of change of the error:

$$u(t) = K_p e(t) + K_i \int_0^t e(\tau)\, d\tau + K_d \frac{de(t)}{dt}. \tag{2.17}$$

The three gains K_p, K_i, and K_d are respectively the proportional, integral, and derivative coefficients that determine the contribution of each component to the control signal.

The proportional term responds immediately to the current error, the integral term corrects for persistent bias by accounting for accumulated error over time, and the derivative term introduces a predictive damping effect based on how fast the error is changing. Together, these actions enable the controller to achieve fast response, small steady state error, and good damp-

ing of oscillations. In the Laplace domain, Eq. (2.17) corresponds to the transfer function

$$G_c(s) = K_p + \frac{K_i}{s} + K_d s, \tag{2.18}$$

which is the classical parallel form of the PID controller.

In real applications, ideal differentiation is not physically realizable and tends to amplify measurement noise. To mitigate this, the derivative term is often implemented as a low-pass filtered form:

$$G_c(s) = K_p + \frac{K_i}{s} + K_d \frac{s}{\tau_d s + 1}, \tag{2.19}$$

where τ_d is a small derivative filter constant. This modification retains the damping benefit of the derivative term while reducing sensitivity to high-frequency noise.

Each component of the PID law performs a distinct role in shaping the closed-loop response.

Proportional Term (P): $K_p e(t)$

The proportional term provides an immediate corrective action proportional to the current error. It represents the most intuitive form of feedback: when the system deviates from the desired value, the controller generates a correction of corresponding magnitude.

- Effect: Increasing K_p decreases rise time and reduces *steady-state error*, but excessive K_p can cause overshoot, oscillations, or even instability.
- Physical Analogy: Steering a car back to the center of a lane if you are far from the center, you steer sharply; if close, you steer gently. A very large K_p is like overreacting to small deviations, causing the car to weave.

Integral Term (I): $K_i \int_0^t e(\tau)\, d\tau$

The integral term accounts for the accumulation of past errors. It ensures that even small, steady discrepancies between the set point and the process variable are eliminated over time. By integrating the error, the controller develops a memory of past deviations and continuously increases the control effort until the steady-state error is zero.

- Effect: The integral action eliminates steady-state error but can slow down the transient response and increase overshoot if K_i is too large. When actuators saturate, the integral term may continue to grow even though the output cannot respond—a phenomenon known as *integral windup*. This effect is mitigated by techniques such as conditional integration or integral clamping.

- Physical Analogy: If a car consistently drifts slightly to the right, you gradually apply a constant left correction to remove the accumulated offset. The longer the deviation persists, the stronger the correction becomes.

Derivative Term (D): $K_d \frac{de(t)}{dt}$

The derivative term predicts the future trend of the error by reacting to its rate of change. It introduces a damping effect that smooths the control action and helps prevent overshoot.

- Effect: Derivative control reduces overshoot and oscillations, improving the transient response and stability margin. However, because it amplifies noise, the derivative term is typically filtered using the form in Eq. (2.19).
- Physical Analogy: As you steer a car back toward the center, you anticipate your approach speed. If you are turning quickly, you begin to relax the steering before reaching the center to avoid overshooting.

2.2.2 Practical Implementation and Tuning

In digital controllers, the continuous PID law is discretized for computation at each sampling instant T_s. The discrete positional form is

$$u(k) = K_p e(k) + K_i T_s \sum_{i=0}^{k} e(i) + K_d \frac{e(k) - e(k-1)}{T_s}, \tag{2.20}$$

where k denotes the discrete time index. The derivative term is often replaced by a first-order filtered difference to attenuate noise.

When the actuator output is limited, the integral term may accumulate excessively, causing a large overshoot once the saturation is released. This phenomenon is known as *integral windup*. To prevent it, various *anti-windup* schemes are employed, such as halting the integration when the control input reaches its limit or feeding back the saturation error to the integrator.

Determining appropriate values for (K_p, K_i, K_d), known as *tuning*, is crucial for achieving the desired trade-off between speed and robustness.

- *Manual tuning:* Adjusting gains iteratively while observing the step response, leveraging an understanding of how each term affects performance.
- *Ziegler Nichols methods:* Based on the process reaction curve or the ultimate gain and oscillation period. These methods provide empirical tuning rules that achieve a quarter-decay response for many industrial plants.

- *Cohen Coon method:* An open-loop procedure that estimates gains from a first-order plus dead time approximation of the process. These classical heuristics are effective for well-behaved, moderately lag-dominant systems, but they may yield aggressive gains for non-minimum-phase or highly coupled processes.

Example: Temperature Control System

Consider a precision oven where the temperature must be maintained at $150°$C with an accuracy of $\pm 0.5°$C. A thermocouple measures the internal temperature $PV(t)$, and the PID controller adjusts the electrical power applied to the heating element.

- Proportional Action: When the temperature drops to $149°$C ($e = 1°$C), the proportional term immediately increases heater power by an amount proportional to the deviation. For instance, with $K_p = 50$, the control effort increases by 50% of the rated power.
- Integral Action: If heat loss causes a small offset of $0.1°$C to persist, the integral term will continue to accumulate until this steady-state error is removed. Anti-windup protection ensures that the control signal does not exceed the actuator limit.
- Derivative Action: If the temperature is rising rapidly (e.g., $2°$C/s), the derivative term reduces the power preemptively to prevent overshoot, analogous to damping in mechanical systems.

This example illustrates how the three terms complement each other: proportional control provides responsiveness, integral control ensures accuracy, and derivative control adds damping for smooth convergence.

Chapter 3

Dual crawler crane system with poin-mass load

3.1 System Description and Assumptions

In dual crawler crane hoisting systems, the lifted loads vary widely in type and exhibit significant differences in shape and geometry. Depending on the physical characteristics of the lifted object, different modeling approaches can be adopted. When the load size is relatively small compared to the crane span, it can be reasonably approximated as a poin-mass. This simplification allows for clearer analytical derivation and provides fundamental insights into the system's kinematic and dynamic behavior.

In practical applications, the loads lifted by dual crane systems are typically characterized by large mass. In this study, the cooperative hoisting process involving DCCs is analyzed under the following simplifying assumptions, which are commonly adopted in similar crane related studies:

Assumption 3.1 *All crane motions are confined to a two-dimensional plane, and the entire system is modeled within this planar framework.*

Assumption 3.2 *The load has a significant mass, ensuring that the cables remain taut at all times while cable elasticity is neglected.*

A sketch of the two cooperating crawler cranes in the vertical $x-y$ plane is shown in Fig. 3.1, whose variables and parameters are defined in Table 3.1.

Table 3.1: Variables and parameters.

Symbols	Meanings	Units
L_1, L_2	rope length	m
(x, y)	coordinates of the load	m
$(X_1, Y_1), (X_2, Y_2)$	coordinates of the boom anchor	m
D	distance between two cranes	m

It should be noted that in this and the following chapter, the notation used to represent the cable lengths is identical to that of the boom anchor point coordinates. Moreover, in the

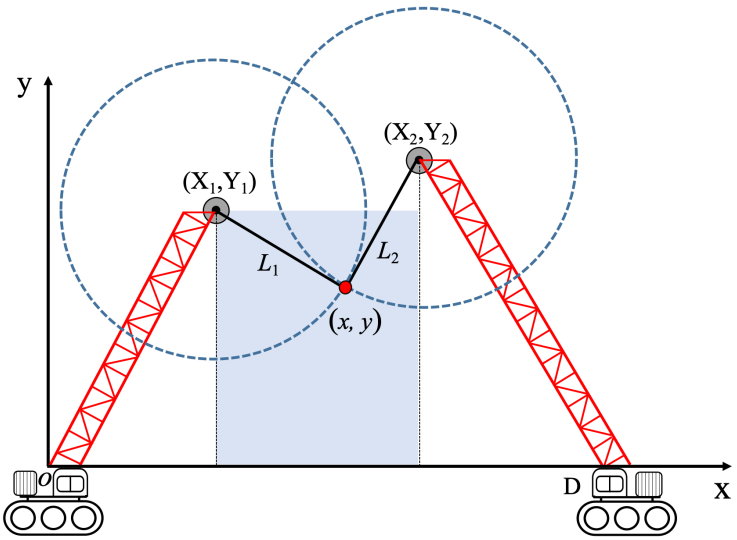

Figure 3.1: Schematic representation of DCCs with poin-mass.

rigid-rod model, the coordinates of the load's center are considered equivalent to the position coordinates of the point-mass load. The admissible load positions within the workspace are determined by the presence of tension in both cables, so that both cranes are carrying part of the load. This region is visually depicted as the shaded area in Fig. 3.1 and it is analytically described as follows:

$$\begin{cases} X_1 < x < X_2, \\ 0 \leq y < min(Y_1, Y_2). \end{cases} \tag{3.1}$$

In this study, prior to the hoisting operation, the DCCs are positioned according to the specific requirements of the lifting task. Once properly aligned, their positions remain fixed, and thus the distance D between the cranes is considered constant. Similarly, the boom angles are adjusted before the operation begins. Since the focus of this work is on the cooperative lifting of larg tonnage loads, and in accordance with industrial practice and safety considerations, the boom angles are assumed to remain unchanged throughout the entire hoisting process. Consequently, the boom anchor points (X_1, Y_1) and (X_2, Y_2) are treated as fixed.

3.2 Kinematic Analysis

Cable lengths are the Euclidean distances from the anchors to the load

$$L_1 = \sqrt{(x - X_1)^2 + (y - Y_1)^2}, \tag{3.2}$$

$$L_2 = \sqrt{(x - X_2)^2 + (y - Y_2)^2}, \tag{3.3}$$

the cable lengths are uniquely determined by the configuration (x, y, γ). We therefore define the inverse kinematics mapping

$$f_{L_{1,2}} : \ (x, y, \gamma) \in \mathbb{R}^2 \ \mapsto \ (L_1, L_2) \in \mathbb{R}^2,$$

compactly written as

$$(L_1, \ L_2) = f_{L_{1,2}}(x, y), \tag{3.4}$$

with the component-wise formulas provided in Eq. (3.2 – 3.3).

Eq. (3.2 – 3.3) describes two circles whose centers are the boom anchors, as shown in Fig. 3.1 with a dashed blue line. When the cable lengths L_1 and L_2 are given, the coordinate $(x, y)$of the load can be calculated as follows. From Fig. 3.1 it can be seen that Eq. (3.2 – 3.3) has two different (x,y) solutions (the two intersection points of the circles). Clearly, the physically meaningful solution for a load subject to gravity is the one with minimal value of y. Squaring Eq. (3.2 – 3.3) and subtracting each other the resulting relations one deduces the following

$$x = \frac{(L_1^2 - L_2^2 - X_1^2 - Y_1^2 + X_2^2 + Y_2^2) - 2y\,(Y_2 - Y_1)}{2\,(X_2 - X_1)}. \tag{3.5}$$

Substituting Eq. (3.5) into Eq. (3.2) one obtains the second order algebraic equation

$$ay^2 + by + c = 0 \tag{3.6}$$

whose coefficients are

$$\begin{cases} a = & \dfrac{(Y_2 - Y_1)^2 + (X_2 - X_1)^2}{(X_2 - X_1)^2} \\ b = & \dfrac{2\,(Y_2 - Y_1)\,X_2}{X_2 - X_1} - 2Y_2\,(X_2 - X_1) - \\ & \dfrac{(Y_2 - Y_1)\,(L_1^2 - L_2^2 - X_1^2 - Y_1^2 + X_2^2 + Y_2^2)}{(X_2 - X_1)^2} \\ c = & \dfrac{(L_1^2 - L_2^2 - X_1^2 - Y_1^2 + X_2^2 + Y_2^2)^2}{4\,(X_2 - X_1)^2} - L_2^2 + Y_2^2 \\ & - \dfrac{X_2\,(L_1^2 - L_2^2 - X_1^2 - Y_1^2 + X_2^2 + Y_2^2)}{X_2 - X_1} + X_2^2 \end{cases} \tag{3.7}$$

Among the two solutions of Eq. (3.6), the smallest one is clearly

$$y = \frac{-b - \sqrt{b^2 - 4ac}}{2a} \tag{3.8}$$

Introducing the additional parameter

$$r = \frac{L_1^2 - L_2^2 - X_1^2 - Y_1^2 + X_2^2 + Y_2^2}{2\,(X_2 - X_1)} \tag{3.9}$$

and inserting Eq. (3.8) into Eq. (3.5) one obtains the x coordinate of the load as follows:

$$x = r + \frac{\left(b + \sqrt{b^2 - 4ac}\right)(Y_2 - Y_1)}{2a\,(X_2 - X_1)} \tag{3.10}$$

From the geometric relations in Eq. (3.8) and Eq. (3.10), the load coordinates are uniquely determined by the cable lengths L_1, L_2. We therefore define the forward kinematics mapping

$$f_{x,y} : \ (L_1, L_2) \in \mathbb{R}^2 \ \mapsto \ (x, y) \in \mathbb{R}^2,$$

compactly written as

$$(x,\ y) = f_{x,y}(L_1, L_2), \tag{3.11}$$

with the component wise formulas provided in Eq. (3.8) and Eq. (3.10).

Through the kinematic analysis of the point-mass load, the relationship between the load coordinates and the cable lengths has been clearly established. This analysis provides the foundation for the subsequent design of the lifting trajectory.

3.3 Hoisting of Point-Mass Load under Cable Velocity Constraints

In practical crane operations, the cable velocity is subject to physical and safety limitations imposed by the drive system and the mechanical structure. To ensure smooth and stable motion of the lifted load, these velocity constraints must be explicitly considered during trajectory planning. In this section, the lifting task of a point-mass load is studied under cable velocity constraints. Starting from the kinematic relations established in the previous analysis, the desired motion trajectories and corresponding velocity profiles are designed to satisfy the prescribed limitations. Subsequently, the dynamic equations of the system are derived and analyzed to verify the feasibility of the obtained motion. This section thus provides a fundamental reference for extending the approach to more complex cases, such as the rigid-rod load model discussed in Chapter 4.

3.3.1 Trajectory and Velocity Profile Design

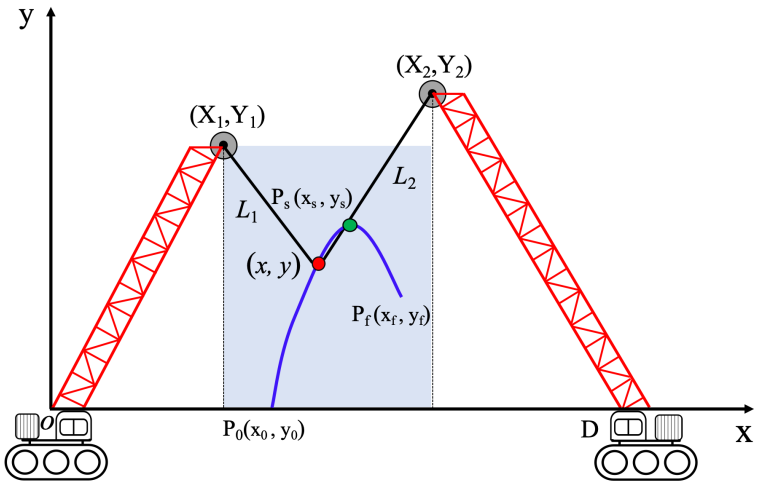

Figure 3.2: Desired trajectory of the load.

In the lifting operation of two crawler cranes, the position of the load can be controlled by changing the length of the two cables. We assume the desired trajectory of the load is given as a parabolic curve as shown in Fig. 3.2. Here $P_0 = (x_0, y_0)$ denotes the initial position of the load and $P_f = (x_f, y_f)$ the final position. Such a trajectory can be described by:

$$y = k\,(x - x_s)^2 + y_s, \quad \text{for } x \in [x_0, x_f] \tag{3.12}$$

where $k < 0$ is a negative coefficient and (x_s, y_s) is the vertex of the parabola which in this case denotes the maximum value of the quadratic function.

To move the load along the desired trajectory, we impose a trapezoidal velocity profile $v_x(t) = dx(t)/dt$ along the x-axis shown in Fig. 3.3 on the left and described by

$$v_x(t) = \begin{cases} \alpha t & t \in [0, t_a] \\ V & t \in [t_a, t_b] \\ \alpha\,(T - t) & t \in [t_b, T] \end{cases} \tag{3.13}$$
$$\text{with} \quad t_a = \frac{V}{\alpha} \quad \text{and} \quad t_b = T - \frac{V}{\alpha}.$$

In the first phase (acceleration) the velocity increases with a constant slope α until a cruising velocity V is reached at time t_a. In the second phase (cruising) the velocity remains constant until a time t_b is reached. Finally, in the third phase (deceleration) velocity decreases with slope $-\alpha$, thus reaching the desired final position x_f. The total hoisting time is denoted T. This

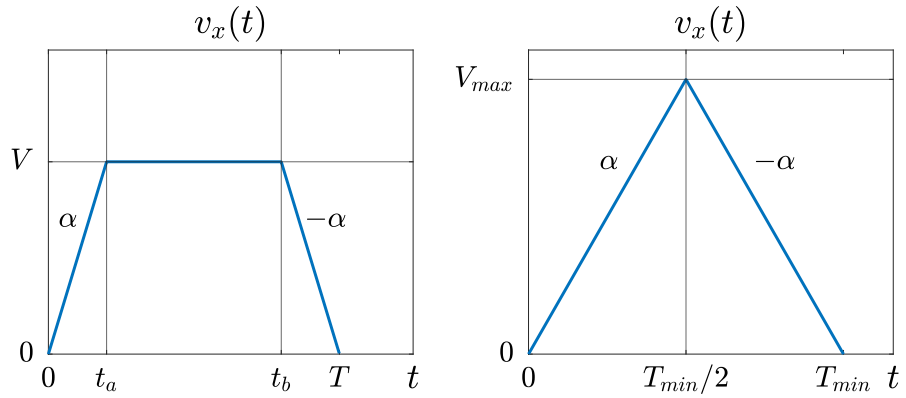

Figure 3.3: Desired velocity profile $v_x(t)$ as a function of time t for a given acceleration α. The limit case on the right corresponds to the minimum time hoisting assuming no bounds on the rope length velocities are given.

velocity profile imposes the following evolution of the load along the x-axis:

$$x(t) = \begin{cases} x_0 + \dfrac{\alpha}{2}t^2 & t \in [0, t_a] \\ x_0 - \dfrac{V^2}{2\alpha} + Vt & t \in [t_a, t_b] \\ x_f - \dfrac{\alpha}{2}(T-t)^2 & t \in [t_b, T] \end{cases} \tag{3.14}$$

whereas the evolution $y(t)$ along the y-axis can be immediately obtained by substituting Eq. (3.14) in Eq. (3.12).
Note that:

$$x_a = x(t_a) = x_0 + \frac{V^2}{2\alpha}, \quad x_b = x(t_b) = x_f - \frac{V^2}{2\alpha}, \tag{3.15}$$

while in the cruising phase (constant velocity) it holds that $x_b - x_a = V(t_b - t_a)$ which implies

$$t_b - t_a = \frac{x_b - x_a}{V} = \frac{x_f - x_0}{V} - \frac{V}{\alpha}, \tag{3.16}$$

from which we obtain

$$T = t_a + (t_b - t_a) + (T - t_b) = \frac{V}{\alpha} + \frac{x_f - x_0}{V}. \tag{3.17}$$

Assuming the parameter α is given, the previous equation allows one to write the hoisting time as a function of the constant cruising velocity V, keeping in mind that the admissible values of V are those that satisfy $t_b - t_a \geq 0$, i.e., according to Eq. (3.16):

$$V \leq V_{max} \stackrel{\text{def}}{=} \sqrt{\alpha(x_f - x_0)}. \tag{3.18}$$

In the admissible range of cruising velocities $V \in (0, V_{max}]$, the hoisting time is always

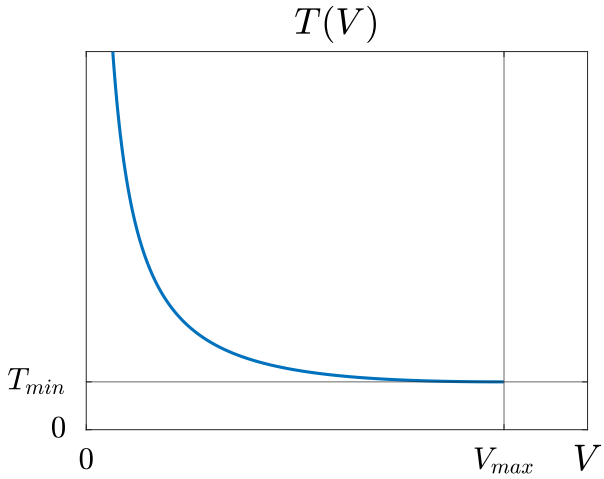

Figure 3.4: Hoisting time T as a function of the constant cruising velocity V.

decreasing, as shown in Fig. 3.4. As expected, the minimum time $T_{min} = 2\sqrt{(x_f - x_0)/\alpha}$ corresponds to the velocity profile described by the plot in the right of Fig. 3.3, which reaches the maximum velocity V_{max}.

In reality, such a minimum time profile may not be admissible because there are also constraints on the rate of change of the rope length that must be satisfied. To take this into account, let us first compute the rope length derivatives, $\dot{L}_1(t)$ and $\dot{L}_2(t)$. From Eq. (3.2) one obtains

$$\dot{L}_1(t) = \frac{d}{dt}L_1(t) = \left(\frac{\partial}{\partial x}L_1 + \frac{\partial}{\partial y}L_1 \cdot \frac{\partial}{\partial x}y\right)\frac{d}{dt}x(t), \tag{3.19}$$

which also taking into account Eq. (3.12) yields

$$\dot{L}_1(t) = \frac{(x - X_1) + 2k\,(x - x_0)\,(y - Y_1)}{\sqrt{(x - X_1)^2 + (y - Y_1)^2}} \cdot v_x = l_1(x)\; v_x, \tag{3.20}$$

similarly, from Eq. (3.3) one obtains

$$\dot{L}_2(t) = \frac{(x - X_2) + 2k\,(x - x_0)\,(y - Y_2)}{\sqrt{(x - X_2)^2 + (y - Y_2)^2}} \cdot v_x = l_2(x)\; v_x. \tag{3.21}$$

The rope derivatives must satisfy for all $t \in [0, T]$ constraints

$$\left|\dot{L}_1(t)\right| \leq L_{1d,max} \quad \text{and} \quad \left|\dot{L}_2(t)\right| \leq L_{2d,max} \tag{3.22}$$

where $L_{1d,max}$ and $L_{2d,max}$ are suitable bounds that depend on the cranes.

3.3.2 Dynamic Solution

We can finally state the problem we want to address.

Problem 1 (Minimum time hoist)

$$\begin{aligned} \min_{V} \quad & T = \frac{V}{\alpha} + \frac{x_f - x_0}{V} \\ \text{s.t.} \quad & \text{(a) } V \in [0, V_{max}] \\ & \text{(b) } \left|\dot{L}_1(t)\right| \leq L_{1d,max}, \quad \forall t \in [0, T] \\ & \text{(c) } \left|\dot{L}_2(t)\right| \leq L_{2d,max}, \quad \forall t \in [0, T] \\ & \text{under Eq. (3.12), (3.13), (3.14).} \end{aligned}$$

As we have observed, in the solution space $T(V)$ is decreasing, hence the optimal value of the decision variable V^* is the maximum value of the cruising velocity that satisfies constraint (a), (b) and (c).

To solve this problem we consider two approaches.

1) Direct approximate solution

Let us consider constraints (b) and (c) which according to Eq. (3.20 - 3.21) can be rewritten and manipulated, for $i = 1, 2$, as follows:

$$\left|\dot{L}_i(t)\right| = |l_i(x)|\,|v_x(t)| \leq l_{i,max} v_x(t) \leq l_{i,max} V \tag{3.23}$$

where $l_{i,max} = \max_{x \in [x_0, x_f]} |l_i(x)|$ only depends on the desired trajectory in Eq. (3.12) and not on the velocity profile. Thus constraints (b) and (c) are satisfied when

$$V \leq \frac{L_{1d,max}}{l_{1,max}} \quad \text{and} \quad V \leq \frac{L_{2d,max}}{l_{2,max}}, \tag{3.24}$$

and a direct approximate, although possibly suboptimal, solution of Problem 1 is

$$V = \min\left(V_{max}, \frac{L_{1d,max}}{l_{1,max}}, \frac{L_{2d,max}}{l_{2,max}}\right). \tag{3.25}$$

This procedure is outlined in the next Algorithm 1.

Algorithm 1: Direct Approximate Solution for Minimum-Time Hoisting

Input: Initial and final positions $(x_0, y_0), (x_f, y_f)$; trajectory parameters k, x_s, y_s; crane geometry $(X_i, Y_i), i = 1, 2$; max cable speeds $L_{1d,\max}, L_{2d,\max}$; acceleration α.

Output: Approximate cruising velocity V and total hoisting time T.

Compute $V_{\max} \leftarrow \sqrt{\alpha(x_f - x_0)}$;

for *each* x *in* $[x_0, x_f]$ **do**

  Compute $y(x) \leftarrow k(x - x_s)^2 + y_s$;

  for $i = 1, 2$ **do**

    Compute:

$$l_i(x) = \frac{(x - X_i) + 2k(x - x_0)(y - Y_i)}{\sqrt{(x - X_i)^2 + (y - Y_i)^2}}$$

Compute

$$l_{1,\max} = \max_{x \in [x_0, x_f]} |l_1(x)|, \quad l_{2,\max} = \max_{x \in [x_0, x_f]} |l_2(x)|$$

Estimate:

$$V_1 \leftarrow \frac{L_{1d,\max}}{l_{1,\max}}, \quad V_2 \leftarrow \frac{L_{2d,\max}}{l_{2,\max}}$$

if $V_1 > 0$ *and* $V_2 > 0$ **then**

  Set $V \leftarrow \min(V_{\max}, V_1, V_2)$;

  Compute:

$$T \leftarrow \frac{V}{\alpha} + \frac{x_f - x_0}{V^*}$$

else

  Report: No admissible velocity found ;

2) Line search optimization

Given a specific value of V, the corresponding velocity profile $v_x(t)$ and the position trajectories $x(t)$ and $y(t)$ for $t \in [0, T]$ can be computed from Eq. (3.12 - 3.14). By substituting these trajectories into Eq. (3.20 - 3.21), the time histories of the cable velocity profiles $\dot{L}_1(t)$ and $\dot{L}_2(t)$ are obtained. These profiles allow a direct verification of whether the cable velocity constraints (b) and (c) are satisfied at each time instant.

The procedure begins with an initial maximum velocity $V = V_{\max}$, which represents the upper bound of the admissible motion speed. The algorithm then iteratively reduces V in uniform or adaptive steps of a suitable size, recalculating the corresponding trajectories and cable velocities at each iteration. At every step, the algorithm checks whether constraints (b) and (c) are satisfied throughout the entire motion duration $t \in [0, T]$.

Once both constraints are fulfilled, the corresponding velocity V^* and the associated total motion time T^* are recorded as the optimal solution. This iterative *line search optimization method* thus ensures convergence toward the minimum feasible duration of motion under the given kinematic and cable-velocity constraints. The precision of the obtained optimal pair (T^*, V^*) can be controlled by the choice of the step size and termination tolerance, offering a balance between computational efficiency and accuracy. This procedure is outlined in the next Algorithm 2.

3.4 Simulation and Analysis

To assess and compare the two methods, simulations are performed on the following dual-crane hoisting case study. The boom anchor points of the two cranes are set to the following values

$$\begin{aligned} X_1 &= 15m, \quad Y_1 = 60m, \\ X_2 &= 50m, \quad Y_2 = 65m, \quad D = 80\text{m}. \end{aligned}$$

The maximal allowed cable velocity values are taken the same for both cranes, i.e.

$$L_{1d,max} = L_{2d,max} = 0.2m/s \tag{3.26}$$

The box needs to be lifted from the ground $y_0 = 0m$ to a height of $y_f = 40m$ for installation and then released downward. Therefore, the following parameters are set for the parabolic

Algorithm 2: Line Search Optimization for Minimum-Time Hoisting

Input: Initial and final positions $(x_0, y_0), (x_f, y_f)$; trajectory parameters k, x_s, y_s; boom anchor (X_i, Y_i), i=1,2; max cable speeds $L_{1d,\max}, L_{2d,\max}$; acceleration α.

Output: Optimal cruising velocity V^* and total hoisting time T^*.

Compute $V_{\max} \leftarrow \sqrt{\alpha(x_f - x_0)}$;

for *each* V *in decreasing order from* $V_{\max}$ *to* 0.001 **do**

  $t_a \leftarrow V/\alpha, \quad T \leftarrow V/\alpha + (x_f - x_0)/V, \quad t_b \leftarrow T - V/\alpha$;

  for *each* t *in* $[0, T]$ **do**

    Compute $x(t)$ via:

$$x(t) = \begin{cases} x_0 + \frac{1}{2}\alpha t^2, & t < t_a \\ x_0 - \frac{V^2}{2\alpha} + Vt, & t_a \le t < t_b \\ x_f - \frac{1}{2}\alpha(T-t)^2, & t \ge t_b \end{cases}$$

    $y(t) \leftarrow k(x - x_0)^2 + y_0, \quad v_x(t) \leftarrow \dot{x}(t)$;

    for $i = 1, 2$ **do**

      Compute:

$$\dot{L}_i(t) = \frac{(x - X_i) + 2k(x - x_0)(y - Y_i)}{\sqrt{(x - X_i)^2 + (y - Y_i)^2}} \cdot v_x(t)$$

    if $|\dot{L}_1(t)| > L_{1d,\max}$ *or* $|\dot{L}_2(t)| > L_{2d,\max}$ **then**

      break (constraints violated) ;

  if *no violations occurred for all* t **then**

    $V^* \leftarrow V, \quad T^* \leftarrow T$;

    break (optimal found) ;

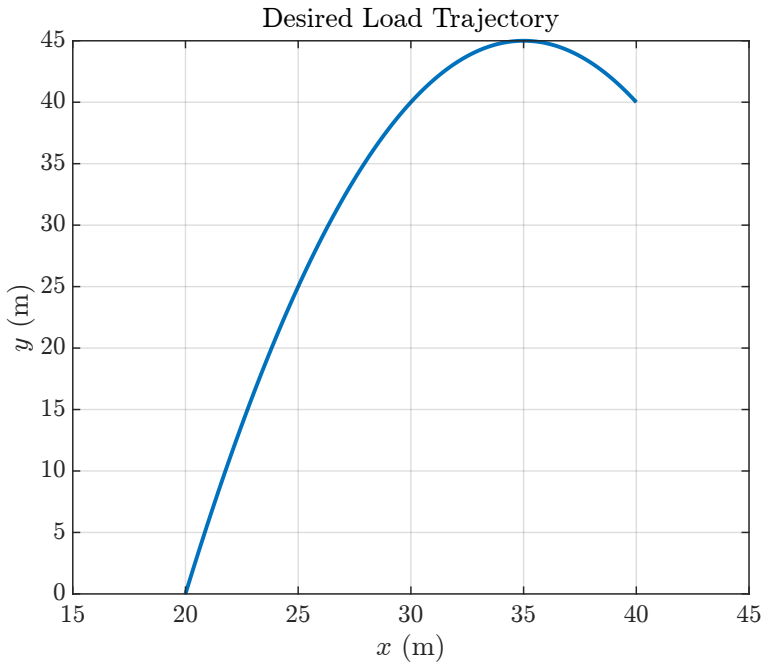

Figure 3.5: Desired load path.

load lifting trajectory in Eq. (3.12)

$$\begin{aligned} x_0 &= 20m, \quad x_f = 40m, \\ x_s &= 35m, \quad y_s = 45m, \\ k &= -0.2. \end{aligned}$$

The desired load trajectory is displayed in Fig. 3.5. The acceleration/deceleration parameter of the chosen horizontal load velocity Eq. (3.14) is set as $\alpha = 0.5m/s^2$. According to Eq. (3.18), this yields the maximal allowed cruising velocity

$$V_{max} = 3.1623m/s. \tag{3.27}$$

According to Eq. (3.17), setting $V = V_{max}$ would yield a total travel time $T = 12.64s$ and the load coordinates vs. time displayed in Fig. 3.6. The resulting rope lengths and rope velocities are displayed in Fig. 3.7, and both $\dot{L}_1(t)$ and $\dot{L}_2(t)$ turn out to heavily violate the admissible bounds in Eq. (3.22).

Let us then apply the two methods previously outlined to compute the largest possible value of V which makes the constraints Eq. (3.22) satisfied.

Functions $l_1(x)$ and $l_2(x)$ are displayed in Fig. 3.8. The bounds $l_{1,max} = 5.913$ and $l_{2,max} = 5.838$ are found at the initial position. Evaluating V according to Eq. (3.25) yields

$$V = 0.0338m/s \tag{3.28}$$

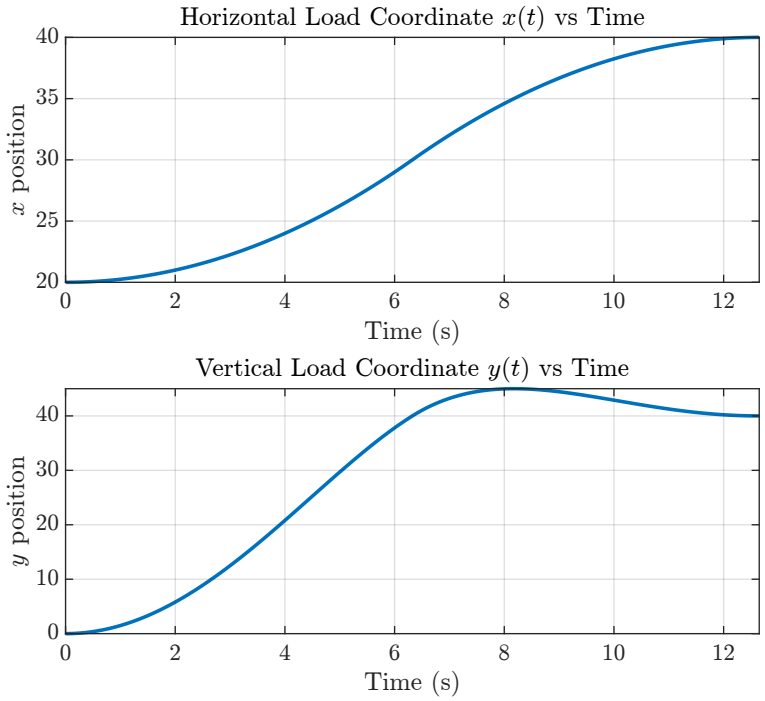

Figure 3.6: Actual load path with $V = V_{max}$.

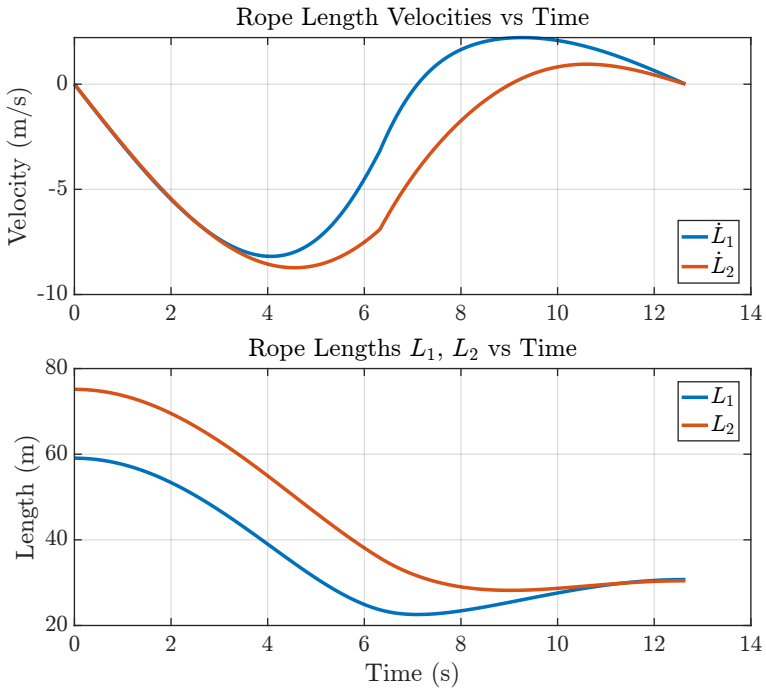

Figure 3.7: Rope velocities (up) and rope lengths (down) with $V = V_{max}$.

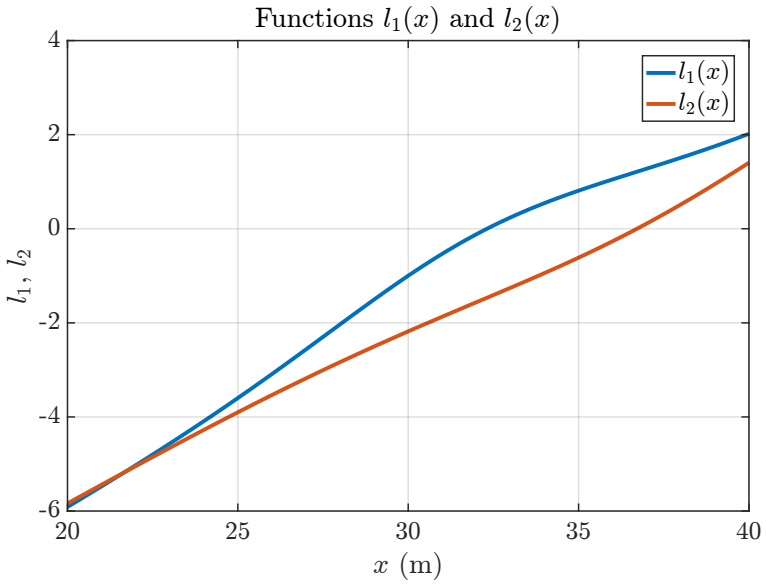

Figure 3.8: Functions $l_1(x)$ and $l_2(x)$ with $V = 0.0338m/s$.

Fig. 3.9 shows the horizontal velocity of the load along the time and x-axis. The travel time is $T = 591.43$ s, as can be seen from Fig. 3.10 and Fig. 3.11 which display the time evolution of the load coordinates and of the cable lengths along with the corresponding derivatives. As observed in Fig. 3.11, the rope attains its maximum velocity after a very short transient. The value $x_a = x(t_a) = 20.0008$ can be obtained based on Eq. (3.15), and it turns out to be very close to the initial position. It can be seen constraints Eq. (3.22) are actually fulfilled along the entire travel of the load. Since the constant cruising velocity V is reached at a position x_a very close to the initial position where $|l_1(x)|$ is maximal, the iterative line search optimization procedure gives a result that is almost coincident with that in Eq. (3.28), which $V^* = 0.0338m/s^2, T^* = 591.14s$, meaning that the direct approximate solution is almost optimal in this example.

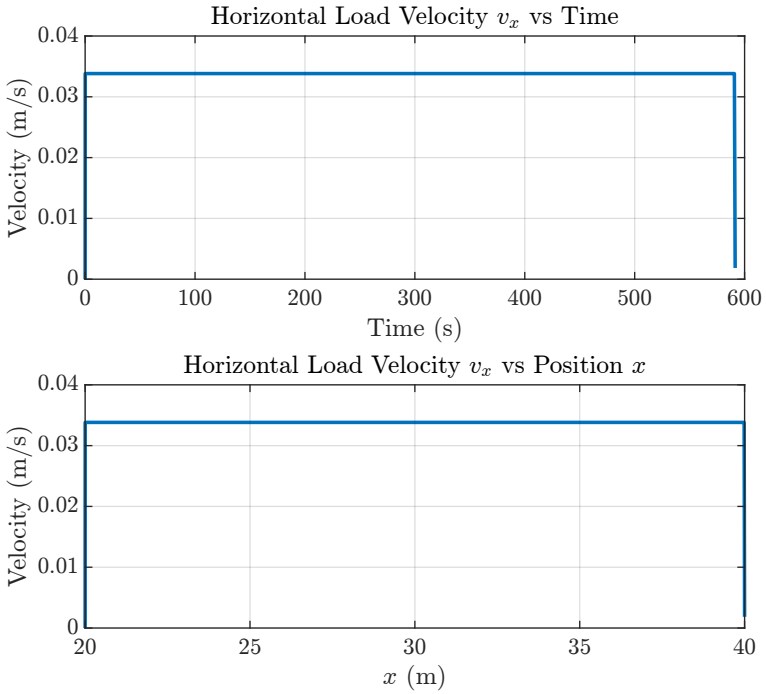

Figure 3.9: Horizontal load velocity v_x vs. time (up) and vs. position x (down) with $V = 0.0338m/s$.

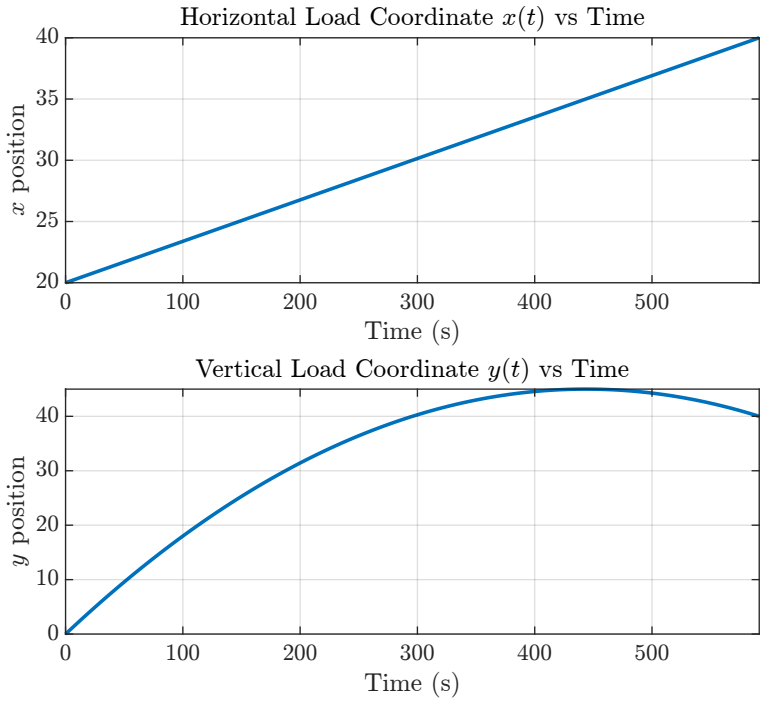

Figure 3.10: Actual load path with $V = 0.0338m/s$.

However, a closer inspection of Fig. 3.9 reveals that although the load velocity becomes very small when reaching the final position (x_f, y_f), it does not exactly reach zero. To ensure that the load velocity is also zero upon arrival at the target position, an improved version of the

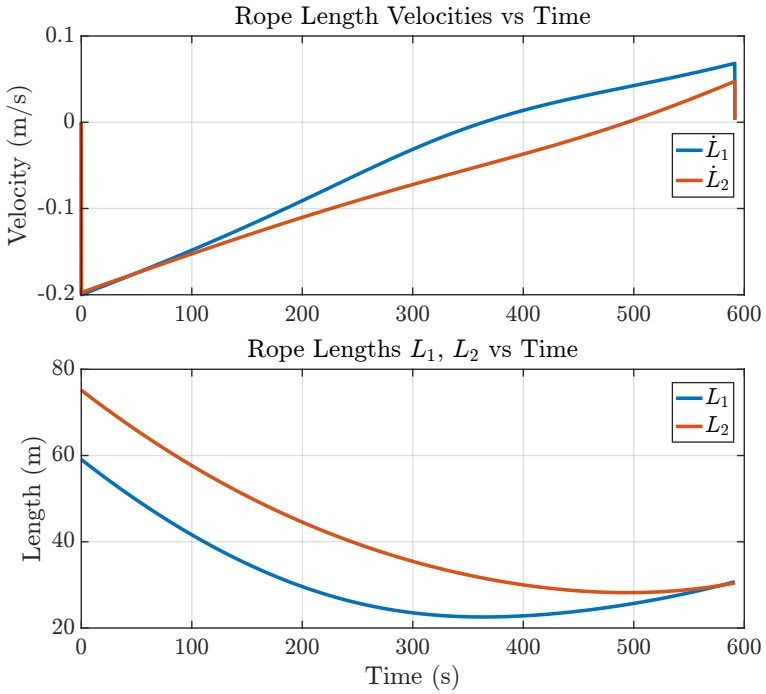

Figure 3.11: Rope velocities (up) and rope lengths (down) with $V = 0.0338m/s$.

above method is considered. According to the direct approximate solution above, now it does not longer consider a pre-specified V_{max} velocity profile, but it instead changes the velocity value dynamically, the following equation is introduced

$$V_x(x) = A(x) \min\left(\frac{L_{1d,max}}{|l_1(x)|}, \frac{L_{2d,max}}{|l_2(x)|}\right). \tag{3.29}$$

where

$$A(x) = \begin{cases} 1, & x \in [x_0,\, x_f - \delta], \\ \dfrac{\sqrt{\delta^2 - (x - x_f + \delta)^2}}{\delta}, & x \in [x_f - \delta,\, x_f]. \end{cases} \tag{3.30}$$

with

$$\delta = \frac{x_f - x_0}{D_f} \tag{3.31}$$

the parameter D_f is assigned a suitable positive value based on the difference between x_f and x_0.

In this approach, the velocity profile is not pre-assigned (as in Methods 1 and 2), but instead computed adaptively along the trajectory based on the instantaneous values of the rope functions $l_1(x)$ and $l_2(x)$. At every load position $x \in [x_0, x_f]$, the rope speed constraints

$$|\dot{L}_1(x)| \leq L_{1d,\max}, \quad |\dot{L}_2(x)| \leq L_{2d,\max}, \tag{3.32}$$

must be satisfied. By the chain rule, these constraints imply:

$$|\dot{L}_i(x)| = |l_i(x)| \cdot V_x(x) \leq L_{id,\max}, \quad i = 1, 2 \tag{3.33}$$

Solving for $V_x(x)$, we obtain the maximum admissible velocity at each x

$$V_x(x) \leq \min\left(\frac{L_{1d,\max}}{|l_1(x)|}, \frac{L_{2d,\max}}{|l_2(x)|}\right). \tag{3.34}$$

To enforce a smooth stop of the load at the final position x_f, the velocity profile is shaped using a modulation function Eq. (3.30). This ensures that $V_x(x)$ gradually decreases to zero near x_f, guaranteeing a smooth and physically feasible stop without violating the rope velocity limits. The complete velocity profile is integrated forward starting from $x = x_0$ to obtain the load position, velocity, and rope length trajectories. This procedure is outlined in the next Algorithm 3.

Algorithm 3: Adaptive Velocity Shaping for Minimum-Time Hoisting

Input: Initial and final positions $(x_0, y_0), (x_f, y_f)$; trajectory parameters k, x_s, y_s; boom anchor (X_i, Y_i), i=1,2; max cable speeds $L_{1d,\max}, L_{2d,\max}$; D_f; maximum Evolution time $T_{\max}$.

Output: Velocity $V_x(t)$, arrival time T_a

Initialize: $x \leftarrow x_0$, $V_x \leftarrow 0$;

Compute $\delta \leftarrow \dfrac{x_f - x_0}{D_f}$;

Define shaping function:

$$A(x) = \begin{cases} 1, & x \in [x_0,\ x_f - \delta] \\ \dfrac{\sqrt{\delta^2 - (x - x_f + \delta)^2}}{\delta}, & x \in [x_f - \delta,\ x_f] \end{cases}$$

while $x < x_f$ *and* $t < T_{\max}$ **do**

$y \leftarrow k(x - x_0)^2 + y_0$

Compute:

$$l_i(x) = \frac{(x - X_i) + 2k(x - x_0)(y - Y_i)}{\sqrt{(x - X_i)^2 + (y - Y_i)^2}} \quad \text{for } i = 1, 2$$

Compute local maximum velocity:

$$V_x \leftarrow A(x) \cdot \min\left(\frac{L_{1d,\max}}{|l_1(x)|}, \frac{L_{2d,\max}}{|l_2(x)|}\right)$$

Compute:

$$L_i \leftarrow \sqrt{(x - X_i)^2 + (y - Y_i)^2} \quad \text{for } i = 1, 2$$

$t \leftarrow T_{max}$

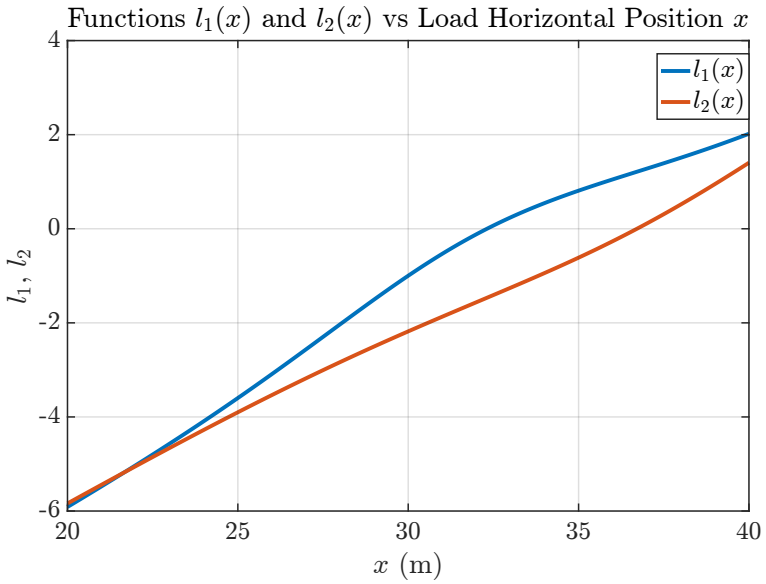

Figure 3.12: Functions $l_1(x)$ and $l_2(x)$ with $T_a = 269.7s$.

To verify the effectiveness of the adaptive velocity shaping method, the previous case study is simulated again while keeping all parameter settings and the lifting trajectory unchanged. The system evolution time $T_{max} = 280s$.

Functions $l_1(x)$ and $l_2(x)$ are displayed in Fig. 3.12. Since the desired load trajectory remains unchanged, the functions $l_1(x)$ and $l_2(x)$ are identical to those in the previous case. Fig. 3.13 shows the velocity of the load along the x-axis and time, it can be observed that the velocity becomes zero when the load reaches the final position, and that the motion consists only of an acceleration phase followed by a deceleration phase, without any constant-velocity interval. The travel time is $T_a = 269.7s$, as can be seen from Fig. 3.14 and Fig. 3.15 which display the time evolution of the load coordinates and of the cable lengths along with the corresponding derivatives. As observed in Fig. 3.15, the rope attains its maximum velocity after a very short transient. It can be seen that the constraints in Eq. (3.22) are fully satisfied throughout the entire motion of the load, and that L_1 and L_2 remain close to their maximum allowable cable velocities for most of the operation time. This demonstrates that the adaptive velocity shaping method significantly reduces the lifting duration compared with Method 1 and Method 2.

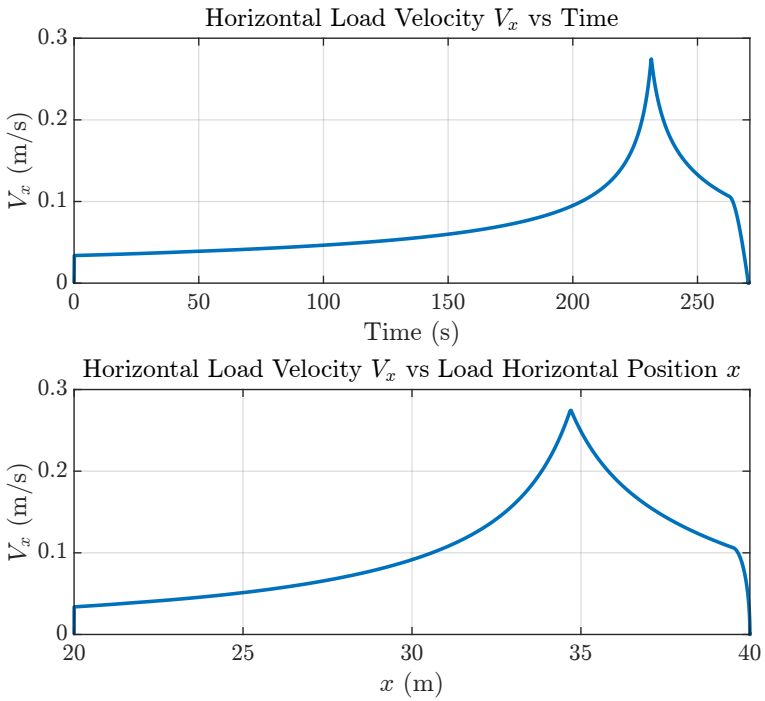

Figure 3.13: Horizontal load velocity V_x vs. time (up) and V_x vs. x-axis(down) with T_a = 269.7s.

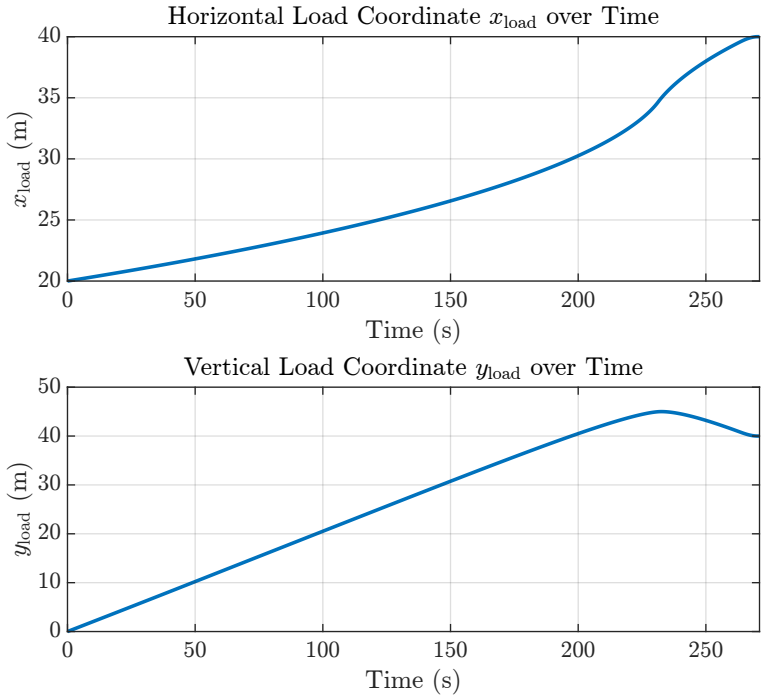

Figure 3.14: Actual load path with $T_a = 269.7s$.

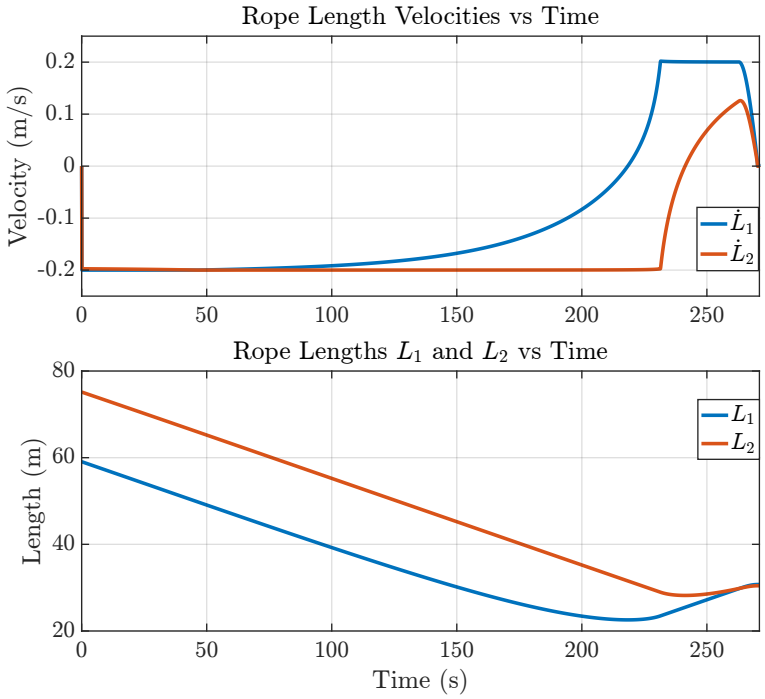

Figure 3.15: Rope velocities (up) and rope lengths (down) with $T_a = 269.7s$.

This chapter investigates the cooperative hoisting of a point-mass load by a dual crawler crane system under cable velocity constraints, aiming to achieve minimum-time lifting along a predefined trajectory. The study begins with a kinematic analysis of the point-mass load system, through which the relationship between the cable lengths and the load position is derived. Based on this kinematic relation, desired motion trajectories and corresponding velocity profiles are designed to enable the load to complete the lifting task as quickly as possible while strictly satisfying the cable velocity limits.

To achieve this objective, a direct approximation method is first proposed. This approach is analytically derived and provides a conservative estimate of the cruising velocity by considering the minimum feasible speed imposed by the cable velocity constraints. By computing the maximum values of the cable dynamic factors $l_1(x)$ and $l_2(x)$ along the path, a maximum admissible cruising velocity V that satisfies the constraints can be obtained. The advantage of this method lies in its simplicity, closed-form solution, and guaranteed compliance with the velocity limits. However, this approach is conservative, as it does not account for whether the worst-case condition actually occurs along the trajectory, which may lead to an underestimation of the system's performance.

To improve accuracy, a line search optimization method is also developed. Starting from the maximum cruising velocity defined by a trapezoidal velocity profile, the algorithm iteratively reduces the cruising speed with an appropriate step size until the cable velocity constraints are fully satisfied. This method provides a higher level of precision and can approxi-

mate the optimal solution, though at the expense of increased computational cost.

Both methods are tested on the same case study, and the simulation results show nearly identical outcomes. This indicates that, in the considered case, the direct approximation method yields an almost optimal solution. Nevertheless, at the optimal cruising velocity, the load still retains a very small residual velocity when reaching the final position. To address this issue and further reduce the lifting time, an Adaptive Velocity Shaping method is proposed as an enhancement of the direct approximation approach. This method abandons the use of a predefined velocity profile and instead employs a dynamic velocity adjustment strategy based on real-time position information. By introducing a position dependent adjustment function, the load velocity along the x-axis is continuously adapted according to the instantaneous values of the cable dynamic factors $l_1(x)$ and $l_2(x)$. This ensures that the cable velocity constraints are always satisfied while maintaining a relatively high motion speed and enabling a smooth deceleration as the load approaches the target position. Simulation results for the same case confirm that, compared with the previous methods, the Adaptive Velocity Shaping approach substantially reduces the total lifting time.

Chapter 4

Dual crawler crane system with rigid-rod load

4.1 System Description and Assumptions

In Chapter 3, a dual crane system with a point-mass load is constructed. In this scenario, the load's small volume allows it to be approximated as a point-mass. However, in practical engineering applications, the loads lifted by dual crane systems are typically characterized by large mass and volume. This is common in industries such as chemical processing, construction, and energy. As illustrated in Fig. 4.1, dual cranes are commonly employed for installing large structures such as chemical reaction towers and architectural components. These loads typically have considerable length, and therefore cannot be modeled as point-mass; instead, their attitude variations during the hoisting process must be taken into account. For this type of load, previous studies have generally modeled it as a rigid-rod.

(a) Reactor tower (b) Architectural components

Figure 4.1: Cooperative hoisting of reactor tower (left) and architectural components (right) with DCCs.

From a theoretical modeling perspective, the rigid-rod representation adopted in this chapter can be regarded as a natural extension of the point-mass model introduced in Chapter 3. In the point-mass formulation, the load orientation is implicitly neglected, and the system dynamics are fully described by the translational motion of the load center. This modeling choice is appropriate when the load dimensions are small compared to the crane span or when attitude variations are negligible. By contrast, the rigid-rod model explicitly introduces the load orientation as an additional generalized coordinate, allowing attitude dynamics to be captured during cooperative hoisting. It is worth noting that the point-mass model can be recovered as a special

case of the rigid-rod model when the load length tends to zero or when the orientation is constrained to remain constant. Therefore, the two models are not conceptually disconnected, but rather represent different levels of abstraction within a unified modeling framework. The motivation for introducing the more detailed rigid-rod model in this chapter is to address installation scenarios in which load orientation plays a critical role, such as the lifting and positioning of elongated industrial components. In these cases, neglecting attitude dynamics may lead to inaccurate predictions of system behavior and insufficient control performance, thereby justifying the increased modeling complexity.

In this study, the cooperative hoisting process involving two cranes is analyzed under the following simplifying assumptions, which are commonly adopted in similar crane related studies. Meanwhile, Assumptions 3.1 and 3.2 presented in Chapter 2 are also applicable to this chapter.

Assumption 4.1 *The load is modeled as a rigid rod whose deformation under external forces is negligible. In other words, it is assumed to undergo neither bending nor elongation during the hoisting process.*

A sketch of the two cooperating crawler cranes in the vertical $x - y$ plane is shown in Fig. 4.2, whose variables and parameters are defined in Table 4.1.

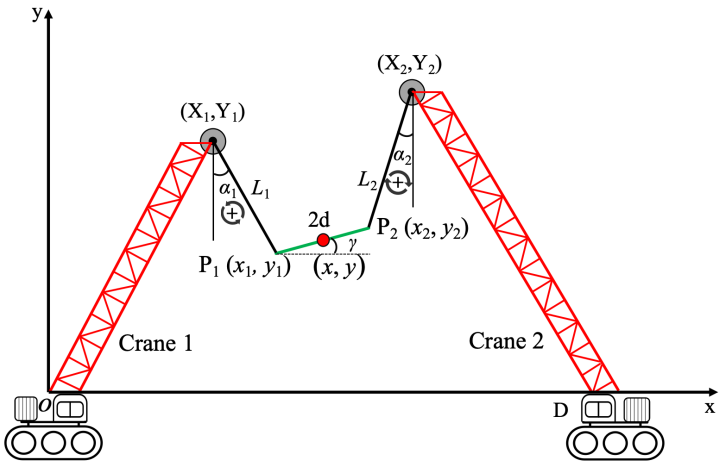

Figure 4.2: Schematic representation of DCCs with rigid-rod load.

Let (X_1, Y_1) and (X_2, Y_2) be the coordinates of fixed boom anchor points. The load is a rigi-rod of total length $2d > 0$, with center at (x, y) and attitude γ (measured from the x-axis, positive counterclockwise). Note that positive sense of angle α_1 is defined counterclockwise, whereas for angle α_2 it is defined clockwise. In this study, the primary focus is on the variations in the load's position and orientation during motion. The two endpoints of the load, denoted as P_1 and P_2, are connected to the ends of the two hoisting cables. To accurately describe the

Table 4.1: Variables and parameters.

Symbols	Meanings	Units
L_1, L_2	rope length	m
α_1, α_2	cable angles with the vertical direction	rad
γ	load angle with the horizontal direction	rad
(x, y)	coordinates of the load center	m
$(X_1, Y_1), (X_2, Y_2)$	coordinates of the boom anchor	m
$(x_1, y_1), (x_2, y_2)$	coordinates of P_1, P_2	m
$2d$	load length	m
D	distance between two cranes	m
m	payload mass	kg
g	gravity constant	m/s^2

load's position, its center coordinates (x, y) are typically used, while its orientation is represented by the angle γ. Meanwhile, under normal operating conditions, the load should remain within a reasonable working region. The admissible load positions within the workspace are determined by the presence of tension in both cables, so that both cranes are carrying part of the load. This region is analytically described as follows:

$$\begin{cases} \alpha_1, \alpha_2 \in \left(0, \dfrac{\pi}{2}\right), \ \gamma \in \left(-\dfrac{\pi}{2}, \dfrac{\pi}{2}\right), \\ X_1 < x_1 < x < x_2 < X_2, \\ 0 \leq \min(y_1, y_2) \leq y \leq \max(y_1, y_2) < \min(Y_1, Y_2). \end{cases}$$

Although the admissible workspace is defined as an open set, boundary configurations corresponding to $\gamma = \pm\pi/2$ can be considered as limiting cases, which are relevant in practical installation tasks.

4.2 Kinematic analysis

After defining the system configuration and assumptions in Section 4.1, the next step is to analyze the kinematic characteristics of the DCC system with a rigid-rod load. Unlike the point-mass model introduced in Chapter 3, the rigid-rod load exhibits an additional rotational degree of freedom, which must be explicitly considered when describing the system motion. This introduces coupling between the translational motion of the load's center and its rotational orientation, resulting in more complex geometric relationships among the cable lengths, the anchor points, and the load endpoints.

The purpose of this section is to establish the kinematic framework that captures these coupled relationships. By deriving the geometric and motion constraints, the position and orientation of the rigid load can be expressed in terms of the cable lengths and the crane configurations. These constraints form the foundation for the subsequent dynamic modeling in

Section 4.3 and the order reduction process discussed in Section 4.4.

Accordingly, Section 4.2 is organized as follows. Section 4.2.1 presents the geometric constraints derived from the planar configuration of the system, while Section 4.2.2 formulates the motion constraints that relate the cable velocities to the load's translational and rotational motion.

4.2.1 Geometric Constraints

By examining Fig. 4.2 and analyzing the geometric relationships between the boom tips and the two endpoints of the load along the x-axis and y-axis

$$x_2 - x_1 = 2d\cos\gamma, \tag{4.1}$$

$$y_2 - y_1 = 2d\sin\gamma. \tag{4.2}$$

since

$$\begin{bmatrix} x_1 \\ y_1 \end{bmatrix} = \begin{bmatrix} X_1 \\ Y_1 \end{bmatrix} + L_1 \begin{bmatrix} \sin\alpha_1 \\ -\cos\alpha_1 \end{bmatrix}, \tag{4.3}$$

$$\begin{bmatrix} x_2 \\ y_2 \end{bmatrix} = \begin{bmatrix} X_2 \\ Y_2 \end{bmatrix} - L_2 \begin{bmatrix} \sin\alpha_2 \\ \cos\alpha_2 \end{bmatrix}. \tag{4.4}$$

By combining Eq. (4.1 – 4.4), the following geometric constraint equations can be obtained

$$X_1 - X_2 + L_1\sin\alpha_1 + L_2\sin\alpha_2 + 2d\cos\gamma = 0, \tag{4.5}$$

$$Y_1 - Y_2 - L_1\cos\alpha_1 + L_2\cos\alpha_2 + 2d\sin\gamma = 0. \tag{4.6}$$

The constraint equations in Eq. (4.5 – 4.6) do not explicitly include the coordinates of the load's center point (x, y). In this case, the relationship between the load's center and its two endpoints, P_1 and P_2, can be established using the following expressions

$$\begin{bmatrix} x_1 \\ y_1 \end{bmatrix} = \begin{bmatrix} x \\ y \end{bmatrix} - d \begin{bmatrix} \cos\gamma \\ \sin\gamma \end{bmatrix}, \tag{4.7}$$

$$\begin{bmatrix} x_2 \\ y_2 \end{bmatrix} = \begin{bmatrix} x \\ y \end{bmatrix} + d \begin{bmatrix} \cos\gamma \\ \sin\gamma \end{bmatrix}. \tag{4.8}$$

Cable lengths are the Euclidean distances from the anchors to the corresponding endpoints:

$$L_1 = \sqrt{(x_1 - X_1)^2 + (y_1 - Y_1)^2}, \qquad L_2 = \sqrt{(x_2 - X_2)^2 + (y_2 - Y_2)^2}. \tag{4.9}$$

By substituting Eq. (4.7 - 4.8) into Eq. (4.9), the following explicit expressions can be obtained

$$L_1 = \sqrt{(x - d\cos\gamma - X_1)^2 + (y - d\sin\gamma - Y_1)^2}, \tag{4.10}$$

$$L_2 = \sqrt{(x + d\cos\gamma - X_2)^2 + (y + d\sin\gamma - Y_2)^2}. \tag{4.11}$$

From the geometric relations in Eq. (4.10 – 4.11), the cable lengths are uniquely determined by the configuration (x, y, γ). We therefore define the forward–kinematics mapping

$$f_{L_{1,2}} : (x, y, \gamma) \in \mathbb{R}^3 \mapsto (L_1, L_2) \in \mathbb{R}^2,$$

compactly written as

$$(L_1,\ L_2) = f_{L_{1,2}}(x, y, \gamma), \tag{4.12}$$

with the component wise formulas provided in Eq. (4.10 – 4.11).

At this stage, the inverse kinematics of the system is considered. Previously, a unique pair of cable lengths (L_1, L_2) could be determined once the configuration (x, y, γ) was specified. The current objective is to determine the load's coordinates (x, y) when the configuration (L_1, L_2, γ) is given. As illustrated in Fig. 4.3, the cable lengths L_1 and L_2 are given. According

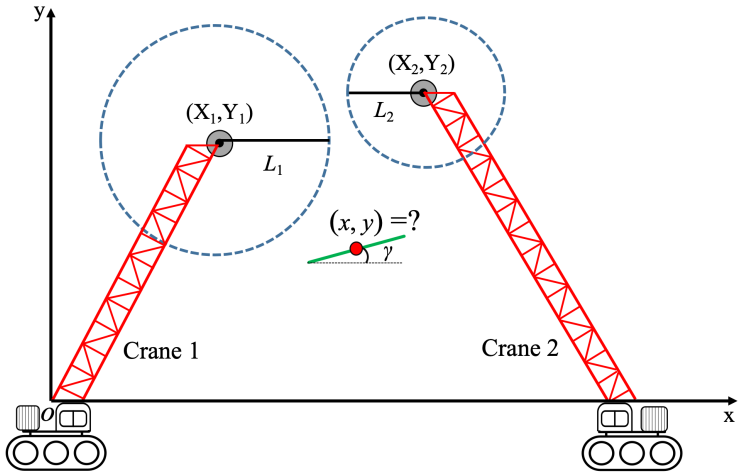

Figure 4.3: Schematic representation of DCCs.

to Assumption 3.1, the possible trajectories of the cable ends can be represented by two circles centered at the crane anchor points, with radii L_1 and L_2, respectively. Given that the load orientation γ is also specified, determining the coordinates (x, y) requires translating the load while keeping γ constant so that its two endpoints lie on the corresponding dashed circles. It is evident that only one configuration satisfies these geometric conditions.

To verify the above conclusion in an algebraic form, first recalling the geometric constraint Eq. (4.5 – 4.6), when the configuration (L_1, L_2, γ) is specified, the solutions for α_1 and α_2 can

be obtained by combining them with the following Pythagorean identities.

$$\sin^2\alpha_1 + \cos^2\alpha_1 = 1, \qquad \sin^2\alpha_2 + \cos^2\alpha_2 = 1. \tag{4.13}$$

From a geometric standpoint, Eq. (4.5 – 4.6) admit two symmetric configurations of the dual crane system. These two branches correspond to the rigid load being located either above or below the crane tips. Mathematically, both satisfy the same geometric constraints, since the system can be mirrored with respect to the line connecting the two crane anchors. However, in practical operations the load is always suspended below the cranes under gravity, and the cables must remain in tension. Consequently, only the lower configuration is physically admissible, satisfying the workspace constraint $\alpha_1, \alpha_2 \in \left(0, \frac{\pi}{2}\right)$. Therefore, when restricted to the feasible workspace, the solution (α_1, α_2) of Eq. (4.5 – 4.6) and Eq. (4.13) is unique, and α_1 and α_2 can thus be regarded as dependent variables of L_1, L_2, and γ, defined as follows by solving the same set of equations

$$\alpha_1 = h_1(L_1, L_2, \gamma), \tag{4.14}$$

$$\alpha_2 = h_2(L_1, L_2, \gamma). \tag{4.15}$$

then present alternative coordinate expressions for the two endpoints of the load, distinct from Eq. (4.7 - 4.8)

$$\begin{bmatrix} x_1 \\ y_1 \end{bmatrix} = \begin{bmatrix} X_1 \\ Y_1 \end{bmatrix} + L_1 \begin{bmatrix} \sin\alpha_1 \\ -\cos\alpha_1 \end{bmatrix}, \tag{4.16}$$

$$\begin{bmatrix} x_2 \\ y_2 \end{bmatrix} = \begin{bmatrix} X_2 \\ Y_2 \end{bmatrix} - L_2 \begin{bmatrix} \sin\alpha_2 \\ \cos\alpha_2 \end{bmatrix}. \tag{4.17}$$

the coordinates of the load's center point can be readily obtained as follows

$$\begin{bmatrix} x \\ y \end{bmatrix} = \frac{1}{2} \begin{bmatrix} X_1 + X_2 + L_1\sin\alpha_1 - L_2\sin\alpha_2 \\ Y_1 + Y_2 - L_1\cos\alpha_1 - L_2\cos\alpha_2 \end{bmatrix}. \tag{4.18}$$

This implies that once the configuration (L_1, L_2, γ) is given, α_1 and α_2 are uniquely determined, which in turn means that the coordinates of the load's center point (x, y) are also uniquely defined. In other words, (α_1, α_2) and (x, y) are equivalent representations of the system configuration. We therefore define the inverse kinematics mapping

$$f_{x,y} : \ (L_1, L_2, \gamma) \in \mathbb{R}^3 \ \mapsto \ (x, y) \in \mathbb{R}^2,$$

compactly written as

$$(x,\ y) = f_{x,y}(L_1, L_2, \gamma), \tag{4.19}$$

with the component-wise formulas provided in Eq. (4.5 – 4.6), Eq. (4.13) and Eq. (4.18).

Through kinematic analysis, the DCC system with a rigid rod load, described by five

variables (x, y, γ, L_1, L_2), possesses three degrees of freedom. Therefore, once any three of these variables are known, the remaining two can be uniquely determined.

4.2.2 Motion Constraints

The full system is described by five degrees of freedom (x, y, γ, L_1, L_2) but possesses only three degrees of freedom due to two geometric constraints imposed by the cables. When the cable lengths L_1 and L_2 are fixed, there can be still be infinite possible values of (x, y, γ) compatible with (L_1, L_2), the remaining configuration variables (x, y, γ) are not independent but must satisfy both constraints simultaneously. Hence, all possible configurations form a one-dimensional subset of $\mathbb{R}^3$, denoted as

$$(x, y, \gamma) = g(L_1, L_2) \subset \mathbb{R}^3, \tag{4.20}$$

which defines a manifold of dimension one, a continuous curve (topologically equivalent to a line segment) along which the system can evolve. Such a manifold represents all feasible positions and attitudes of the load consistent with the assigned cable lengths.

To provide a more intuitive understanding of how this one dimensional geometric manifold evolves, a graphical illustration is presented through the following example:

$$\begin{aligned} &X_1 = 20 \text{ m}, \quad Y_1 = 90 \text{ m}, \\ &X_2 = 100 \text{ m}, \quad Y_2 = 100 \text{ m}, \quad D = 110 \text{ m}. \end{aligned}$$

After defining the positions of the two boom anchor points (X_1, Y_1) and (X_2, Y_2), as well as the inter crane distance D, the cable lengths are fixed at $L_1 = 60$ m and $L_2 = 70$ m. Considering the workspace limitation, the orientation angle γ is constrained within the range $(-\pi/2, \pi/2)$. Within this range, 18 evenly spaced sample points are selected to observe the geometric evolution of the system as γ varies while L_1 and L_2 remain constant. Based on the inverse kinematic relations and Eq. (4.19), the corresponding load center positions (x, y) are computed in MATLAB. Fig. 4.4 illustrates the overall geometric configuration of the DCC system and the resulting one dimensional manifold of the load center under constant cable lengths.

The two dashed circles in Fig. 4.4 represent the geometric constraints defined by the fixed cable lengths L_1 and L_2, centered at the boom anchors (X_1, Y_1) and (X_2, Y_2), respectively. For each orientation $\gamma \in (-\pi/2, \pi/2)$, the rigid rod load is positioned such that both of its cable attachment points lie on the corresponding circular constraints defined by L_1 and L_2. The resulting configurations, drawn as thin dashed lines, illustrate the possible geometric poses of the load consistent with the fixed cable lengths. The orange dots mark the corresponding

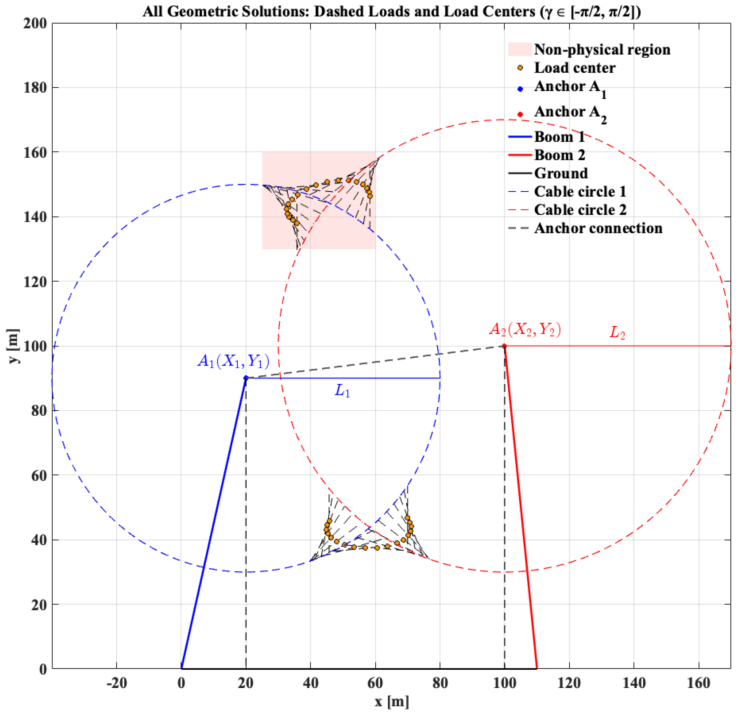

Figure 4.4: Variation in load position and direction with L_1 and L_2 fixed.

positions of the load center (x, y), which collectively form a one–dimensional manifold in the configuration space (x, y, γ). The solid blue and red lines represent the two crane booms, while the black solid line denotes the ground. The vertical dashed lines mark the workspace boundaries of the cranes. A shallow red shaded area is added to highlight the upper region of the manifold, which lies above the line connecting the two anchor points and does not correspond to a physically realizable configuration. This region violates the geometric feasibility constraints of the DCC system and lacks physical meaning, as it corresponds to configurations that cannot exist under realistic cable tension conditions.

The lower branch of the manifold, located below the line joining (X_1, Y_1) and (X_2, Y_2), represents the geometrically feasible portion of the configuration space, corresponding to attainable positions of the load within the cranes' operational workspace. By contrast, the upper branch, indicated by the shaded region, corresponds to an over the line configuration of the load center that would require nonphysical cable orientations. Thus, only the lower branch is considered meaningful for subsequent modeling and control design.

Based on Fig. 4.4 and Table 4.2, it can be observed that under the given DCC configuration and fixed cable lengths L_1 and L_2, the feasible variation of the load position (x, y) corresponding to $\gamma \in [-1.571, 1.561]$ lies within the following intervals:

$$x \in [44.921, 71.121], \quad y \in [37.358, 46.846].$$

Table 4.2: Load center coordinates for varying γ with fixed cable lengths.

γ (rad)	-1.571	-1.396	-1.211	-1.026	-0.842	-0.657	-0.472	-0.287	-0.102
x (m)	69.908	70.717	71.121	71.014	70.295	68.889	66.769	63.992	60.715
y (m)	46.846	45.494	44.116	42.727	41.358	40.059	38.909	38.009	37.467
γ (rad)	0.082	0.267	0.452	0.637	0.822	1.006	1.191	1.376	1.561
x (m)	57.196	53.748	50.672	48.186	46.402	45.333	44.921	45.073	45.681
y (m)	37.358	37.694	38.420	39.429	40.611	41.875	43.164	44.452	45.726

The analysis of this geometric manifold provides a clear visualization of the system's configuration dependency and lays the foundation for subsequent derivations of equilibrium and control strategies.

4.3 Dynamic Analysis: Lagrangian Modeling

Following the kinematic analysis of the rigid-rod load, we proceed to formulate an accurate dynamic model. For notational simplicity, the following abbreviations are introduced

$$S_\theta = \sin\theta,\ C_\theta = \cos\theta,\ \text{where } \theta \in \begin{cases} \alpha_i, \gamma, \alpha_i \pm \gamma, \alpha_i \pm \alpha_j, \\ i, j = 1, 2,\ (i \neq j). \end{cases}$$

Recalling the previously derived system constraints, they can be compactly expressed as follows

$$X_1 - X_2 + L_1 S_{\alpha_1} + L_2 S_{\alpha_2} + 2dC_\gamma = 0, \tag{4.21}$$

$$Y_1 - Y_2 - L_1 C_{\alpha_1} + L_2 C_{\alpha_2} + 2dS_\gamma = 0. \tag{4.22}$$

The system clearly involves five degrees of freedom. Based on the inverse kinematics analysis, the cable angles α_1 and α_2 are equivalent to the load coordinates x and y. Since the constraints Eq. (4.21 – 4.22) explicitly depend on $L_1, L_2, \gamma, \alpha_1$, and α_2, these quantities are chosen as the state variables for the subsequent dynamic modeling. However, the presence of the two constraints indicates that not all five degrees of freedom are independent, with two of them being determined by the remaining three. Since the DCC system lifts the load by controlling the lengths $L_1(t)$ and $L_2(t)$, and $\gamma(t)$ represents the load's attitude, we define $L_1(t), L_2(t), \gamma(t)$ as the independent degrees of freedom, whereas $\alpha_1(t)$ and $\alpha_2(t)$ are treated as dependent ones.

The Lagrange method is used to model the DCC system. To obtain a sixth–order dynamic system involving only the independent variables, we first formulate the full tenth–order dynamic model corresponding to the five degrees of freedom, which still contains the dependent variables, as follows:

$$\frac{d}{dt}\left(\frac{\partial \mathcal{L}}{\partial \dot{q}_\phi}\right) - \frac{\partial \mathcal{L}}{\partial q_\phi} = u_\phi \tag{4.23}$$

where $q_\phi = \left[L_1(t), L_2(t), \gamma(t), \alpha_1(t), \alpha_2(t)\right]^\top$ and $\dot{q}_\phi = \left[\dot{L}_1(t), \dot{L}_2(t), \dot{\gamma}(t), \dot{\alpha}_1(t), \dot{\alpha}_2(t)\right]^\top$ denote the variable vector and generalized velocity respectively, $u_\phi = \left[\tau_1(t), \tau_2(t), 0, 0, 0\right]^\top$ represent the generalized force, where $\tau_1(t), \tau_2(t)$ denote the manipulable control inputs. The Lagrangian is given by:

$$\mathcal{L} = T(t) - V(t) \tag{4.24}$$

To derive the Lagrangian dynamic model of the system, we first define its kinetic and potential energy. Since the boom angle remains fixed during operation, the system's energy depends on the load center coordinates (x, y), where

$$V(t) = mgy \tag{4.25}$$

Since the load undergoes both translational and rotational motion, its kinetic energy comprises both translational and rotational components

$$T(t) = \frac{1}{2}m\left(\dot{x}^2 + \dot{y}^2\right) + \frac{1}{2}I\dot{\gamma}^2 \tag{4.26}$$

Its rotational motion can be approximated as that of a uniform straight rod rotating about an axis passing through its center and perpendicular to its length. $I = (md^2)/3$ represents the moment of inertia of the load.

Differentiating the load's midpoint coordinates derived from Eq. (4.18) yields:

$$\begin{cases} \dot{x} = \frac{1}{2}(\dot{L}_1 S_{\alpha_1} + L_1\dot{\alpha}_1 C_{\alpha_1} - \dot{L}_2 S_{\alpha_2} - L_2\dot{\alpha}_2 C_{\alpha_2}) \\ \dot{y} = \frac{1}{2}(L_1\dot{\alpha}_1 S_{\alpha_1} - \dot{L}_1 C_{\alpha_1} + L_2\dot{\alpha}_2 S_{\alpha_2} - \dot{L}_2 C_{\alpha_2}) \end{cases} \tag{4.27}$$

Substituting Eq. (4.27) into Eq. (4.26) one obtains

$$\begin{aligned} T(t) =& \frac{1}{8}m(\dot{L}_1^2 + L_1^2\dot{\alpha}_1^2 + L_2^2\dot{\alpha}_2^2 + 2\dot{L}_1\dot{L}_2 C_{(\alpha_1+\alpha_2)} \\ & - 2\dot{L}_1 L_2\dot{\alpha}_2 S_{(\alpha_1+\alpha_2)} - 2L_1\dot{L}_2\dot{\alpha}_1 S_{(\alpha_1+\alpha_2)} \\ & - 2L_1 L_2\dot{\alpha}_1\dot{\alpha}_2 C_{(\alpha_1+\alpha_2)} + \dot{L}_2^2) + \frac{1}{6}md^2\dot{\gamma}^2 \end{aligned} \tag{4.28}$$

Similarly, substituting Eq. (4.18) into Eq. (4.25) one obtains

$$V(t) = \frac{1}{2}mg(Y_1 + Y_2 - L_1 C_{\alpha_1} - L_2 C_{\alpha_2}) \tag{4.29}$$

Since the potential energy of the system $V(t)$ does not contain the $\dot{q}_\phi$ term, Eq. (4.23) can be rewritten as

$$\frac{d}{dt}\left(\frac{\partial T}{\partial \dot{q}_\phi}\right) - \frac{\partial T}{\partial q_\phi} + \frac{\partial V}{\partial q_\phi} = u_\phi \tag{4.30}$$

Then, the dynamic equations of the system can be defined as the following forms

$$\begin{cases} \mathcal{F}_{L_i} \overset{\text{def}}{=} \frac{d}{dt}\left(\frac{\partial T}{\partial \dot{L}_i}\right) - \frac{\partial T}{\partial L_i} + \frac{\partial V}{\partial L_i} = \tau_i(t),\ i = 1, 2 \\ \mathcal{F}_{\gamma} \overset{\text{def}}{=} \frac{d}{dt}\left(\frac{\partial T}{\partial \dot{\gamma}}\right) - \frac{\partial T}{\partial \gamma} + \frac{\partial V}{\partial \gamma} = 0, \\ \mathcal{F}_{\alpha_i} \overset{\text{def}}{=} \frac{d}{dt}\left(\frac{\partial T}{\partial \dot{\alpha}_i}\right) - \frac{\partial T}{\partial \alpha_i} + \frac{\partial V}{\partial \alpha_i} = 0. \end{cases} \tag{4.31}$$

where the expression are expressed as follows

$$\begin{aligned} \mathcal{F}_{L_1} =& \frac{1}{4} m\big(\ddot{L}_1 - L_1\dot{\alpha}_1^2 - (2\dot{L}_2\dot{\alpha}_2 + L_2\ddot{\alpha}_2)S_{(\alpha_1+\alpha_2)} \\ &+ (\ddot{L}_2 - L_2\dot{\alpha}_2^2)C_{(\alpha_1+\alpha_2)} - 2gC_{\alpha_1}\big), \\ \mathcal{F}_{L_2} =& \frac{1}{4} m\big(\ddot{L}_2 - L_2\dot{\alpha}_2^2 - (2\dot{L}_1\dot{\alpha}_1 + L_1\ddot{\alpha}_1)S_{(\alpha_1+\alpha_2)} \\ &+ (\ddot{L}_1 - L_1\dot{\alpha}_1^2)C_{(\alpha_1+\alpha_2)} - 2gC_{\alpha_2}\big), \\ \mathcal{F}_{\gamma} =& \frac{1}{3} m d^2 \ddot{\gamma}, \\ \mathcal{F}_{\alpha_1} =& \frac{1}{4} m\big(2L_1\dot{L}_1\dot{\alpha}_1 + L_1^2\ddot{\alpha}_1 + 2gL_1S_{\alpha_1} \\ &- (2L_1\dot{L}_2\dot{\alpha}_2 + L_1L_2\ddot{\alpha}_2)C_{(\alpha_1+\alpha_2)} \\ &+ (L_1L_2\dot{\alpha}_2^2 - L_1\ddot{L}_2)S_{(\alpha_1+\alpha_2)}\big), \\ \mathcal{F}_{\alpha_2} =& \frac{1}{4} m\big(2L_2\dot{L}_2\dot{\alpha}_2 + L_2^2\ddot{\alpha}_2 + 2gL_2S_{\alpha_2} \\ &- (2\dot{L}_1L_2\dot{\alpha}_1 + L_1L_2\ddot{\alpha}_1)C_{(\alpha_1+\alpha_2)} \\ &+ (L_1L_2\dot{\alpha}_1^2 - \ddot{L}_1L_2)S_{(\alpha_1+\alpha_2)}\big). \end{aligned} \tag{4.32}$$

To simplify the description and facilitate the subsequent analysis, we derive the matrix form of the dynamic equation with five generalized coordinates $L_1, L_2, \gamma, \alpha_1, \alpha_2$—based on Eq. (4.32). Meanwhile, the effect of friction should also be taken into account. Therefore, the form of the dynamic model can be expressed in the following compact matrix–vector form:

$$M'(q_\phi)\ddot{q}_\phi + C'(q_\phi, \dot{q}_\phi)\dot{q}_\phi + G'(q_\phi) = u_\phi - F'\dot{q}_\phi \tag{4.33}$$

where $M'(q_\phi), C'(q_\phi, \dot{q}_\phi) \in \mathbb{R}^{5\times5}$, $G'(q_\phi) \in \mathbb{R}^5$ are the inertia matrix, centripetal Coriolis matrix and gravity vector respectively. $F' \in \mathbb{R}^{5\times5}$ is a matrix containing the friction coefficients.

After arrangement, the matrices in Eq. (4.33) are expressed as follows

$$M'(q_\phi) = \begin{bmatrix} \frac{1}{4}m & M'_{12} & 0 & 0 & M'_{15} \\ M'_{12} & \frac{1}{4}m & 0 & M'_{24} & 0 \\ 0 & 0 & \frac{1}{3}md^2 & 0 & 0 \\ 0 & M'_{24} & 0 & \frac{1}{4}mL_1^2 & M'_{45} \\ M'_{15} & 0 & 0 & M'_{45} & \frac{1}{4}mL_2^2 \end{bmatrix}, \quad F' = \begin{bmatrix} \mathrm{diag}(F_{f1}, F_{f2}, F_{f3}) & \mathbf{0}_{3\times 2} \\ \mathbf{0}_{2\times 3} & \mathbf{0}_{2\times 2} \end{bmatrix},$$

$$C'(q_\phi, \dot{q}_\phi) = \begin{bmatrix} 0 & C'_{12} & 0 & C'_{14} & C'_{15} \\ C'_{21} & 0 & 0 & C'_{24} & C'_{25} \\ 0 & 0 & 0 & 0 & 0 \\ C'_{41} & C'_{42} & 0 & 0 & C'_{45} \\ C'_{51} & C'_{52} & 0 & C'_{54} & 0 \end{bmatrix}, \quad G'(q_\phi) = \begin{bmatrix} -\frac{1}{2}mgC_{\alpha_1} \\ -\frac{1}{2}mgC_{\alpha_2} \\ 0 \\ \frac{1}{2}mgL_1S_{\alpha_1} \\ \frac{1}{2}mgL_2S_{\alpha_2} \end{bmatrix}. \tag{4.34}$$

where the detailed expressions of the elements of $M'(q_\phi)$ and $C'(q_\phi, \dot{q}_\phi)$ are provided as follows

$$M'_{12} = \frac{m}{4}C_{(\alpha_1+\alpha_2)}, \qquad M'_{15} = -\frac{m}{4}L_2S_{(\alpha_1+\alpha_2)},$$

$$M'_{24} = -\frac{m}{4}L_1S_{(\alpha_1+\alpha_2)}, \qquad M'_{45} = -\frac{m}{4}L_1L_2C_{(\alpha_1+\alpha_2)},$$

$$C'_{12} = -\frac{m}{2}\dot{\alpha}_2S_{(\alpha_1+\alpha_2)}, \qquad C'_{14} = -\frac{m}{4}L_1\dot{\alpha}_1,$$

$$C'_{15} = -\frac{m}{4}L_2\dot{\alpha}_2C_{(\alpha_1+\alpha_2)}, \qquad C'_{21} = -\frac{m}{2}\dot{\alpha}_1S_{(\alpha_1+\alpha_2)},$$

$$C'_{24} = -\frac{m}{4}L_1\dot{\alpha}_1C_{(\alpha_1+\alpha_2)}, \qquad C'_{25} = -\frac{m}{4}L_2\dot{\alpha}_2,$$

$$C'_{41} = \frac{m}{2}L_1\dot{\alpha}_1, \qquad C'_{42} = -\frac{m}{2}L_1\dot{\alpha}_2C_{(\alpha_1+\alpha_2)},$$

$$C'_{45} = \frac{m}{4}L_1L_2\dot{\alpha}_2S_{(\alpha_1+\alpha_2)}, \qquad C'_{52} = \frac{m}{2}L_2\dot{\alpha}_2,$$

$$C'_{51} = -\frac{m}{2}L_2\dot{\alpha}_1C_{(\alpha_1+\alpha_2)}, \qquad C'_{54} = \frac{m}{4}L_1L_2\dot{\alpha}_1S_{(\alpha_1+\alpha_2)}.$$

4.4 Order Reduction

At this stage, the Lagrangian dynamic model of the DCC system with a rigid–rod load has been fully established. The complete formulation contains ten state variables, corresponding to five generalized coordinates and their time derivatives. However, although the model is expressed using five variables, the system inherently possesses only three independent degrees of freedom. The two angular coordinates, α_1 and α_2, are not independent; they are fully constrained by the geometry of the cable–load configuration.

For this reason, the dependent variables α_1 and α_2, together with their time derivatives, must be eliminated from the model. Removing these variables reduces the number of independent degrees of freedom from five to three and lowers the state dimension of the dynamical model from ten to six. This reduction significantly simplifies the structure of the model and facilitates the subsequent controller design.

The reduction is carried out by incorporating the constraint relations in Eq. (4.5 - 4.6) into the dynamics. In particular, Eq. (4.14 - 4.15) provides explicit expressions for $\alpha_1(t)$ and $\alpha_2(t)$ as functions of the independent variables $L_1(t)$, $L_2(t)$, and $\gamma(t)$. Substituting these expressions into the Lagrangian equations yields a consistent sixth–order dynamic model with three degrees of freedom.

Although an explicit representation of functions $h_1(L_1, L_2, \gamma)$ and $h_2(L_1, L_2, \gamma)$ appears to be not possible to derive by Eq. (4.5 - 4.6), some useful manipulations are presented next. Taking the temporal derivative of Eq. (4.14) and Eq. (4.15) one obtains

$$\begin{aligned} \dot{\alpha}_1 &= \frac{\partial h_1}{\partial L_1}\dot{L}_1 + \frac{\partial h_1}{\partial L_2}\dot{L}_2 + \frac{\partial h_1}{\partial \gamma}\dot{\gamma}, \\ \dot{\alpha}_2 &= \frac{\partial h_2}{\partial L_1}\dot{L}_1 + \frac{\partial h_2}{\partial L_2}\dot{L}_2 + \frac{\partial h_2}{\partial \gamma}\dot{\gamma}. \end{aligned} \tag{4.35}$$

Eq. (4.35) can be rewritten in the more compact form as follows:

$$\begin{aligned} \dot{\alpha_1} &= h^1_{L_1}\dot{L}_1 + h^1_{L_2}\dot{L}_2 + h^1_{\gamma}\dot{\gamma}, \\ \dot{\alpha_2} &= h^2_{L_1}\dot{L}_1 + h^2_{L_2}\dot{L}_2 + h^2_{\gamma}\dot{\gamma}. \end{aligned} \tag{4.36}$$

where

$$\begin{aligned} h^1_{L_1} &\overset{\text{def}}{=} \frac{\partial h_1}{\partial L_1}, \quad h^1_{L_2} \overset{\text{def}}{=} \frac{\partial h_1}{\partial L_2}, \quad h^1_{\gamma} \overset{\text{def}}{=} \frac{\partial h_1}{\partial \gamma}, \\ h^2_{L_1} &\overset{\text{def}}{=} \frac{\partial h_2}{\partial L_1}, \quad h^2_{L_2} \overset{\text{def}}{=} \frac{\partial h_2}{\partial L_2}, \quad h^2_{\gamma} \overset{\text{def}}{=} \frac{\partial h_2}{\partial \gamma}. \end{aligned} \tag{4.37}$$

To derive the expressions for the functions $h^1_{L_1}$, $h^1_{L_2}$, ... ,h^2_{γ} in Eq. (4.37), take the partial

derivative of constraints Eq. (4.5) and Eq. (4.6) with respect to L_1, yielding:

$$\begin{aligned} S_{\alpha_1} + L_1 h^1_{L_1} C_{\alpha_1} + L_2 h^2_{L_1} C_{\alpha_2} = 0, \\ L_1 h^1_{L_1} S_{\alpha_1} - C_{\alpha_1} - L_2 h^2_{L_1} S_{\alpha_2} = 0. \end{aligned} \tag{4.38}$$

The expressions for $h^1_{L_1}$ and $h^2_{L_1}$ can then be computed as follows

$$h^1_{L_1} = \frac{C_{(\alpha_1+\alpha_2)}}{L_1 S_{(\alpha_1+\alpha_2)}} = \frac{C_{(h_1+h_2)}}{L_1 S_{(h_1+h_2)}}, \quad h^2_{L_1} = -\frac{1}{L_2 S_{(\alpha_1+\alpha_2)}} = -\frac{1}{L_2 S_{(h_1+h_2)}}. \tag{4.39}$$

Similarly, take the partial derivative of constraints Eq. (4.5) and Eq. (4.6) with respect to L_2 and γ. Straightforward manipulations yield

$$\begin{aligned} h^1_{L_2} &= -\frac{1}{L_1 S_{(\alpha_1+\alpha_2)}} = -\frac{1}{L_1 S_{(h_1+h_2)}}, \qquad h^2_{L_2} = \frac{C_{(\alpha_1+\alpha_2)}}{L_2 S_{(\alpha_1+\alpha_2)}} = \frac{C_{(h_1+h_2)}}{L_2 S_{(h_1+h_2)}} \\ h^1_{\gamma} &= -\frac{2dC_{(\alpha_2+\gamma)}}{L_1 S_{(\alpha_1+\alpha_2)}} = -\frac{2dC_{(h_2+\gamma)}}{L_1 S_{(h_1+h_2)}}, \qquad h^2_{\gamma} = \frac{2dC_{(\alpha_1-\gamma)}}{L_2 S_{(\alpha_1+\alpha_2)}} = \frac{2dC_{(h_1-\gamma)}}{L_2 S_{(h_1+h_2)}}. \end{aligned} \tag{4.40}$$

It should be emphasized that the coefficients obtained by differentiating α_1 and α_2 with respect to time denoted as $h^1_{L_1}$, $h^1_{L_2}$, ... ,h^2_{γ} still depend on the five system variables. At this stage, we derive the dynamic equations for the three variables system using the Lagrange equation Eq. (4.80)

$$\frac{d}{dt}\left(\frac{\partial T}{\partial \dot{q}}\right) - \frac{\partial T}{\partial q} + \frac{\partial V}{\partial q} = u \tag{4.41}$$

where $q = \left[L_1(t), L_2(t), \gamma(t)\right]^\top$ represent the vector of generalized Lagrangian coordinates, and $u = \left[\tau_1(t), \tau_2(t), 0\right]^\top$ denotes the generalized force vector. After arrangement, the three variables dynamic model can be defined in the following form

$$\begin{cases} \mathcal{F}_{L_1} + h^1_{L_1}\mathcal{F}_{\alpha_1} + h^2_{L_1}\mathcal{F}_{\alpha_2} = \tau_1(t) \\ \mathcal{F}_{L_2} + h^1_{L_2}\mathcal{F}_{\alpha_1} + h^2_{L_2}\mathcal{F}_{\alpha_2} = \tau_2(t) \\ \mathcal{F}_{\gamma} + h^1_{\gamma}\mathcal{F}_{\alpha_1} + h^2_{\gamma}\mathcal{F}_{\alpha_2} = 0 \end{cases} \tag{4.42}$$

Similarly, Eq. (4.33) can be rewritten in the following form:

$$M(q_\phi)\ddot{q} + C(q_\phi, \dot{q}_\phi)\dot{q} + G(q_\phi) = u - F\dot{q} \tag{4.43}$$

where $M(q_\phi), C(q_\phi, \dot{q}_\phi) \in \mathbb{R}^{3\times3}$, $G(q) \in \mathbb{R}^3$ are the inertia matrix, centripetal Coriolis matrix and gravity vector respectively. According to Eq. (4.36), we can obtain the relationship between $\dot{q}$ and $\dot{q}_\phi$ as follows

$$\dot{q}_\phi = N(q_\phi)\dot{q}, \quad u = N(q_\phi)^\top u_\phi. \tag{4.44}$$

where

$$N(q_\phi)^\top = \begin{bmatrix} 1 & 0 & 0 & h^1_{L_1} & h^2_{L_1} \\ 0 & 1 & 0 & h^1_{L_2} & h^2_{L_2} \\ 0 & 0 & 1 & h^1_{\gamma} & h^2_{\gamma} \end{bmatrix} \tag{4.45}$$

Differentiating both sides of $\dot{q_\phi}$ yields:

$$\ddot{q}_\phi = \dot{N}(q_\phi)\dot{q} + N(q_\phi)\ddot{q} \tag{4.46}$$

For brevity, the following simplified notation will be used to present the mathematical model

$$M'(q_\phi) = M',\ C'(q_\phi, \dot{q}_\phi) = C',\ G'(q_\phi) = G',\ N(q_\phi) = N, \tag{4.47}$$

$$M(q_\phi) = M,\ C(q_\phi, \dot{q}_\phi) = C,\ G(q_\phi) = G. \tag{4.48}$$

substituting Eq. (4.44) and Eq. (4.46) into Eq. (4.33) one obtains

$$M'(\dot{N}\dot{q} + N\ddot{q}) + C'(N\dot{q}) + G' = u_\phi - F'\dot{q}_\phi. \tag{4.49}$$

multiply Eq. (4.49) by the matrix $N^\top$ on the left-hand side

$$N^\top M'(\dot{N}\dot{q} + N\ddot{q}) + N^\top C'(N\dot{q}) + N^\top G' = N^\top u_\phi - N^\top F'\dot{q}_\phi. \tag{4.50}$$

After simplification, the expression can be written as follows

$$(N^\top M'N)\ddot{q} + N^\top(M'\dot{N} + C'N)\dot{q} + N^\top G' = N^\top u_\phi - N^\top F'\dot{q}_\phi \tag{4.51}$$

defining

$$\begin{aligned} M = N^\top M'N, \quad G = N^\top G', \quad u = N^\top u_\phi, \\ C = N^\top M'\dot{N} + N^\top C'N, \quad F\dot{q} = N^\top F'\dot{q}_\phi \end{aligned} \tag{4.52}$$

the final form of the dynamic model can be expressed as follows

$$M\ddot{q} + C\dot{q} + G = u - F\dot{q} \tag{4.53}$$

Through subsequent computations and arrangements,$M(q_\phi), C(q_\phi, \dot{q_\phi})$ and $G(q_\phi)$ is derived as

follows

$$M = \begin{bmatrix} M_{11} & M_{12} & M_{13} \\ M_{21} & M_{22} & M_{23} \\ M_{31} & M_{32} & M_{33} \end{bmatrix}, \quad C = \begin{bmatrix} C_{11} & C_{12} & C_{13} \\ C_{21} & C_{22} & C_{23} \\ C_{31} & C_{32} & C_{33} \end{bmatrix},$$

$$G = \begin{bmatrix} \frac{1}{2}h^1_{L_1} mgL_1 S_{\alpha_1} + \frac{1}{2}h^2_{L_1} mgL_2 S_{\alpha_2} - \frac{1}{2}mgC_{\alpha_1} \\ \frac{1}{2}h^1_{L_2} mgL_1 S_{\alpha_1} + \frac{1}{2}h^2_{L_2} mgL_2 S_{\alpha_2} - \frac{1}{2}mgC_{\alpha_2} \\ \frac{1}{2}h^1_{\gamma} mgL_1 S_{\alpha_1} + \frac{1}{2}h^2_{\gamma} mgL_2 S_{\alpha_2} \end{bmatrix}, \quad F = \mathrm{diag}(F_{f1}, F_{f2}, F_{f3}). \tag{4.54}$$

and the detailed expressions of the elements of matrices M and C are provided as follows

$$M_{11} = \frac{m}{4}\Big(L_1^2 \left(h^1_{L_1}\right)^2 + L_2^2 \left(h^2_{L_1}\right)^2 - 2L_1L_2h^1_{L_1}h^2_{L_1}C_{(\alpha_1+\alpha_2)} - 2L_2h^2_{L_1}S_{(\alpha_1+\alpha_2)} + 1\Big),$$

$$M_{12} = M_{21} = \frac{m}{4}\Big(h^1_{L_1}h^1_{L_2}L_1^2 + h^2_{L_1}h^2_{L_2}L_2^2 + (1 - h^1_{L_1}h^2_{L_2} - h^1_{L_2}h^2_{L_1})L_1L_2C_{(\alpha_1+\alpha_2)}$$

$$- (h^1_{L_1}L_1 + h^2_{L_2}L_2)S_{(\alpha_1+\alpha_2)}\Big),$$

$$M_{13} = M_{31} = \frac{m}{4}\Big(h^1_{L_1}h^1_{\gamma}L_1^2 + h^2_{L_1}h^2_{\gamma}L_2^2 - (h^1_{L_1}h^2_{\gamma} + h^1_{\gamma}h^2_{L_1})L_1L_2C_{(\alpha_1+\alpha_2)} - h^2_{\gamma}L_2S_{(\alpha_1+\alpha_2)}\Big),$$

$$M_{22} = \frac{m}{4}\Big(L_1^2 \left(h^1_{L_2}\right)^2 + L_2^2 \left(h^2_{L_2}\right)^2 - 2L_1L_2h^1_{L_2}h^2_{L_2}C_{(\alpha_1+\alpha_2)} - 2L_1h^1_{L_2}S_{(\alpha_1+\alpha_2)} + 1\Big),$$

$$M_{23} = M_{32} = \frac{m}{4}\Big(h^1_{L_2}h^1_{\gamma}L_1^2 + h^2_{L_2}h^2_{\gamma}L_2^2 - (h^1_{L_2}h^2_{\gamma} + h^1_{\gamma}h^2_{L_2})L_1L_2C_{(\alpha_1+\alpha_2)} - h^1_{\gamma}L_1S_{(\alpha_1+\alpha_2)}\Big),$$

$$M_{33} = \frac{m}{12}\Big(3L_1^2 \left(h^1_{\gamma}\right)^2 + 3L_2^2 \left(h^2_{\gamma}\right)^2 + 4d^2 - 6L_1L_2h^1_{\gamma}h^2_{\gamma}C_{(\alpha_1+\alpha_2)}\Big).$$

$$C_{11} = \frac{m}{4}(\dot{\alpha}_1 L_1 h^1_{L_1} - (2\dot{\alpha}_1 + \dot{\alpha}_2)L_2 h^2_{L_1} C_{(\alpha_1+\alpha_2)} + (L_1\dot{\alpha}_1 + \dot{\alpha}_2)L_2 h^1_{L_1} h^2_{L_1} S_{(\alpha_1+\alpha_2)}),$$

$$C_{12} = \frac{m}{4}(2L_2 h^2_{L_1}\dot{\alpha}_2 - (L_1 h^1_{L_1} + L_2 h^2_{L_2})C_{(\alpha_1+\alpha_2)}\dot{\alpha}_2 + (L_1 L_2 h^1_{L_1} h^2_{L_2}\dot{\alpha}_2$$

$$+ L_1 L_2 h^1_{L_2} h^2_{L_1}\dot{\alpha}_1 - 2)S_{(\alpha_1+\alpha_2)} - L_1 h^1_{L_1}\dot{\alpha}_1),$$

$$C_{13} = \frac{m}{4}(L_1 L_2 S_{(\alpha_1+\alpha_2)}(h^1_{L_1} h^2_{\gamma}\dot{\alpha}_2 + h^1_{\gamma} h^2_{L_1}\dot{\alpha}_1) - L_2 h^2_{\gamma} C_{(\alpha_1+\alpha_2)}\dot{\alpha}_2 - L_1 h^1_{\gamma}\dot{\alpha}_1),$$

$$C_{21} = \frac{m}{4}(2L_1 h^1_{L_2}\dot{\alpha}_1 - (L_1 h^1_{L_1} + 2L_2 h^2_{L_2})C_{(\alpha_1+\alpha_2)}\dot{\alpha}_1 + L_1 L_2 S_{(\alpha_1+\alpha_2)}(h^1_{L_1} h^2_{L_2}\dot{\alpha}_1 + h^1_{L_2} h^2_{L_1}\dot{\alpha}_2)$$

$$- 2S_{(\alpha_1+\alpha_2)}\dot{\alpha}_1 - L_2 h^2_{L_1}\dot{\alpha}_2),$$

$$C_{22} = \frac{m}{4}(L_2 h^2_{L_2}\dot{\alpha}_2 - L_1 h^1_{L_2} C_{(\alpha_1+\alpha_2)}(\dot{\alpha}_1 + 2\dot{\alpha}_2) + L_1 L_2 h^1_{L_2} k_{L_2} S_{(\alpha_1+\alpha_2)}(\dot{\alpha}_1 + \dot{\alpha}_2)),$$

$$C_{23} = \frac{m}{4}((h^1_{L_2} h^2_{\gamma}\dot{\alpha}_2 + h^1_{\gamma} h^2_{L_2}\dot{\alpha}_1)L_1 L_2 S_{(\alpha_1+\alpha_2)} - L_1 h^1_{\gamma} C_{(\alpha_1+\alpha_2)}\dot{\alpha}_1 - L_2 h^2_{\gamma}\dot{\alpha}_2),$$

$$C_{31} = \frac{m}{4}((h^1_{L_1} h^2_{\gamma}\dot{\alpha}_1 + h^1_{\gamma} h^2_{L_1}\dot{\alpha}_2)L_1 L_2 S_{(\alpha_1+\alpha_2)} + 2L_1 h^1_{\gamma}\dot{\alpha}_1 - 2L_2 h^2_{\gamma}\dot{\alpha}_1 C_{(\alpha_1+\alpha_2)}),$$

$$C_{32} = \frac{m}{4}((h^1_{L_2} h^2_{\gamma}\dot{\alpha}_1 + h^1_{\gamma} h^2_{L_2}\dot{\alpha}_2)L_1 L_2 S_{(\alpha_1+\alpha_2)} + 2L_2 h^2_{\gamma}\dot{\alpha}_2 - 2L_1 h^1_{\gamma}\dot{\alpha}_2 C_{(\alpha_1+\alpha_2)}),$$

$$C_{33} = \frac{m}{4}(\dot{\alpha}_1 + \dot{\alpha}_2)L_1 L_2 h^1_{\gamma} h^2_{\gamma} S_{(\alpha_1+\alpha_2)}.$$

Although matrix M, C and G in Eq. (4.54) depend on the elements of vector q_ϕ, once the relations $\alpha_1 = h_1(L_1, L_2, \gamma), \alpha_2 = h_2(L_1, L_2, \gamma)$ are replaced into it, then matrix M, C and G depend on q only. This substitution formally eliminates the dependent variables and yields the reduced three degree of freedom dynamic model described by Eq. (4.53).

However, for numerical implementation, the computation of α_1 and α_2 remains necessary at each integration step, since they still affect the evaluation of the system matrices $M(q)$, $C(q, \dot{q})$, and $G(q)$. To ensure consistency between the reduced order coordinates and the original geometric constraints, a stepwise numerical procedure is adopted as follows.

After the order reduction, the state vector of the reduced system comprises only the independent generalized coordinates $q = [L_1,\ L_2,\ \gamma]^\top$, while the dependent variables α_1 and α_2 are implicitly related to q through the geometric constraint Eq. (4.21 – 4.22). However, since the matrices $M(q)$, $C(q, \dot{q})$, and $G(q)$ in Eq. (4.54) are functions of both the independent and dependent variables, their evaluation during time integration requires the consistent computation of α_1 and α_2 at each time step.

To handle this dependency, a stepwise numerical procedure is adopted. At each discrete time instant t_k ($k = 0, 1, \ldots, N$), the current state $q_k = q(t_k) = [L_{1k}, L_{2k}, \gamma_k]^\top$ is used to determine the corresponding values of α_{1k} and α_{2k} by numerically solving the nonlinear constraint Eq. (4.21 – 4.22). The obtained values are then substituted into the system dynamics Eq. (4.53) to compute the state derivatives and advance the integration to the next step. This iterative process ensures consistency between the reduced order coordinates and the original geometric constraints throughout the simulation.

The overall procedure is summarized in Algorithm 4.

Algorithm 4: Stepwise Numerical Computation of α_1 and α_2

Input: Initial state variables $L_1(0)$, $L_2(0)$, $\gamma(0)$, total steps N, final time t_f

Output: Sequences $\{\alpha_{1k}, \alpha_{2k}, q_k, \dot{q}_k\}$ for $k = 0, 1, \ldots, N$

Set $t_0 = 0$, $t_N = t_f$, and choose time step $\Delta t = t_f/N$;

Initialize $q_0 = [L_{10}, L_{20}, \gamma_0]^\top$;

for $k = 0, 1, 2, \ldots, N-1$ **do**

(1) Solve the constraint Eq. (4.21 – 4.22) numerically to obtain α_{1k} and α_{2k} corresponding to q_k;

(2) Evaluate the matrices $M(q_k)$, $C(q_k, \dot{q}_k)$, and $G(q_k)$ using α_{1k} and α_{2k};

(3) Solving the system dynamics Eq. (4.53) over Δt to compute q_{k+1} and $\dot{q}_{k+1}$;

This numerical scheme allows the reduced order model to be integrated efficiently while preserving the consistency with the full system geometry. In addition, it avoids explicit analytical substitution of the dependent variables, thus maintaining numerical stability even for configurations close to kinematic singularities.

In this section, the original tenth–order dynamical model, whose state vector is

$$(q_\phi, \dot{q}_\phi) = \left[L_1,\ L_2,\ \gamma,\ \alpha_1,\ \alpha_2,\ \dot{L}_1,\ \dot{L}_2,\ \dot{\gamma},\ \dot{\alpha}_1,\ \dot{\alpha}_2\right]^\top,$$

is reduced to a sixth–order model,

$$(q, \dot{q}) = \left[L_1,\ L_2,\ \gamma,\ \dot{L}_1,\ \dot{L}_2,\ \dot{\gamma}\right]^\top,$$

by explicitly enforcing the constraints of the DCC system. These constraints eliminate the two angular variables and their derivatives, thereby reducing the number of independent degrees of freedom from five to three. As a direct consequence, the order of the dynamical model decreases from ten to six. This reduction not only simplifies the subsequent controller design but also provides a systematic and principled methodology for modeling complex cooperative hoisting systems subject to kinematic and geometric constraints.

4.5 Computing the Equilibrium State of the System

Having established an accurate dynamic model for the dual crane system with a rigid rod load, it is essential to determine the equilibrium configuration of the system before proceeding to the design of the lifting control strategy. The equilibrium analysis provides the reference configuration around which the control laws can be developed and the dynamic behavior of the suspended load can be stabilized.

In heavy load hoisting operations, the weight of the lifting components such as cables, hooks, and spreader bars is negligible compared with the weight of the payload itself. Neglecting these relatively light components introduces no significant error in the overall system balance. At equilibrium, all structural elements of the system, including the payload's center of mass, the cable anchor points, and the boom attachment points, must lie within the same vertical plane. Otherwise, gravitational forces would induce lateral motion or oscillations, preventing the system from maintaining a static configuration.

Therefore, the equilibrium configuration of the system can be analyzed within a two dimensional plane, which is consistent with Assumptions 3.1. This planar representation significantly simplifies the equilibrium computation while still capturing the essential characteristics of the dual crane hoisting mechanism.

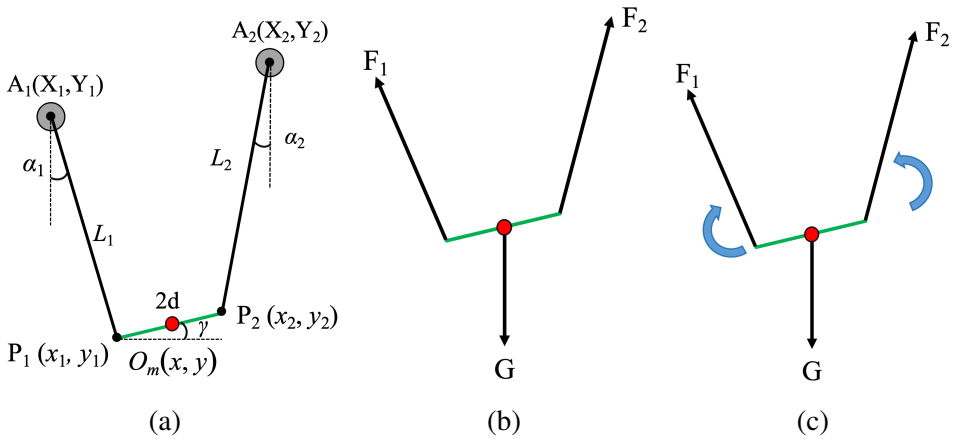

Figure 4.5: Kinematics, forces, and moments of the system in dual crane lifting

The rigid rod load system can be regarded as a closed kinematic chain composed of three links: two hoisting cables and the rigid load itself. As illustrated in Fig. 4.5a, four revolute joints connect these links, namely the cable anchor points A_1 and A_2, and the load endpoints P_1 and P_2. The mass center of the load, denoted as O_m, coincides with the midpoint of the rigid rod and is introduced to represent the combined effects of gravity and the cable tensions, as shown in Fig. 4.5b, and Fig. 4.5c illustrates the two distinct torques generated by the rope tension on the load.

In the system, one set of parameters is constant and can be determined at any given simulation instant. These parameters include the cable lengths L_1 and L_2. Another set consists of five unknown variables to be solved, α_1, α_2, γ, F_1, and F_2, which represent, respectively, the cable angles with respect to the vertical axis, the load inclination angle, and the two cable tensions.

The equilibrium configuration of the system is determined by three fundamental conditions: (1) geometric and kinematic constraints, (2) force equilibrium, and (3) torque equilibrium. The geometric constraints arise from the closure of the kinematic loop, which has already been expressed in the kinematic analysis of Section 4.2 as Eq. (4.5 – 4.6). It indicates that the two endpoints of the rigid rod load must be connected to the ends of the cable. The remaining two conditions require that both the resultant force and the resultant moment acting on the mass center O_m vanish in the equilibrium state.

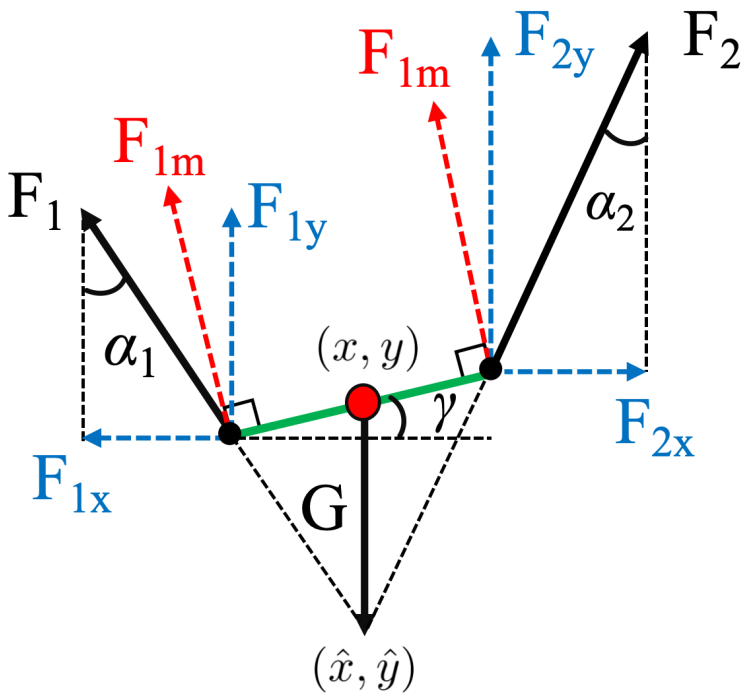

Figure 4.6: Force and moment analysis at static equilibrium

In what follows, we consider forces and torques by their magnitudes, the directions are represented geometrically via the cable orientation angles α_1, α_2 and the load attitude γ. A rigid body is at *static equilibrium* if and only if both the total force and the total moment vanish for any reference point O, i.e.,

$$\sum \mathbf{F} = \mathbf{0}, \qquad \sum \mathbf{M}_O = \mathbf{0}.$$

Figure 4.6 depicts a force diagram: the directions of the cable tensions coincide with the cable

directions, and the gravity acts vertically at the load center. In the present planar setting, exactly three non-parallel forces act on the load (two cable tensions and gravity). By the *classical three-force equilibrium theorem*, equilibrium holds if and only if the lines of action of the three forces are concurrent (they intersect at a single point).

Let the horizontal/vertical components of the tensions be (F_{1x}, F_{1y}) and (F_{2x}, F_{2y}), and let $G = mg$ denote the weight. Force equilibrium reads

$$\begin{cases} F_{1x} - F_{2x} = 0 \\ F_{1y} + F_{2y} - G = 0 \end{cases} \tag{4.55}$$

with the component relations

$$\begin{cases} F_{1x} = F_1 \sin\alpha_1, \quad F_{1y} = F_1 \cos\alpha_1 \\ F_{2x} = F_2 \sin\alpha_2, \quad F_{2y} = F_2 \cos\alpha_2 \\ G = mg \end{cases} \tag{4.56}$$

Substituting Eq. (4.56) into Eq. (4.55) yields

$$\begin{cases} F_1 \sin\alpha_1 - F_2 \sin\alpha_2 = 0 \\ F_1 \cos\alpha_1 + F_2 \cos\alpha_2 - mg = 0 \end{cases} \tag{4.57}$$

As illustrated in Fig. 4.6, the torque-effective components of the cable tensions (perpendicular to the load) are F_{m1} and F_{m2}, so moment equilibrium gives

$$F_{m1} d - F_{m2} d = 0 \tag{4.58}$$

where

$$\begin{cases} F_{m1} = F_1 \cos(\alpha_1 - \gamma) \\ F_{m2} = F_2 \cos(\alpha_2 + \gamma) \end{cases} \tag{4.59}$$

Substituting Eq. (4.59) into Eq. (4.58) yields

$$F_1 \cos(\alpha_1 - \gamma) - F_2 \cos(\alpha_2 + \gamma) = 0 \tag{4.60}$$

Geometric condition for static equilibrium. In the previous derivations, only the magnitudes of the forces were considered to simplify the formulation, and their directions were represented by the geometric angles α_1, α_2, and γ. At this stage, it is convenient to introduce a compact vector notation to describe the resultant of the two cable tensions in a clearer and more concise way. Each cable tension is characterized by its magnitude and direction: the magnitudes are denoted by F_1 and F_2, and the directions are defined by the angles α_1 and α_2, respectively. Accordingly, the two tension forces can be represented in vector form as

$$\mathbf{F}_1 = F_1 \, \mathbf{u}_1, \qquad \mathbf{F}_2 = F_2 \, \mathbf{u}_2, \tag{4.61}$$

where $\mathbf{u}_1$ and $\mathbf{u}_2$ are unit vectors along the directions of the cables. The resultant of these two tensions is therefore written as

$$\mathbf{R} = \mathbf{F}_1 + \mathbf{F}_2. \tag{4.62}$$

This vector expression is introduced solely for clarity in the geometric explanation and does not modify the scalar treatment adopted in the previous equilibrium derivations.

According to the force equilibrium condition in Eq. (4.57), the resultant force of the two cable tensions must balance the gravity acting on the load. Let $\mathbf{F}_g$ denote the gravitational force vector applied at the load center, whose magnitude is mg and whose direction is vertically downward, i.e.,

$$\mathbf{F}_g = -mg\,\mathbf{e}_y, \tag{4.63}$$

where $\mathbf{e}_y$ is the unit vector along the upward vertical direction. The negative sign indicates that gravity acts opposite to $\mathbf{e}_y$. Hence, the resultant of the two tensions is given by

$$\mathbf{R} = -\mathbf{F}_g = mg\,\mathbf{e}_y, \tag{4.64}$$

which means that the combined effect of the two cable tensions produces a vertical force acting upward, equal in magnitude to the load weight.

Next, consider the moment equilibrium expressed by Eq. (4.60). It states that the algebraic sum of the torques generated by F_1 and F_2 about the load center (x, y) is zero, this condition implies that the resultant force $\mathbf{R}$ produces no moment about (x, y), hence its line of action must pass through (x, y).

In planar statics, the line of action of the resultant $\mathbf{R}$ for two non-parallel forces always passes through the intersection point $(\hat{x}, \hat{y})$ of their individual lines of action. Since $\mathbf{R}$ is vertical and passes through (x, y), the intersection P must lie on the same vertical line as the load center. Consequently, the horizontal coordinates of $(\hat{x}, \hat{y})$ and (x, y) coincide:

$$\hat{x} = x.$$

This relationship defines the geometric equilibrium condition: at static equilibrium, the extensions of the two cable tension lines intersect at a point directly below the load center, ensuring that the three forces (two tensions and gravity) are concurrent and generate no net moment.

Symmetry of cable angles at horizontal attitude. We now analyze the special case in which the load attitude angle is horizontal, i.e., $\gamma = 0$. Under this condition, we aim to show that the two cable inclination angles must be equal, $\alpha_1 = \alpha_2$.

Substituting $\gamma = 0$ into the moment equilibrium Eq. (4.60) gives

$$F_1 \cos\alpha_1 = F_2 \cos\alpha_2, \tag{4.65}$$

which indicates that the vertical components of the two cable tensions are equal in magnitude. This equality ensures that both tensions contribute the same vertical lifting force on the load.

From the first equation in the force balance condition Eq. (4.57), we have

$$F_1 \sin \alpha_1 = F_2 \sin \alpha_2, \tag{4.66}$$

which expresses the equality of the horizontal components of the two cable tensions, ensuring that no net horizontal force acts on the load.

Dividing Eq. (4.66) by Eq. (4.65) yields

$$\frac{F_1 \sin \alpha_1}{F_1 \cos \alpha_1} = \frac{F_2 \sin \alpha_2}{F_2 \cos \alpha_2}, \tag{4.67}$$

and since $F_1, F_2 > 0$, the force magnitudes cancel out, resulting in

$$\tan \alpha_1 = \tan \alpha_2. \tag{4.68}$$

Considering that both α_1 and α_2 belong to the range $(0, \pi/2)$ for the given crane geometry, the equality of their tangents implies

$$\alpha_1 = \alpha_2. \tag{4.69}$$

This result demonstrates that when the load is horizontal ($\gamma = 0$), the two cable inclination angles are symmetric with respect to the vertical axis passing through the load center. Such symmetry corresponds to a geometrically balanced and statically stable configuration of the DCC system.

Equilibrium equation. At this stage the three ingredients of equilibrium are established: geometric concurrency, force balance Eq. (4.57), and moment balance Eq. (4.60), together with geometric closure Eq. (4.5 – 4.6). They can be compactly written as

$$\begin{cases} F_1 \sin \alpha_1 - F_2 \sin \alpha_2 = 0 \\ F_1 \cos \alpha_1 + F_2 \cos \alpha_2 - mg = 0 \\ F_1 \cos(\alpha_1 - \gamma) - F_2 \cos(\alpha_2 + \gamma) = 0 \\ X_1 - X_2 + L_1 \sin \alpha_1 + L_2 \sin \alpha_2 + 2d \cos \gamma = 0 \\ Y_1 - Y_2 - L_1 \cos \alpha_1 + L_2 \cos \alpha_2 + 2d \sin \gamma = 0 \end{cases} \tag{4.70}$$

which is referred to as the *equilibrium equation* in the subsequent sections. Given the cable lengths L_1, L_2 and the system parameters X_1, X_2, Y_1, Y_2, m, g, d, the unknowns are F_1, F_2, α_1, α_2, γ, which are coupled by the nonlinear equilibrium equation above enforcing geometric closure and simultaneous force and moment balance.

Solving this nonlinear system numerically yields the equilibrium configuration of the sus-

pended load, represented by the cable angles α_1 and α_2 and the load inclination angle γ. In other words, for any prescribed pair of cable lengths (L_1, L_2), there exists a unique set of equilibrium orientations $(\alpha_1, \alpha_2, \gamma)$ that satisfies the static equilibrium conditions. This also confirms, from a static equilibrium perspective, that within the one dimensional manifold $(x, y, \gamma) = g(L_1, L_2) \subset \mathbb{R}^3$, there exists a physically meaningful equilibrium point $(x_{\text{eq}}, y_{\text{eq}}, \gamma_{\text{eq}}) = g_{\text{eq}}(L_1, L_2) \in \mathbb{R}^3$ that satisfies the equilibrium conditions. This mapping between the cable lengths and the load configuration establishes the fundamental relationship required for the subsequent design of the desired load location, where the inverse problem will be solved in order to determine $L_1(t), L_2(t)$ and $\gamma(t)$ from the desired load location.

4.6 Stability Analysis at the Equilibrium Point

4.6.1 Single Degree of Freedom Dynamics Model

As analyzed in Section 4.2.2 and 4.5, when L_1 and L_2 are fixed, all possible configurations (x, y, γ) form a one dimensional manifold $(x, y, \gamma) = g(L_1, L_2) \subset \mathbb{R}^3$. Within this manifold, there exists one and only one configuration $(x_{\text{eq}}, y_{\text{eq}}, \gamma_{\text{eq}}) = g_{\text{eq}}(L_1, L_2) \in \mathbb{R}^3$ that satisfies the equilibrium conditions. This configuration is referred to as the equilibrium point of the system. In the following, we first express the fixed length constraints in algebraic form and show how they reduce the geometry to a one dimensional curve parametrized by γ. Then, based on this parametrization, we construct a single coordinate Lagrangian model in γ that will be used for the stability analysis of the equilibrium.

For given cable lengths (L_1, L_2), from Eq. (4.10 – 4.11) the geometric configuration of the system is constrained by two algebraic equations:

$$Z_1(x, y, \gamma) = (x - d\cos\gamma - X_1)^2 + (y - d\sin\gamma - Y_1)^2 - L_1^2 = 0, \tag{4.71}$$

$$Z_2(x, y, \gamma) = (x + d\cos\gamma - X_2)^2 + (y + d\sin\gamma - Y_2)^2 - L_2^2 = 0. \tag{4.72}$$

Eq. (4.71 – 4.72) state that, for a given γ, the two load end attachments must lie on circles of radii L_1 and L_2 centered at (X_1, Y_1) and (X_2, Y_2), respectively. They encode the fact that the cable lengths are fixed, and therefore select the admissible triplets (x, y, γ).

The *Jacobian matrix* of the constraint Eq. (4.71 – 4.72) with respect to (x, y) is defined as

$$J(x, y, \gamma) = \begin{bmatrix} \dfrac{\partial Z_1}{\partial x} & \dfrac{\partial Z_1}{\partial y} \\ \dfrac{\partial Z_2}{\partial x} & \dfrac{\partial Z_2}{\partial y} \end{bmatrix} = \begin{bmatrix} J_{1x} & J_{1y} \\ J_{2x} & J_{2y} \end{bmatrix}, \tag{4.73}$$

from the explicit form of Z_1 and Z_2 in Eq. (4.71 – 4.72), the partial derivatives are obtained as

$$J_{1x} = 2(x - d\cos\gamma - X_1), \qquad J_{1y} = 2(y - d\sin\gamma - Y_1),$$

$$J_{2x} = 2(x + d\cos\gamma - X_2), \qquad J_{2y} = 2(y + d\sin\gamma - Y_2).$$

The Jacobian $J(x, y, \gamma)$ collects the partial derivatives of the two constraint functions Z_1 and Z_2 with respect to the load coordinates (x, y). Each row of J therefore represents how the corresponding constraint equation varies when the load center undergoes infinitesimal displacements in the horizontal or vertical direction. In this sense, J establishes the local geometric mapping between small changes in (x, y) and the induced variations in (Z_1, Z_2).

When the Jacobian $J(x, y, \gamma)$ is nonsingular, which holds throughout the admissible workspace, the *Implicit Function Theorem* can be applied. It ensures that the coordinates (x, y) can be locally expressed as smooth functions of the attitude angle γ. Specifically, there exist differentiable mappings $x(\gamma)$ and $y(\gamma)$ satisfying

$$Z_1(x(\gamma), y(\gamma), \gamma) = 0, \qquad Z_2(x(\gamma), y(\gamma), \gamma) = 0. \tag{4.74}$$

The theorem states that if a continuously differentiable mapping $\mathbf{Z}(x, y, \gamma) = [Z_1, Z_2]^\top$ satisfies $\mathbf{Z}(x_0, y_0, \gamma_0) = \mathbf{0}$ and its Jacobian matrix with respect to (x, y), i.e. $J(x_0, y_0, \gamma_0)$, is invertible, then there exist unique differentiable functions $x(\gamma)$ and $y(\gamma)$ in a neighborhood of γ_0 such that the constraint equations remain satisfied for all nearby values of γ, where (x_0, y_0, γ_0) denotes a reference configuration that satisfies the constraint equations $\mathbf{Z}(x_0, y_0, \gamma_0) = \mathbf{0}$. This result formally justifies the dependency relationships $x = x(\gamma)$ and $y = y(\gamma)$ used in the subsequent derivation of the single degree of freedom dynamic model. A detailed discussion of the Implicit Function Theorem can be found in standard mathematical analysis references [101, 102].

This result implies that, for given cable lengths (L_1, L_2), the load configuration can be completely described by a single variable γ. Eq. (4.74) therefore establishes that, under fixed cable lengths and a regular workspace (i.e., an invertible Jacobian J), the entire system configuration is uniquely determined by γ. Consequently, γ is adopted as the generalized coordinate describing motion along the one dimensional manifold defined by the fixed length constraints.

In the following derivations, this implicit formulation will be used to compute the first and second derivatives $x'(\gamma), y'(\gamma), x''(\gamma), y''(\gamma)$ appearing in the expressions of the kinetic and potential energies.

Since the constraint functions Z_1 and Z_2 in Eq. (4.74) are identically zero along the one dimensional manifold, their total derivatives with respect to γ also vanish. By applying the *chain rule* to both Z_1 and Z_2, each total derivative can be expanded as

$$\frac{dZ_i}{d\gamma} = \frac{\partial Z_i}{\partial x}x' + \frac{\partial Z_i}{\partial y}y' + \frac{\partial Z_i}{\partial \gamma} = 0, \qquad i = 1, 2.$$

Rewriting these two equations in matrix form gives

$$J(x,y,\gamma)\begin{bmatrix}x'\\y'\end{bmatrix}+B(x,y,\gamma)=0 \quad\Longrightarrow\quad \begin{bmatrix}x'\\y'\end{bmatrix}=-J^{-1}(x,y,\gamma)B(x,y,\gamma), \tag{4.75}$$

where $B(x,y,\gamma)$ is formed by the terms $\partial Z_i/\partial\gamma$ of the two constraint equations, that is,

$$B(x,y,\gamma)=\begin{bmatrix}J_{1x}(d\sin\gamma)+J_{1y}(-d\cos\gamma)\\J_{2x}(-d\sin\gamma)+J_{2y}(d\cos\gamma)\end{bmatrix}. \tag{4.76}$$

By solving Eq. (4.75), one obtains the derivatives $(x',y')^{\mathrm{T}}$ that describe how the load center moves along the constraint manifold as γ varies. Although $x(\gamma)$ and $y(\gamma)$ cannot be obtained in closed form, their derivatives can be computed algebraically from Eq. (4.75 – 4.76), and these results will be used later in the derivation of the kinetic and potential energies.

Differentiating Eq. (4.75) once more with respect to γ gives

$$J(x,y,\gamma)\begin{bmatrix}x''\\y''\end{bmatrix}+J'(x,y,\gamma)\begin{bmatrix}x'\\y'\end{bmatrix}+B'(x,y,\gamma)=0, \tag{4.77}$$

$$\begin{bmatrix}x''\\y''\end{bmatrix}=-J^{-1}(x,y,\gamma)\left(J'(x,y,\gamma)\begin{bmatrix}x'\\y'\end{bmatrix}+B'(x,y,\gamma)\right). \tag{4.78}$$

Eq. (4.75) with respect to γ, the second derivatives $x''(\gamma)$ and $y''(\gamma)$ are obtained. These quantities are required for the formulation of the kinetic and potential energies in the subsequent derivations.

To construct the single degree of freedom dynamic model in terms of the generalized coordinate γ, the Euler–Lagrange formulation is adopted, following the same modeling approach introduced in Section 4.3. A viscous damping term $w\dot{\gamma}$ is included to represent the energy dissipation caused by cable friction and other resistive effects, where $w\geq 0$ denotes the damping coefficient. The resulting equation of motion is

$$\frac{d}{dt}\left(\frac{\partial\mathcal{L}}{\partial\dot{\gamma}}\right)-\frac{\partial\mathcal{L}}{\partial\gamma}+w\dot{\gamma}=0, \tag{4.79}$$

where the Lagrangian is defined as

$$\mathcal{L}(\gamma,\dot{\gamma})=T-V. \tag{4.80}$$

According to Eq. (4.26), the kinetic energy is expressed as follow

$$T(\gamma,\dot{\gamma})=\frac{1}{2}m(x'^2+y'^2)\dot{\gamma}^2+\frac{1}{2}I_c\dot{\gamma}^2=\frac{1}{2}M(\gamma)\dot{\gamma}^2, \tag{4.81}$$

with

$$M(\gamma) = m(x'^2 + y'^2) + I_c, \qquad M'(\gamma) = 2m(x'x'' + y'y''). \tag{4.82}$$

The quantity $M(\gamma)$ plays the role of an effective inertia associated with the generalized coordinate γ. It depends on the geometry through $x'(\gamma)$ and $y'(\gamma)$, i.e., how the load center moves when the orientation changes. Its derivative $M'(\gamma)$ comes from differentiating M w.r.t. γ and will multiply $\dot{\gamma}^2$ in the equations of motion.

The potential energy is determined by the vertical position of the load center, and can be expressed as

$$V(\gamma) = mg\, y(\gamma), \qquad V'(\gamma) = mg\, y'(\gamma), \tag{4.83}$$

where $V'(\gamma)$ represents the generalized restoring torque associated with the coordinate γ. Thus

$$\mathcal{L}(\gamma, \dot{\gamma}) = \frac{1}{2} M(\gamma)\dot{\gamma}^2 - mg\, y(\gamma) \tag{4.84}$$

We compute

$$\begin{aligned} &\frac{\partial \mathcal{L}(\gamma, \dot{\gamma})}{\partial \dot{\gamma}} = M(\gamma)\dot{\gamma}, \qquad \frac{d}{dt}\left(M(\gamma)\dot{\gamma}\right) = M(\gamma)\ddot{\gamma} + M'(\gamma)\dot{\gamma}^2, \\ &\frac{\partial \mathcal{L}(\gamma, \dot{\gamma})}{\partial \gamma} = \frac{\partial}{\partial \gamma}\left(\frac{1}{2} M(\gamma)\dot{\gamma}^2 - V(\gamma)\right) = \frac{1}{2} M'(\gamma)\dot{\gamma}^2 - V'(\gamma). \end{aligned} \tag{4.85}$$

Based on Eq. (4.79 – 4.85), the resulting single degree of freedom dynamics can be written as

$$\boxed{M(\gamma)\,\ddot{\gamma} \;+\; \frac{1}{2} M'(\gamma)\,\dot{\gamma}^2 \;+\; w\,\dot{\gamma} \;+\; V'(\gamma) \;=\; 0.} \tag{4.86}$$

Eq. (4.86) is the reduced model in the single coordinate γ: $M(\gamma)\ddot{\gamma}$ is the inertial torque, $\frac{1}{2} M'(\gamma)\dot{\gamma}^2$ is a geometric correction due to the γ dependence of the inertia, $w\dot{\gamma}$ is the viscous damping torque, and $V'(\gamma)$ is the restoring torque induced by gravity. This compact form will be the starting point for the equilibrium characterization and the subsequent linear stability analysis.

4.6.2 Linear Stability Analysis

An equilibrium orientation γ_{eq} satisfies $\dot{\gamma} = 0$ and $\ddot{\gamma} = 0$ in Eq. (4.86). Substituting these into the equation gives the condition

$$V'(\gamma_{\text{eq}}) = mg\, y'(\gamma_{\text{eq}}) = 0, \tag{4.87}$$

which ensures that the total torque acting on the load is zero at equilibrium.

Define the small deviation

$$\tilde{\gamma} \triangleq \gamma - \gamma_{\text{eq}}, \qquad \dot{\tilde{\gamma}} = \dot{\gamma}, \;\; \ddot{\tilde{\gamma}} = \ddot{\gamma}. \tag{4.88}$$

We analyze very small motions around equilibrium, meaning that the deviation, velocity, and acceleration are all small quantities of the same order of magnitude,

$$\tilde{\gamma} = \mathcal{O}(\epsilon), \qquad \dot{\tilde{\gamma}} = \mathcal{O}(\epsilon), \qquad \ddot{\tilde{\gamma}} = \mathcal{O}(\epsilon). \tag{4.89}$$

Hence, their products such as $\tilde{\gamma}\ddot{\tilde{\gamma}}$ or $\dot{\tilde{\gamma}}^2$ are of second order, i.e.,

$$\tilde{\gamma}\ddot{\tilde{\gamma}}, \;\; \dot{\tilde{\gamma}}^2 = \mathcal{O}(\epsilon^2), \tag{4.90}$$

and are therefore neglected in the linear approximation. In other words, $\tilde{\gamma}$, $\dot{\tilde{\gamma}}$, and $\ddot{\tilde{\gamma}}$ are all first order infinitesimals, so that products of small quantities such as $\tilde{\gamma}\ddot{\tilde{\gamma}}$ or $\dot{\tilde{\gamma}}^2$ are of second order and omitted in the linearized model.

The function $M(\gamma)$ represents the inertia associated with the motion of the load and depends smoothly on the orientation γ. To analyze small oscillations around the equilibrium γ_{eq}, we linearize $M(\gamma)$ by means of a *Taylor expansion* around γ_{eq}. This expansion expresses the value of $M(\gamma)$ at any nearby γ as its equilibrium value plus the first order correction due to a small deviation $\tilde{\gamma} = \gamma - \gamma_{\text{eq}}$:

$$M(\gamma) = M(\gamma_{\text{eq}}) + M'(\gamma_{\text{eq}})\,\tilde{\gamma} + \mathcal{O}(\tilde{\gamma}^2) = M_{\text{eq}} + M'_{\text{eq}}\,\tilde{\gamma} + \mathcal{O}(\epsilon^2), \tag{4.91}$$

where $M_{\text{eq}} \triangleq M(\gamma_{\text{eq}}) > 0$ denotes the inertia at equilibrium and $M'_{\text{eq}} \triangleq M'(\gamma_{\text{eq}})$ is its local slope. The higher order term $\mathcal{O}(\tilde{\gamma}^2)$ collects all second and higher order contributions, which are neglected under the small angle assumption since $\tilde{\gamma}$ is infinitesimal.

In Eq. (4.86), this inertia function multiplies the acceleration $\ddot{\gamma} = \ddot{\tilde{\gamma}}$. Substituting the Eq. (4.91) gives

$$\big(M_{\text{eq}} + M'_{\text{eq}}\tilde{\gamma}\big)\ddot{\tilde{\gamma}} = M_{\text{eq}}\ddot{\tilde{\gamma}} + \underbrace{M'_{\text{eq}}\tilde{\gamma}\ddot{\tilde{\gamma}}}_{\mathcal{O}(\epsilon^2)}.$$

The second term involves the product of two small quantities, $\tilde{\gamma}$ and $\ddot{\tilde{\gamma}}$, and is therefore of order $\mathcal{O}(\epsilon^2)$ according to Eq. (4.89). As only first order terms are retained in the linear model, this contribution is neglected. Hence, to first order, the inertia term simplifies to

$$M(\gamma)\,\ddot{\gamma} \;\approx\; M_{\text{eq}}\,\ddot{\tilde{\gamma}}. \tag{4.92}$$

This approximation states that, within the range of small oscillations, the inertia can be treated as a constant equal to its equilibrium value M_{eq}.

The velocity squared inertial term $\frac{1}{2}M'(\gamma)\dot{\gamma}^2$ originates from the variation of the inertia

$M(\gamma)$ with respect to the orientation γ. Expanding $M'(\gamma)$ near γ_{eq} gives

$$\frac{1}{2}M'(\gamma)\dot{\gamma}^2 = \frac{1}{2}\big(M'_{\text{eq}} + \mathcal{O}(\tilde{\gamma})\big)\dot{\tilde{\gamma}}^2, \tag{4.93}$$

where $M'_{\text{eq}} \triangleq M'(\gamma_{\text{eq}})$ and the term $\mathcal{O}(\tilde{\gamma})$ arises from the Taylor expansion of $M'(\gamma)$, representing corrections of higher order proportional to the small deviation $\tilde{\gamma}$. Since $\dot{\tilde{\gamma}} = \mathcal{O}(\epsilon)$ according to Eq. (4.89), the quantity $\dot{\tilde{\gamma}}^2$ is of second order, i.e.,

$$\dot{\tilde{\gamma}}^2 = \mathcal{O}(\epsilon^2).$$

Hence, the entire term in Eq. (4.93) is also of order $\mathcal{O}(\epsilon^2)$, and can be safely neglected in the linear approximation:

$$\frac{1}{2}M'(\gamma)\dot{\gamma}^2 = \mathcal{O}(\epsilon^2) \;\approx\; 0. \tag{4.94}$$

Physically, this term corresponds to a higher order inertial correction due to the dependence of $M(\gamma)$ on γ, but its contribution is negligible when the angular motion around the equilibrium is small.

The potential function $V(\gamma)$ represents the gravitational potential energy of the suspended load, and its derivative $V'(\gamma)$ corresponds to the generalized restoring torque associated with the orientation γ. To linearize this restoring action around the equilibrium, we perform a Taylor expansion of $V'(\gamma)$ at γ_{eq}:

$$V'(\gamma) = V'(\gamma_{\text{eq}}) + V''(\gamma_{\text{eq}})(\gamma - \gamma_{\text{eq}}) + \mathcal{O}(\tilde{\gamma}^2) = V''(\gamma_{\text{eq}})\tilde{\gamma} + \mathcal{O}(\epsilon^2), \tag{4.95}$$

where we used the equilibrium condition $V'(\gamma_{\text{eq}}) = 0$ from Eq. (4.87).

Recalling that the potential energy is related to the vertical position $y(\gamma)$ of the load through $V(\gamma) = mg\,y(\gamma)$, its first and second derivatives are, respectively,

$$V'(\gamma) = mg\,y'(\gamma), \qquad V''(\gamma) = mg\,y''(\gamma). \tag{4.96}$$

Evaluating the latter at the equilibrium yields

$$V''(\gamma_{\text{eq}}) = mg\,y''(\gamma_{\text{eq}}). \tag{4.97}$$

To simplify notation and highlight its physical meaning, we introduce

$$k_{\text{eq}} \triangleq V''(\gamma_{\text{eq}}) = mg\,y''(\gamma_{\text{eq}}), \tag{4.98}$$

which represents the local slope of the restoring torque with respect to γ at the equilibrium configuration. Substituting this definition into Eq. (4.95) yields

$$V'(\gamma) \approx k_{\text{eq}}\,\tilde{\gamma}. \tag{4.99}$$

Substituting Eq. (4.92), Eq. (4.94), and Eq. (4.99) into Eq. (4.86), and using $\dot{\gamma} = \dot{\tilde{\gamma}}$, we obtain the linearized dynamics

$$M_{\mathrm{eq}}\,\ddot{\tilde{\gamma}} \;+\; w\,\dot{\tilde{\gamma}} \;+\; k_{\mathrm{eq}}\,\tilde{\gamma} \;=\; 0, \tag{4.100}$$

which represents a standard second order linear ordinary differential equation with constant coefficients.

Eq. (4.100) describes the small amplitude oscillation of the load orientation around its equilibrium configuration. The three terms respectively correspond to the inertial, damping, and restoring moments, in full analogy with a linear second order *mass–spring–damper* system. Assuming a trial solution of the form $\tilde{\gamma}(t) = e^{\lambda t}$, the characteristic equation is

$$M_{\mathrm{eq}}\lambda^2 + w\lambda + k_{\mathrm{eq}} = 0 \quad \Longrightarrow \quad \lambda_{1,2} = \frac{-w \pm \sqrt{w^2 - 4M_{\mathrm{eq}}k_{\mathrm{eq}}}}{2M_{\mathrm{eq}}}. \tag{4.101}$$

Hence:

- If $k_{\mathrm{eq}} > 0$, the restoring torque acts opposite to the deviation, yielding $\Re\lambda_{1,2} < 0$ for $w > 0$ (asymptotic stability), and purely imaginary eigenvalues $\lambda_{1,2} = \pm\mathrm{i}\sqrt{k_{\mathrm{eq}}/M_{\mathrm{eq}}}$ for $w = 0$ (Lyapunov stability).
- If $k_{\mathrm{eq}} < 0$, the restoring action is reversed and one root of Eq. (4.101) has a positive real part, corresponding to an unstable saddle–type equilibrium.

The parameter $k_{\mathrm{eq}} = mg\,y''(\gamma_{\mathrm{eq}})$ quantifies the local curvature of the load trajectory with respect to γ, that is, the sensitivity of the vertical position y to small orientation perturbations. In geometric terms, a positive k_{eq} means that when the load undergoes a small angular deviation, its center of mass moves slightly upward. As a result, gravity generates a restoring torque that pulls the load back toward the equilibrium position, indicating a stable configuration. If k_{eq} were negative, a small deviation would instead lower the center of mass, so gravity would act in the same direction as the disturbance, driving the system further away from equilibrium and making it unstable.

From the geometric analysis presented in Sec. 4.2.2, the configuration manifold obtained for fixed cable lengths (L_1, L_2) consists of two branches: the lower branch, located below the line joining (X_1, Y_1) and (X_2, Y_2), and the upper branch, located above it. Only the lower branch satisfies the static and torque equilibrium conditions of the suspended load and remains entirely within the feasible workspace of the DCC system. This branch corresponds to $k_{\mathrm{eq}} > 0$, representing a physically attainable and stable equilibrium configuration. The upper branch, by contrast, would correspond to $k_{\mathrm{eq}} < 0$, which geometrically represents an "over–the–line" configuration of the load center that violates both the geometric constraints and the force balance requirements. Hence, this case is not physically realizable, and only the $k_{\mathrm{eq}} > 0$ configuration

exists in practice.

In summary, the combined evidence from the linear stability analysis and the geometric manifold interpretation demonstrates that all physically admissible equilibrium configurations of the DCC system are locally stable.

In what follows, we consider the following case study to determine the system's equilibrium point under a fixed configuration (L_1, L_2) and to verify whether this equilibrium is stable.

$$X_1 = 20 \text{ m}, \quad Y_1 = 90 \text{ m}, \quad L_1 = 60 \text{ m}, \quad L_2 = 70 \text{ m}, \quad d = 10 \text{ m}$$

$$X_2 = 100 \text{ m}, \quad Y_2 = 100 \text{ m}, \quad D = 110 \text{ m} \quad m = 1 \text{ kg}, \quad g = 9.81 \; kg/s^2.$$

The angle γ is defined within the range $(-\pi/2, \pi/2)$, and the viscous damping coefficient is set to $w = 0$. Through numerical computation in MATLAB, the equilibrium values are obtained as

$$\gamma_{\text{eq}} = 0.0345, \quad k_{\text{eq}} = 131.0247.$$

Therefore, under this configuration, an equilibrium point γ_{eq} is identified. When $w > 0$, the equilibrium point is asymptotically stable, whereas for $w = 0$, it is Lyapunov stable.

Meanwhile, according to the *equilibrium equation* Eq. (4.70) derived in the previous subsection, the value of γ obtained by solving it numerically in MATLAB coincides exactly with γ_{eq}. This result confirms the correctness of the derived Eq. (4.70).

4.6.3 Energy Based Stability Analysis

While the linearized analysis establishes local stability, it is desirable to confirm that this property is intrinsic to the full nonlinear dynamics on the constant length manifold. Therefore, in this subsection a qualitative proof is provided using an energy based Lyapunov approach. Without relying on small-angle linearization or numerical simulation, the analysis demonstrates that, under mild geometric regularity and convexity assumptions, the equilibrium configuration is indeed asymptotically stable for the entire class of admissible parameters.

Consider the single degree of freedom dynamics Eq. (4.86) evolving on the admissible interval $\Gamma = (\underline{\gamma}, \overline{\gamma}) \subset (-\pi/2, \pi/2)$ determined by the fixed cable lengths (L_1, L_2). We make the following assumptions:

Assumption 4.2 *The Jacobian $J(x, y, \gamma)$ is nonsingular on Γ. Hence $(x(\gamma), y(\gamma))$ is unique and smooth, and $M(\gamma)$ is smooth with $0 < M_{\min} \leq M(\gamma) \leq M_{\max} < \infty$.*

Assumption 4.3 *There exists a unique $\gamma_{\text{eq}} \in \Gamma$ such that $V'(\gamma_{\text{eq}}) = 0$ and $V(\gamma) > V(\gamma_{\text{eq}})$ for*

all $\gamma \neq \gamma_{\text{eq}}$ *in* Γ.

Assumption 4.4 *Either* Γ *is bounded and* V *attains its unique minimum at* γ_{eq}*, or* $V(\gamma) \to +\infty$ *as* $\gamma \to \underline{\gamma}$ *or* $\gamma \to \overline{\gamma}$.

Assumptions 4.2 is satisfied on the admissible workspace where the two cable directions are not collinear. Assumptions 4.3 expresses the fact that, along the feasible manifold, the gravitational potential has a unique strict minimizer. We adopt the mechanical energy with the equilibrium potential subtracted

$$\mathcal{E}(\gamma, \dot{\gamma}) \;=\; \tfrac{1}{2} M(\gamma)\, \dot{\gamma}^2 \;+\; V(\gamma) - V(\gamma_{\text{eq}}). \tag{4.102}$$

By Assumptions 4.2 - 4.3, $\mathcal{E} \geq 0$ and $\mathcal{E} = 0$ iff $(\gamma, \dot{\gamma}) = (\gamma_{\text{eq}}, 0)$. Differentiating (4.102) along solutions of Eq. (4.86) yields

$$\begin{aligned} \dot{\mathcal{E}} &= \tfrac{1}{2} M'(\gamma)\dot{\gamma}^3 + M(\gamma)\dot{\gamma}\ddot{\gamma} + V'(\gamma)\dot{\gamma} \\ &= \dot{\gamma}\Big(M(\gamma)\ddot{\gamma} + \tfrac{1}{2} M'(\gamma)\dot{\gamma}^2 + V'(\gamma) \Big) = -\,w\,\dot{\gamma}^2 \;\leq\; 0, \end{aligned} \tag{4.103}$$

which shows that $\mathcal{E}$ is a strict Lyapunov function for $w > 0$ and a conserved quantity for $w = 0$.

Lyapunov stability for $w = 0$ **:** Under Assumptions 4.2 - 4.4 with $w = 0$, the equilibrium $(\gamma_{\text{eq}}, 0)$ is Lyapunov stable. Since $\dot{\mathcal{E}} = 0$, the energy is conserved and its positive definiteness at $(\gamma_{\text{eq}}, 0)$ implies that trajectories initialized sufficiently close remain on compact level sets of $\mathcal{E}$ around the equilibrium.

Asymptotic stability for $w > 0$ **:** Under Assumptions 4.2 - 4.4 and $w > 0$, the equilibrium $(\gamma_{\text{eq}}, 0)$ is asymptotically stable. If, in addition, every solution of Eq. (4.86) is forward complete and remains in Γ, the convergence is global on Γ. Since $\dot{\mathcal{E}} = -w\,\dot{\gamma}^2 \leq 0$ and $\mathcal{E} \geq 0$, $\mathcal{E}(t)$ converges. By LaSalle's invariance principle, any trajectory approaches the largest invariant set contained in

$$\mathcal{S} = \{(\gamma, \dot{\gamma}) \in \Gamma \times \mathbb{R} :\; \dot{\mathcal{E}} = 0\} = \{(\gamma, \dot{\gamma}) :\; \dot{\gamma} = 0\}.$$

On $\mathcal{S}$ the dynamics Eq. (4.86) reduces to $V'(\gamma) = 0$, which by Assumptions 4.3 implies $\gamma = \gamma_{\text{eq}}$ only. Therefore the largest invariant subset of $\mathcal{S}$ is the singleton $\{(\gamma_{\text{eq}}, 0)\}$ and the equilibrium is asymptotically stable.

The results of Sections 4.6.1 and 4.6.2 complement each other and provide a comprehensive characterization of the equilibrium stability of the dual crane system. The linearized stiffness criterion established that the equilibrium configuration is locally stable whenever the effective stiffness $k_{\text{eq}} = mg\, y''(\gamma_{\text{eq}})$ is positive, corresponding to a strict local minimum of the potential energy. The subsequent qualitative analysis confirmed that this property is not restricted to infinitesimal motions: under mild geometric regularity and convexity assumptions, the equilibrium remains Lyapunov stable for the full nonlinear dynamics, and asymptotically

stable in the presence of viscous damping. Therefore, the stability of the cooperative hoisting configuration is a structural feature of the constant length manifold, independent of small angle approximations or numerical conditions.

Chapter 5

Control Strategy Design and Simulation

Before proceeding to the controller design, it is essential to summarize the key results obtained from the previous chapters. The dynamic model derived earlier accurately captures the coupling effects among the cable lengths, load position, and orientation, providing a reliable foundation for control development. Building upon this model, this chapter aims to design a control strategy that ensures the coordinated motion of the two cranes while maintaining the desired load position and suppressing undesired sway. To this end, the control objectives and the main properties of the system are first discussed, followed by the detailed design and analysis of the proposed control method.

5.1 Control Objectives and System Properties

In practical applications, the dual crawler crane system requires extremely high installation precision, as the load must be lifted from a known initial configuration to a specified target position. The cooperative manipulation of the two cranes is achieved by simultaneously regulating the lengths of the two hoisting cables, which determine both the load position (x, y) and its orientation γ. The length of each cable is controlled through command signals sent to the crane's hoisting system. These signals regulate the operation of the winch, which adjusts the cable length by varying the rotational speed of its driving motor. In essence, the motor speed directly determines the rate at which the cable is wound or unwound, thereby controlling the motion of the suspended load.

The main control objective is to design a controller capable of guiding the load toward the desired installation position with high positioning accuracy, while effectively suppressing load swing during the lifting process.

The control objective in this work is defined over a finite time interval $[0, t_f]$, corresponding to the duration of the hoisting operation. Unlike asymptotic control schemes, which require convergence as $t \to \infty$, the present problem focuses on achieving the desired configuration precisely at the prescribed final time t_f.

The hoisting task is defined on the finite horizon $[0, t_f]$. Only the initial and final positions

of the load center are prescribed,

$$(x_d(0),\, y_d(0)), \qquad (x_d(t_f),\, y_d(t_f)),$$

and both endpoints are required to be equilibrium configurations. The associated equilibrium orientation and cable lengths are obtained through the equilibrium map $g_{\text{eq}}(\cdot)$,

$$\begin{aligned}(L_{1d}(0),\, L_{2d}(0),\, \gamma_d(0)) &= g_{\text{eq}}\big(x_d(0),\, y_d(0)\big),\\ (L_{1d}(t_f),\, L_{2d}(t_f),\, \gamma_d(t_f)) &= g_{\text{eq}}\big(x_d(t_f),\, y_d(t_f)\big).\end{aligned} \tag{5.1}$$

The desired trajectories are first designed for $L_{1d}(t)$ and $\gamma_d(t)$ by smoothly connecting their equilibrium values at the initial and final configurations using a velocity constrained profile. Then, based on these reference curves of $L_{1d}(t)$ and $\gamma_d(t)$, the corresponding $L_{2d}(t)$ trajectory is computed from the static equilibrium equations. This procedure ensures that every point along the designed reference path satisfies the equilibrium condition. $\dot{L}_{1d}(t), \dot{L}_{2d}(t)$ and $\dot{\gamma}(t)$ denote the velocity of the cable and γ. During the design stage the cable velocity limits are enforced,

$$|\dot{L}_{1d}(t)| \le V_{\max}, \quad \forall\, t \in [0, t_f], \tag{5.2}$$

and workspace bounds are respected.

At the final time t_f the load must reach the desired position and the induced equilibrium orientation within small tolerances $\varepsilon_x,\, \varepsilon_y,\, \varepsilon_\gamma$,

$$|x(t_f) - x_d(t_f)| \le \varepsilon_x, \qquad |y(t_f) - y_d(t_f)| \le \varepsilon_y, \qquad |\gamma(t_f) - \gamma_d(t_f)| \le \varepsilon_\gamma. \tag{5.3}$$

The controller acts on cable lengths and enforces terminal consistency with the designed references,

$$|L_i(t_f) - L_{id}(t_f)| \le \varepsilon_{L_i}, \quad i = 1, 2, \tag{5.4}$$

while satisfying the cable velocity limits and the workspace constraints for all $t \in [0, t_f]$.

5.2 Desired Velocity Profile Design

To ensure smooth motion of the suspended load and compliance with the cable velocity constraints, the desired reference trajectories of $L_{1d}(t)$ and $\gamma_d(t)$ are generated using a seventh order polynomial velocity profile. Compared with fifth–order or trapezoidal profiles, the seventh–order form provides zero initial and final velocity, acceleration, and jerk. This guarantees continuity up to the third derivative of position (i.e., C^3 smoothness), meaning that the trajectory has no discontinuities in position, velocity, acceleration, or jerk. Such high–order

smoothness eliminates abrupt changes in the dynamic response and is particularly important for minimizing residual oscillations of the lifted load.

For variable L_1 and γ, given its initial and final equilibrium values r_0 and r_f over the finite motion interval $[0, t_f]$, the desired trajectory is defined as

$$r_d(t) = a_0 + a_1 t + a_2 t^2 + a_3 t^3 + a_4 t^4 + a_5 t^5 + a_6 t^6 + a_7 t^7. \tag{5.5}$$

Imposing zero velocity, acceleration, and jerk at both endpoints leads to

$$a_0 = r_0, \quad a_1 = a_2 = a_3 = 0,$$

$$a_4 = 35\,\frac{(r_f - r_0)}{t_f^4}, \qquad a_5 = -84\,\frac{(r_f - r_0)}{t_f^5},$$

$$a_6 = 70\,\frac{(r_f - r_0)}{t_f^6}, \qquad a_7 = -20\,\frac{(r_f - r_0)}{t_f^7}.$$

The corresponding velocity profile is

$$\dot{r}_d(t) = \frac{dr_d}{dt} = 4a_4 t^3 + 5a_5 t^4 + 6a_6 t^5 + 7a_7 t^6, \tag{5.6}$$

which automatically starts and ends at zero and reaches its maximum around the midpoint of the motion.

To satisfy the physical limits of the hoisting mechanism, the cable velocities are restricted as

$$|\dot{L}_{1d}(t)| \le V_{\max}, \quad \forall\, t \in [0, t_f]. \tag{5.7}$$

After computing the initial trajectory, the peak cable speed $\dot{r}_{\max} = \max_t |\dot{r}_d(t)|$ is evaluated. If $\dot{r}_{\max} > V_{i,\max}$, the motion duration t_f is uniformly scaled by a factor

$$\rho = \frac{\dot{r}_{\max}}{V_{i,\max}}, \quad t_f \leftarrow \rho\, t_f, \tag{5.8}$$

and the polynomial coefficients are recalculated accordingly. This time scaling adjustment ensures that the designed profile strictly respects the cable velocity constraints without altering its geometric shape.

The complete trajectory generation process can be summarized as follows:

Algorithm 5: Seventh Order Polynomial Trajectory with Velocity Constraint

Input: r_0, r_f, nominal duration t_f, velocity limit $V_{\max}$

Output: Trajectory $r_d(t)$ satisfying $|\dot{r}_d(t)| \leq V_{\max}$

Compute $\Delta r = r_f - r_0$;

Compute coefficients $a_0 \dots a_7$;

Compute $\dot{r}_d(t)$ and $\dot{r}_{\max} = \max_t |\dot{r}_d(t)|$;

if $\dot{r}_{\max} > V_{\max}$ **then**

  Set $\rho = \dot{r}_{\max}/V_{\max}$, $\quad t_f \leftarrow \rho\, t_f$;

  Recompute coefficients a_k using new t_f;

end

Return $r_d(t)$ satisfying the velocity constraint;

The above procedure is applied to each reference variable $L_{1d}(t)$ and $\gamma_d(t)$. Given the initial equilibrium configurations $(L_{1d}(0), L_{2d}(0), \gamma_d(0))$ and final equilibrium configurations $(L_{1d}(t_f), L_{2d}(t_f), \gamma_d(t_f))$, each reference trajectory is generated independently by the polynomial function. Because the seventh order polynomial ensures smooth first, second, and third order derivatives, the resulting motion of the suspended load remains continuous in position, velocity, and acceleration, thereby reducing dynamic oscillations and internal tension peaks in the cables.

The design of $L_{2d}(t)$ is not independent; instead, it depends on the previously generated trajectories $L_{1d}(t)$ and $\gamma_d(t)$ in order to satisfy the equilibrium condition at each time instant. This sequential design procedure ensures that the desired reference trajectories are always consistent with the system's static equilibrium relationships. Such a formulation not only simplifies the control problem by reducing dynamic coupling effects, but also guarantees that when a horizontal lifting motion is required i.e., when $\gamma_d(t) = 0$ is prescribed the desired orientation remains identically zero throughout the entire operation.

This design provides a practical balance between smoothness, computational simplicity, and constraint feasibility. By enforcing the cable velocity limits at the design stage, the reference trajectories are guaranteed to be dynamically feasible and compatible with the mechanical limits of the dual crane system. Consequently, the subsequent controller can focus purely on accurate tracking of the desired profiles without the need for additional constraint handling, which simplifies the control implementation and enhances system stability. The following example illustrates how to generate the desired trajectories based on the above algorithm.

Using the parameters in Table 5.1, the results in Fig. 5.1 are obtained. It can be observed that the load reaches the final position at t=20 s without exceeding the maximum velocity limit. Moreover, the velocity, acceleration, and jerk are exactly zero at t=0 s and t=20 s.

When the final time t_f is initially set to 10 s, the generated trajectory is shown in Fig. 5.2. Since the maximum velocity limit $V_{\max}$ is exceeded, the algorithm automatically adjusts the

Table 5.1: Desired trajectory parameters.

Parameter	**Symbol**	**Value / Unit**
Initial position	r_0	0 m
Final position	r_f	3 m
Time	t_f	20 s
Maximum velocity	V_{max}	0.4 m/s

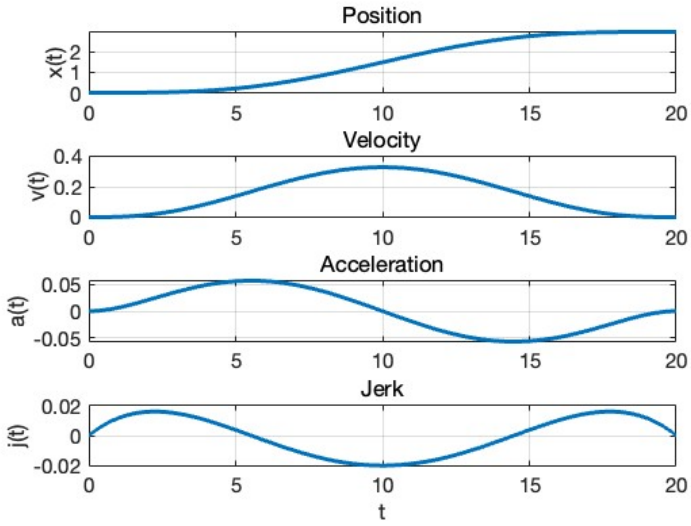

Figure 5.1: Desired trajectory with initial setup t_f = 20 s.

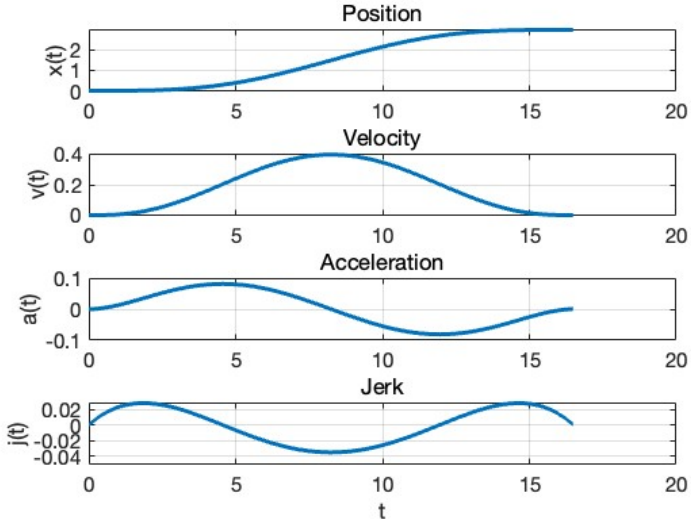

Figure 5.2: Desired trajectory with initial setup t_f = 10 s.

motion duration to 16.5 s. In this case, the peak velocity becomes 0.4 m/s, remaining within the specified velocity constraint.

This algorithm guarantees that the designed velocity profiles are smooth and strictly satisfy the cable velocity constraints. When the initially assigned task duration is too short and causes the cable velocity to exceed the admissible limit, the algorithm automatically adjusts the motion time until feasibility is achieved. As a result, there is no need for repeated manual tuning of the task duration to satisfy the velocity constraint, the method directly provides the minimum feasible motion time that ensures compliance with the cable velocity limits.

5.3 PID-Based Coupled Error Compensation Control

5.3.1 Controller Development

The DCC system under consideration is an underactuated mechanical system, where the number of controlled variables exceeds the number of available control inputs[103]. In particular, the control inputs act directly on the cable lengths L_1 and L_2, while the load orientation γ cannot be actuated directly and must instead be regulated indirectly through the coupled motion of the two cranes. This strong dynamic coupling among L_1, L_2, and γ makes the overall control problem significantly more challenging, as the system exhibits nonlinear and underactuated characteristics that are sensitive to parameter variations.

To overcome these difficulties, a coupled error compensation control strategy is adopted, which exploits the mutual coupling between the actuated and unactuated coordinates. The basic idea is to design control error signals that not only include position and velocity errors of each cable but also incorporate an additional compensation term associated with the load orientation error $(\gamma - \gamma_d)$. This coupling structure enables active damping of the load swing through the coordinated motion of the two cranes.

PID control laws are selected for this application because of their well known robustness, ease of implementation, and effectiveness in handling uncertain nonlinear dynamics when properly tuned. A PID controller combines three control actions: the proportional term $(K_{pi}e_i)$ provides an immediate response to the current error, the integral term $(K_{ii}\int e_i dt)$ compensates for steady-state offset, and the derivative term $(K_{di}\dot{e}_i)$ contributes to anticipative action and damping. Such a structure is particularly effective for mechanical systems like cranes, where the motion must be smooth, oscillations must be minimized, and model uncertainties may exist.

The control inputs τ_i $(i = 1, 2)$ applied to the winch drives are therefore expressed as

$$\tau_i = PID(e_i) = K_{pi}e_i + K_{ii}\int_0^t e_i(\xi)\, d\xi + K_{di}\dot{e}_i. \tag{5.9}$$

These two control inputs correspond to the elements of the generalized force vector $u = \left[\tau_1(t), \tau_2(t), 0\right]^\top$ in the previously derived dynamic model Eq. (4.53). The fact that the control

input associated with γ is zero further confirms that the system is underactuated, as the load orientation cannot be directly controlled but only influenced through the coordinated actions of the two cable forces. Here, K_{pi}, K_{ii}, and K_{di} denote the proportional, integral, and derivative gains of the i-th crane, respectively. Their tuning is carried out to achieve a trade-off between fast response, limited overshoot, and sufficient damping of the load oscillations.

The key component of the proposed strategy lies in the definition of the control error signals are defined as

$$\begin{aligned} e_1(t) &= \dot{L}_{1d} - \dot{L}_1 + \eta_{11}(L_{1d} - L_1) - \eta_{12}(\gamma - \gamma_d), \\ e_2(t) &= \dot{L}_{2d} - \dot{L}_2 + \eta_{21}(L_{2d} - L_2) + \eta_{22}(\gamma - \gamma_d), \end{aligned} \tag{5.10}$$

where $\eta_{ij} > 0$ $(i, j = 1, 2)$ are positive design parameters acting as coupling gains.

Each error signal $e_i(t)$ combines three components: 1. the cable velocity tracking error $(\dot{L}_{id} - \dot{L}_i)$; 2. the cable length tracking error $(L_{id} - L_i)$ weighted by η_{i1}; and 3. a coupling compensation term related to the load swing angle $(\gamma - \gamma_d)$, weighted by η_{i2}.

The purpose of the last term is to introduce an active interconnection between the two crane subsystems, so that orientation deviations of the load induce corrective actions on the cable velocities. Specifically, the sign of the coupling term is opposite in the two error equations: a negative sign in $e_1(t)$ and a positive sign in $e_2(t)$. This choice is physically consistent with the geometry of the dual crane system. When the load rotates clockwise (i.e., $\gamma > \gamma_d$), the left cable (L_1) should slightly shorten while the right cable (L_2) should slightly lengthen to restore the equilibrium orientation. By assigning opposite signs to the γ-related terms, the control action automatically generates a restoring torque that counteracts the swing motion and drives γ back toward γ_d. This mechanism effectively couples the two cable subsystems, allowing the unactuated variable γ to be indirectly stabilized through coordinated variations of L_1 and L_2.

The error dynamics defined in Eq. (5.10) provide the basis for the coupled PID control structure. Once the signals $e_1(t)$ and $e_2(t)$ are driven to zero, both the cable lengths and the load orientation converge toward their desired trajectories, achieving coordinated load positioning and swing suppression.

The controller gains appearing in the error dynamics of Eq. (5.10) were selected following a structured tuning procedure. The proportional, integral, and derivative gains of the PID controller were initially chosen according to classical qualitative tuning principles widely adopted in the PID control literature [104, 105]. In particular, the proportional gain was adjusted to shape the overall responsiveness of the cable velocity tracking, the integral gain was introduced to compensate steady-state errors arising from modeling inaccuracies and constant disturbances, and the derivative gain was used to provide additional damping and mitigate oscillatory behavior induced by the coupled crane dynamics. These principles were employed to

obtain a stabilizing initial set of gains with satisfactory transient performance.

Starting from this initial configuration, the PID gains were further refined through simulation-based tuning in order to account for the nonlinear, constrained, and cooperative nature of the dual-crane system. During this refinement stage, the proportional gains were tuned to balance tracking accuracy and robustness, the integral gains were kept sufficiently small to avoid slow oscillations and windup effects, and the derivative gains were adjusted to improve damping without amplifying measurement noise.

The coupling gains η_{ij} were then tuned by explicitly exploiting the structure of the composite error signals. The gains η_{i1} associated with the cable length errors were first adjusted to ensure adequate convergence of L_i toward L_{id} while preserving coordinated motion between the two subsystems. Subsequently, the gains η_{i2} related to the load orientation error were progressively increased to enhance the attraction of the closed-loop trajectories toward the equilibrium manifold. Since the load orientation γ is not directly actuated, larger values of η_{i2} were required to effectively suppress attitude deviations while maintaining smooth control actions.

The final parameter values represent a compromise between tracking accuracy, swing suppression, coordination effectiveness, and robustness, and were validated through extensive simulation studies.

Algorithm 6: Simulation and Control Procedure

Input: Initial and final load coordinates (x_0, y_0) and (x_f, y_f), total lifting time t_f, physical parameters $(m, g, d, X_i, Y_i), i = 1, 2$, controller gains.

Output: Time histories of (L_1, L_2, γ, x, y) and performance indices.

1. Initialization:

Set the simulation step and time grid.

Load system parameters including mass, gravity, load half-length, anchor coordinates and friction matrix.

2. Equilibrium Configuration:

Using *equilibrium equation* to compute the initial and final static equilibrium states $(L_1(0), L_2(0), \gamma(0))$ and $(L_1(t_f), L_2(t_f), \gamma(t_f))$ based on the given load positions.

3. Desired Trajectory Generation:

Use a smooth polynomial generator Algorithm 5 to create reference trajectories $L_{1d}(t)$ and $\gamma_d(t)$ ensuring zero initial and final velocities. Then, $L_{2d}(t)$ is computed from the equilibrium equations using the predefined $L_{1d}(t)$ and $\gamma_d(t)$.

4. Evolution of Dynamic Systems:

At each time step, execute the following:

1. Compute cable angles α_1, α_2 by solving geometric constraints Algorithm 4.
2. Evaluate composite error signals e_1, e_2 for L_1 and L_2.
3. Update the state derivatives $\dot{q}$ and $\ddot{q}$.

5. Post-Processing:

Reconstruct the load center coordinates (x, y) through the forward kinematics Eq. (4.19).

6. Visualization and Results:

Plot time histories of actual and desired L_1, L_2, and γ.

Plot cable velocities $\dot{L}_1$, $\dot{L}_2$, and load position (x, y) variations.

5.3.2 Discussion on the Stability of the Closed-loop System

The control inputs τ_i $(i = 1, 2)$ applied to the winch drives are generated by PID controllers acting on the coupled error signals $e_1(t)$ and $e_2(t)$, as defined in Eq. (5.10). These error signals depend on the cable length tracking errors $L_{id} - L_i$, the velocity tracking errors $\dot{L}_{id} - \dot{L}_i$, and the attitude tracking error $\gamma - \gamma_d$. When $e_1(t)$ and $e_2(t)$ converge to zero, both cable lengths and the load orientation converge to their desired trajectories, leading to coordinated load positioning and swing suppression.

Before proceeding with the stability discussion, it is worth clarifying the role of the equilibrium configurations in the controller design. The reference trajectories considered in this work are generated so that, at each time instant, they correspond to a statically balanced configuration of the suspended load. Accordingly, the closed-loop objective is not to stabilize the system around a single fixed equilibrium point, but to keep the system state close to a family of equilibrium configurations that evolve over time. The controller is designed to reduce deviations from these equilibrium configurations through the coupled error signals, while allowing the desired motion to progress smoothly along the reference trajectory. From this viewpoint, the stability discussion focuses on the suppression of tracking errors around the equilibrium configurations rather than on pointwise stabilization.

We now discuss why the proposed control law, when combined with the trajectory generation strategy, maintains stable closed-loop behaviour along the motion. For this purpose, let (L_1, L_2, γ) denote the cable lengths and the load attitude angle of the DCC system. The desired trajectories $L_{1d}(t)$ and $L_{2d}(t)$ are smooth and slowly varying, and the desired attitude is defined as

$$\gamma_d(t) = \gamma_{\text{eq}}\big(L_{1d}(t), L_{2d}(t)\big),$$

where $\gamma_{\text{eq}}(L_1, L_2)$ is the equilibrium attitude satisfying the *equilibrium equation* derived earlier in Section 4.6. The set of all such equilibrium configurations forms the equilibrium manifold

$$\mathcal{M} = \{(L_1, L_2, \gamma) : \ \gamma = \gamma_{\text{eq}}(L_1, L_2)\},$$

previously introduced and discussed. By construction, the reference trajectory evolves on $\mathcal{M}$, ensuring that every reference point corresponds to a balanced configuration of the suspended load.

When the cable lengths (L_1, L_2) are held constant, the attitude dynamics along $\mathcal{M}$ include viscous friction terms that dissipate energy, and therefore γ naturally converges to $\gamma_{\text{eq}}(L_1, L_2)$. Moreover, in the full DCC dynamics all generalized coordinates (L_1, L_2, γ) are subject to viscous damping through the term $-F\dot{q}$ in

$$M(q)\ddot{q} + C(q, \dot{q})\dot{q} + G(q) = u - F\dot{q}.$$

Thus, both the attitude and the cable-length dynamics possess intrinsic dissipativity, which promotes the decay of tracking errors and contributes to the open-loop attractivity of the subsystem dynamics along $\mathcal{M}$. A similar dissipative effect has been analysed for container cranes in Bartolini *et al.* [86], where damping plays a key role in ensuring asymptotic convergence of the swing dynamics on an appropriate manifold. Although the control framework in [86] differs from the PID-based approach adopted here, the qualitative behaviour of the attitude dynamics is consistent with the open-loop convergence observed on $\mathcal{M}$.

To analyse the behaviour of the complete closed-loop system, the desired trajectories

$L_{1d}(t)$ and $L_{2d}(t)$ are regarded as slowly time-varying scheduling variables,

$$\sigma(t) = [L_{1d}(t), L_{2d}(t)].$$

If the reference were frozen at $\sigma = \bar{\sigma}$, the closed-loop system would be time invariant, and the tracking-error vector $z(t)$ would satisfy the linearized dynamics

$$\dot{z} = A_c(\bar{\sigma})\, z,$$

where $A_c(\bar{\sigma})$ is the closed-loop Jacobian at the corresponding equilibrium. Since $A_c(\bar{\sigma})$ is Hurwitz for every admissible $\bar{\sigma}$, all frozen-time closed loops are locally asymptotically stable.

The actual system is time-varying because the scheduling variables $\sigma(t)$ change during motion. Several classical results in the gain-scheduling and linear parameter-varying literature [106–108] provide sufficient conditions for guaranteeing the stability of parameter-varying systems by imposing upper bounds on the rate of change of the scheduling parameters. However, these conditions are typically very conservative: the admissible parameter variation rates are often so small as to be practically meaningless, and the computed upper bounds depend strongly on the specific analytical procedure used to derive them, usually diverging significantly from the true bounds of the system. In particular, Shamma [107] developed a Lyapunov-based theoretical framework for analyzing gain-scheduled controllers, establishing sufficient conditions under which a time-varying system remains exponentially stable provided that the scheduling parameters evolve slowly.

Corriga *et al.* [109] applied these ideas to a crane model in which the rope length is the varying parameter. By introducing a suitable time-scaling transformation, they reduced the family of frozen models to a single time-invariant representation and designed an implicit gain-scheduling controller. A Lyapunov-like theorem due to Shamma was then used to estimate an upper bound on the admissible rope-length variation rate ensuring closed-loop stability under nominal operating conditions. As reported in their study, even with this approach the resulting bounds remain difficult to compute precisely and are often overly conservative. This difficulty is also present in our DCC setting: determining a precise upper bound on $\|\dot{\sigma}(t)\|$ is challenging due to the complex and nonlinear coupling of our crane model.

Nevertheless, these studies support the following qualitative rule: if all frozen-time closed loops are stable and the scheduling variables vary sufficiently slowly, then the behaviour of the time-varying gain-scheduled system remains close to that of the frozen systems and preserves their stability properties. In our case, $\sigma(t) = [L_{1d}(t), L_{2d}(t)]$ is generated by a smooth trajectory planner, ensuring a small rate $\|\dot{\sigma}(t)\|$ and therefore a closed-loop behaviour consistent with the above gain-scheduling principle.

Based on the above considerations, the following conclusion can be drawn: the frozen-time closed loops are stable, the drift induced by the time-varying reference is sufficiently

slow, and the intrinsic damping of the system suppresses the perturbations generated by this drift. As a result, the overall closed-loop behaviour of the DCC system is expected to remain stable throughout the motion. This conclusion is supported by the numerical results presented in Section 5.4.3. For all four operating modes and a simulation horizon of $400\,\mathrm{s}$, the attitude γ tracking mean absolute erro satisfies

$$|\gamma(t) - \gamma_{\mathrm{eq}}(L_1(t), L_2(t))| < 6 \times 10^{-6},$$

demonstrating that the system is able to track the slowly varying reference trajectory on the equilibrium manifold with high accuracy. This level of tracking performance is consistent with the gain-scheduling stability principle and provides supportive evidence regarding the effectiveness of the proposed control strategy.

5.4 Simulation Case Study

To validate the effectiveness of the proposed dynamic model and the control strategy, two representative simulation cases are carried out using the DCC system. The objective of these simulations is to evaluate the system behavior, trajectory tracking performance, and load swing suppression capability under different geometric configurations.

The first case considers a perfectly symmetric setup, where the two cranes are identical and their boom tip anchor points are positioned at the same height and equidistant from the load centerline. This configuration allows highlighting the intrinsic symmetry of the system and provides a clear reference for analyzing the cooperative lifting behavior.

The second case investigates a more general and realistic scenario, where the cranes differ in geometry and their anchor points are located at different heights. This asymmetrical configuration introduces coupling imbalances and nonuniform load distribution, representing practical conditions frequently encountered in real construction and industrial hoisting tasks. Comparing the results of the two cases enables a comprehensive assessment of the proposed control scheme's adaptability to varying system geometries and operational conditions.

5.4.1 Case 1: Symmetric Configuration with Horizontal Hoisting Task

In this case, we simulate a representative lifting operation that commonly occurs in real industrial and civil engineering projects. The scenario corresponds to a cooperative hoisting task where the load must be lifted vertically while maintaining a strictly horizontal attitude throughout the entire motion. This type of operation is typical in the installation of large bridge segments, prefabricated building components, or cylindrical vessels in petrochemical plants, where even a slight angular deviation of the lifted structure may cause significant alignment

errors or mechanical stress concentrations during assembly. In such lifting operations, crawler cranes offer significant practical advantages. Before the hoisting process begins, both cranes can be repositioned relative to the load, and their boom lengths and inclination angles can be adjusted independently. Through these preliminary adjustments, the two cranes can be configured into an approximately symmetric arrangement with respect to the load centerline. This flexibility makes it possible to establish an optimal initial configuration that minimizes load imbalance, ensures equal tension in both cables, and facilitates a stable and coordinated lifting motion.

To replicate these practical conditions, the two crawler cranes are assumed to be identical and symmetrically arranged with respect to the load centerline. Their boom anchor points are positioned at the same height and have equal horizontal distances from the midpoint of the load in the initial configuration. Under this geometric symmetry, both cranes are expected to share the lifting effort equally, resulting in a uniform tension distribution along the cables. The control objective is to ensure that the load is hoisted along a vertical path, reaching the target height while keeping its orientation angle γ constant and close to zero during the entire motion.

This symmetric configuration provides an ideal baseline for assessing the performance of the proposed control strategy under well-balanced conditions. It enables a clear evaluation of how accurately the controller can coordinate the motion of both cranes, achieve synchronized cable length variations, and suppress residual oscillations of the load without introducing undesired rotations. Moreover, the insights gained from this controlled and symmetric setup will serve as a reference for analyzing more complex and asymmetric configurations in the following section.

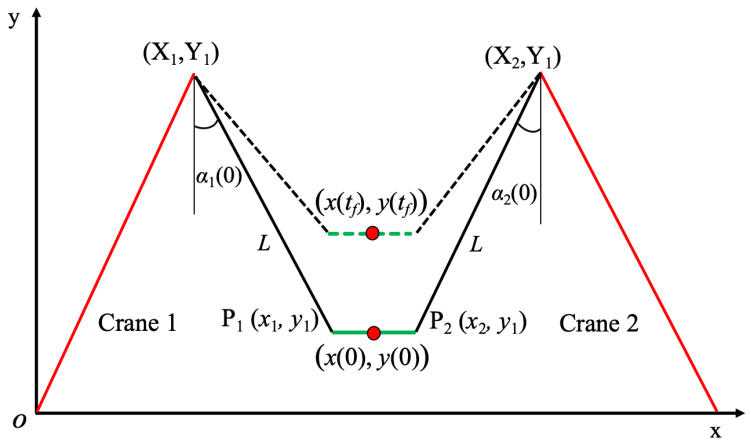

Figure 5.3: Case 1: Configuration that allows hosting the load keeping it always horizontal:here $x(0) = x(t_f) = (X1 + X2)/2$.

Fig. 5.3 illustrates the schematic configuration of the dual crawler crane system under the symmetric arrangement. The corresponding crane parameters and controller gain values used in the simulation are listed in Table 5.2.

Table 5.2: Case 1 parameters of the DCC system.

Parameter and gain	**Symbol**	**Value / Unit**
Coordinate of the boom 1 anchor	(X_1, Y_1)	(20, 100) m
Coordinate of the boom 2 anchor	(X_2, Y_2)	(100, 100) m
Mass of the load	m	2000 kg
Half length of the load	d	10 m
Gravitational acceleration	g	9.81 m/s^2
Friction coefficients	F	$diag(0.1, 0.1, 0.05)$
Initial load coordinate	$(x(0),\ y(0))$	(60, 30) m
Final load coordinate	$(x(t_f),\ y(t_f))$	(60, 60) m
Total simulation duration	t_f	200 s
Maximum cable velocity	$V_{i,max}, i = 1, 2$	0.3 m/s
Coupling gains	$\eta_{i1}, i = 1, 2$	3
Coupling gains	$\eta_{2i}, i = 1, 2$	200
Proportional gain	$K_{pi}, i = 1, 2$	100
Integral gain	$K_{ij}, j = 1, 2$	0.8
Derivative gain	$K_{di}, i = 1, 2$	5

The simulation is carried out in MATLAB. Based on the specified initial and final coordinates of the load, the corresponding equilibrium configurations are first computed as follows

$$L_1(0) = 76.157, \quad L_2(0) = 76.157, \quad \gamma(0) = 0,$$

$$L_1(t_f) = 50, \quad L_2(t_f) = 50, \quad \gamma(t_f) = 0.$$

The smoothly designed reference trajectories $L_{1d}(t), L_{2d}(t)$, and $\gamma_d(t)$, together with their actual responses, are shown in Fig. 5.4. It can be observed that the actual trajectories of both cables perfectly coincide with their reference profiles, while the deviation between the actual and desired values of γ remains very small. Fig. 5.5 also illustrates the time evolution of these tracking errors, showing that the cable length errors are within the millimeter range. Fig. 5.6 shows the velocity profiles of the two cables. It can be seen that the velocity trajectories are smooth and remain entirely within the maximum cable velocity constraint of 0.3 m/s.

Fig. 5.7 presents the time histories of the load coordinates $x(t)$ and $y(t)$. The horizontal position $x(t)$ remains constant throughout the motion, while the vertical coordinate $y(t)$ increases smoothly until the load reaches the prescribed target position at the end of the lifting process. Fig. 5.8 shows the load trajectory in the Cartesian plane. Since the system adopts a symmetric configuration and the desired motion is designed to maintain the load in a horizontal attitude, the resulting trajectory is vertical. The distribution of the sampled points, denser at the

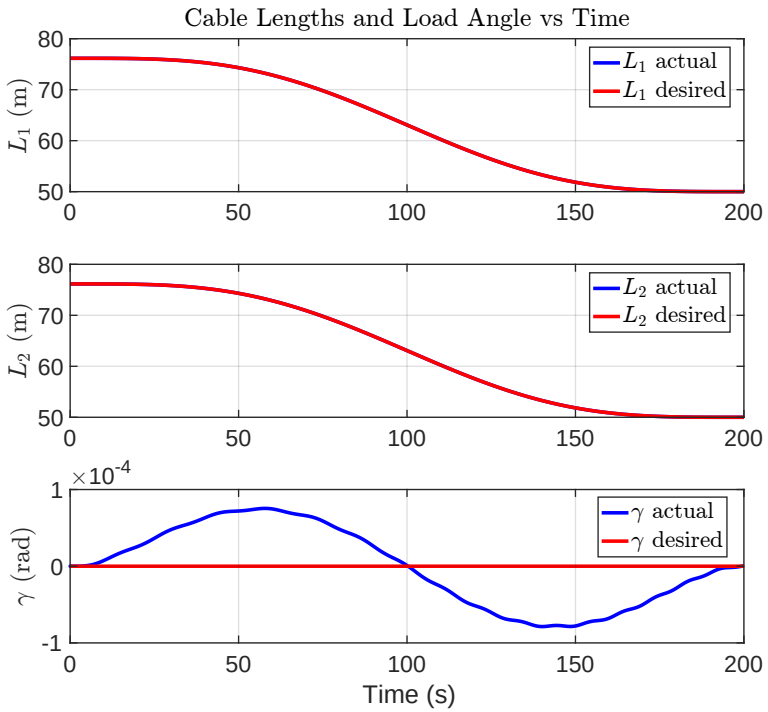

Figure 5.4: Case 1: Actual and desired cable lengths and load angle vs time.

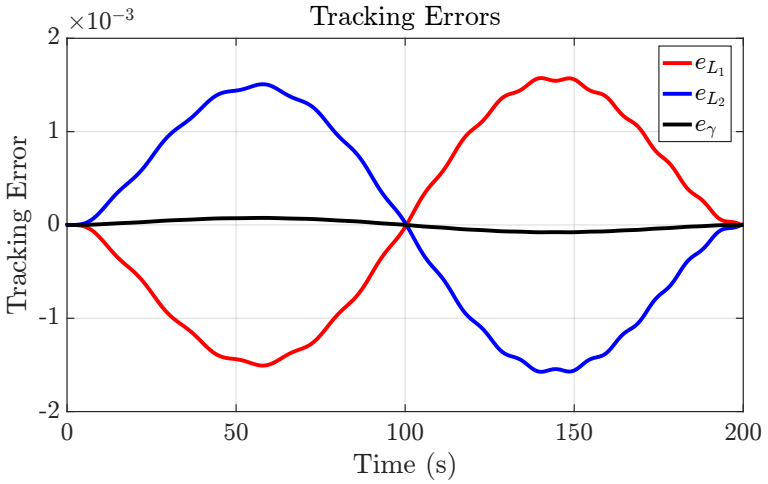

Figure 5.5: Case 1: Tracking errors between actual and desired cable lengths and load angle.

beginning and end of the motion and sparser in the middle, reflects the velocity profile adopted for the lifting process: a smooth acceleration phase, a quasi-uniform mid-motion, and a deceleration phase before reaching the target position. Fig. 5.9 shows the time evolution of the control inputs τ_1 and τ_2 corresponding to the two cable actuators. After a short initial transient, both inputs evolve smoothly and remain bounded throughout the lifting process, indicating that the control law does not rely on abrupt or oscillatory actuation. The two control inputs exhibit very similar profiles over the entire motion, which is consistent with the symmetric configuration adopted in Case 1 and with the vertically oriented reference trajectory. The small differences

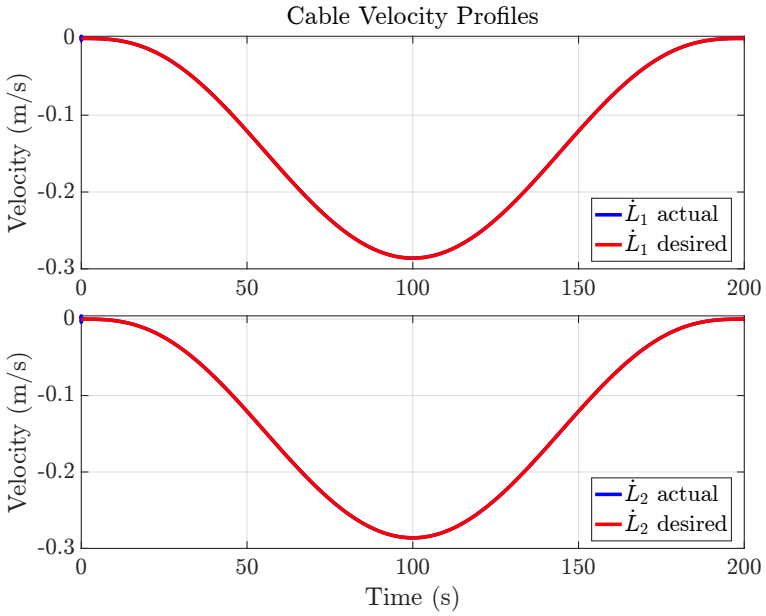

Figure 5.6: Case 1: Actual and desired cable velocity vs time.

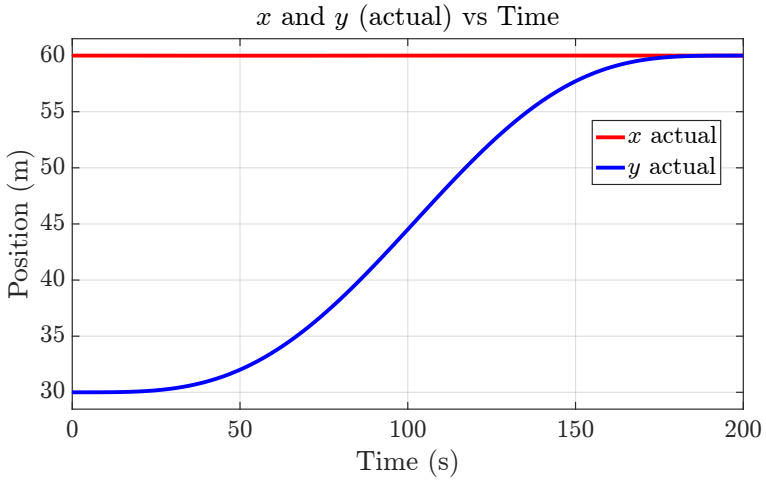

Figure 5.7: Case 1: Coordinate of the load vs time

between τ_1 and τ_2 are attributable to transient effects and dynamic coupling, and do not indicate any significant imbalance in the actuation effort. Overall, the smooth and monotonic evolution of the control inputs is coherent with the observed load trajectories and confirms that the proposed reference generation and control strategy yield stable and well-conditioned closed-loop behaviour in the symmetric lifting scenario. These results confirm that the proposed reference trajectory design enables the load to move vertically while preserving the horizontal orientation throughout the entire lifting motion.

For this case, the system is designed such that the initial and final configurations correspond to static equilibrium conditions. This ensures that the load starts and finishes the motion at stable equilibrium points, although during the lifting phase the system does not necessarily

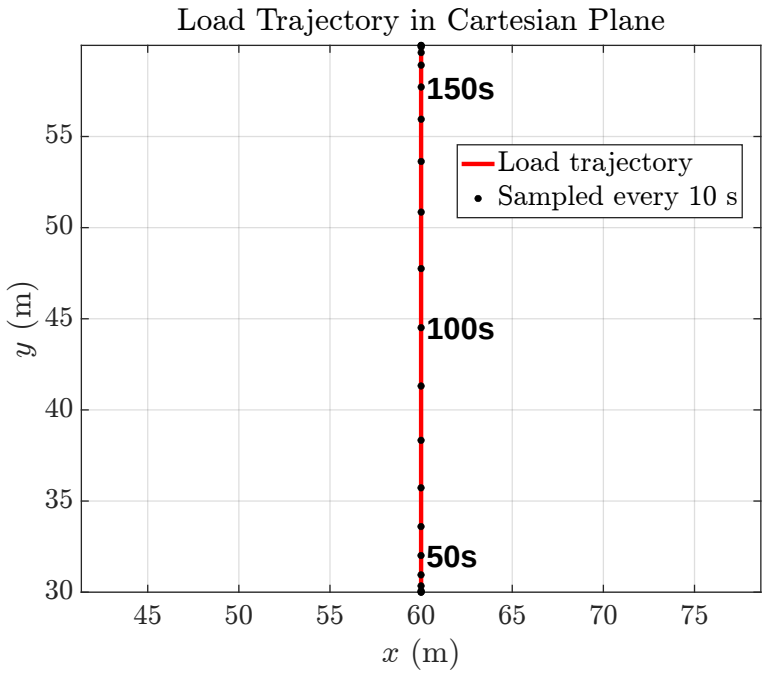

Figure 5.8: Case 1: Load trajectory in Cartesian plane.

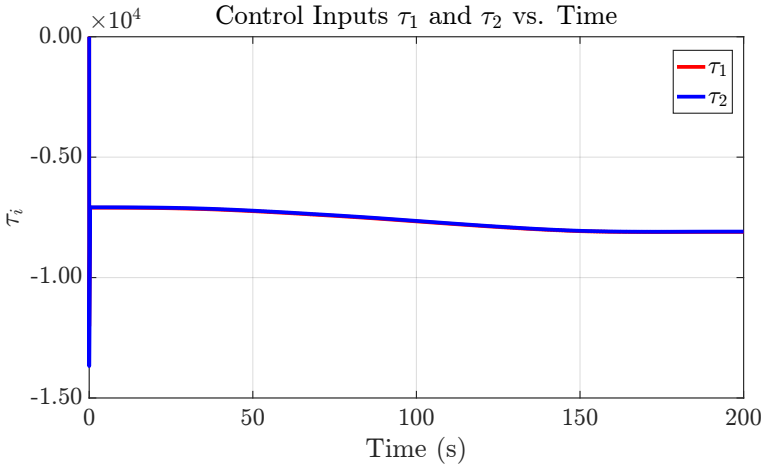

Figure 5.9: Case 1: Time evolution of the control inputs τ_1 and τ_2.

remain in equilibrium at every instant. However, under this symmetric configuration, maintaining a purely vertical lifting trajectory inherently preserves the equilibrium condition throughout most of the motion. This geometric symmetry effectively enhances the control performance, as the system experiences minimal coupling effects and the load orientation remains well balanced.

The results of this case study confirm the effectiveness of the proposed control law in achieving accurate trajectory tracking and stable cooperative lifting. Furthermore, this symmetric scenario provides a solid reference basis for the subsequent analysis of asymmetric configurations.

5.4.2 Case 2: Asymmetric Configuration with Horizontal Hoisting Task

Case 2 considers an asymmetric geometric configuration, as illustrated in Fig. 5.10. In this layout, the boom anchor anchor points of the two cranes are positioned at different heights, resulting in an unequal geometry between the two lifting subsystems. Such a configuration implies that, even if the load is required to remain horizontal throughout the lifting process, the system cannot maintain an exact equilibrium condition at every instant. The inherent geometric imbalance introduces additional coupling effects and nonlinear interactions between the two cranes, which significantly increase the complexity of the control problem.

This scenario is highly representative of real construction and industrial lifting tasks, where it is often impossible to deploy two identical cranes or to achieve a perfectly symmetric arrangement. Differences in crane structure, capacity, or working height may lead to unavoidable geometric asymmetries. Under these conditions, maintaining a strictly horizontal attitude of the load during vertical lifting becomes a demanding control objective, requiring precise coordination between the cable velocities of both cranes.

The simulation of this asymmetric case serves to assess the robustness and adaptability of the proposed control strategy under nonideal working conditions. By testing the controller in this more challenging configuration, we verify its capability to compensate for geometric imbalance and maintain accurate load alignment, thus demonstrating its potential applicability to a broad range of practical cooperative hoisting operations.

The objective in Case 2 is to reach the same final lifting height $y(t_f)$ as in Case 1 within a prescribed time horizon while maintaining a strictly horizontal load attitude $\gamma(t_f) = 0$. This procedure ensures that the load remains horizontal throughout the entire lifting process. It also explains why $L_{1d}(t)$ and $\gamma_d(t)$ are designed first, followed by $L_{2d}(t)$. Otherwise, in this asymmetric configuration, if $L_{1d}(t)$ and $L_{2d}(t)$ were designed independently, the corresponding equilibrium trajectory $\gamma_d(t)$ could not remain zero, and the load would fail to maintain a perfectly horizontal attitude during the motion. The simulation parameters and controller gains are reported in Table 5.3.

Based on the specified initial and final coordinates of the load, the corresponding equilibrium configurations are first computed as follows

$$L_1(0) = 55.902, \quad L_2(0) = 78.262, \quad \gamma(0) = 0,$$

$$L_1(t_f) = 28.284, \quad L_2(t_f) = 56.569, \quad \gamma(t_f) = 0.$$

Fig. 5.11 presents the time histories of the cable lengths and the load orientation angle γ. It can be observed that the actual trajectories of both cables perfectly coincide with their reference

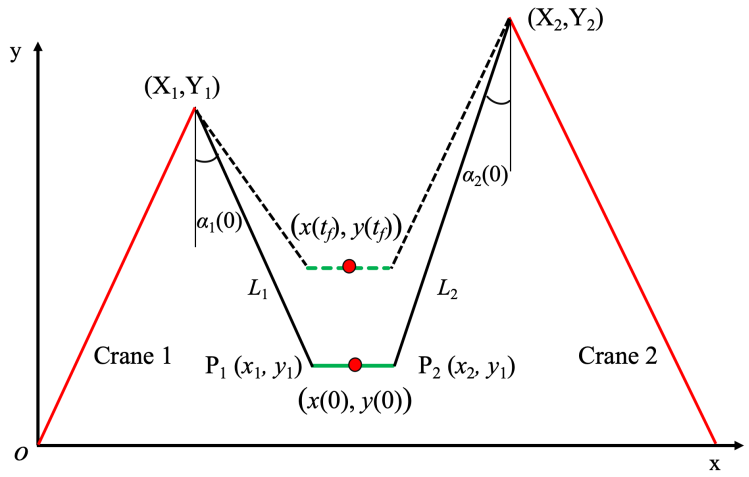

Figure 5.10: Case 2: Asymmetric setup under which the load is hoisted while maintaining a horizontal orientation from start to finish.

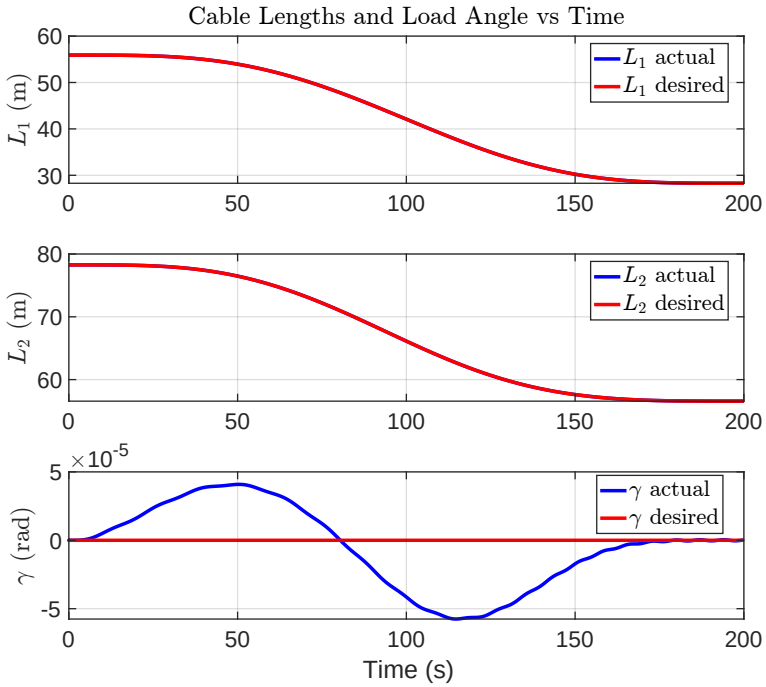

Figure 5.11: Case 2: Actual and desired cable lengths and load angle vs. time.

profiles, while the deviation between the actual and desired values of γ remains very small. The detailed tracking errors are illustrated in Fig. 5.12. The deviation is extremely small and gradually converges to zero, fully meeting the precision requirements of industrial installation standards. Compared with the tracking errors shown in Fig. 5.5 of Case1, the results are nearly identical, indicating that even under the asymmetric geometric configuration, the system can still achieve stable lifting and equivalent trajectory tracking performance.

Fig. 5.13 shows the velocity profiles of the two cables, clearly indicating that the maxi-

Table 5.3: Case 2 parameters of the DCC system.

Parameter and gain	**Symbol**	**Value / Unit**
Coordinate of the boom 1 anchor	(X_1, Y_1)	(20, 80) m
Coordinate of the boom 2 anchor	(X_2, Y_2)	(100, 100) m
Mass of the load	m	2000 kg
Half length of the load	d	10 m
Gravitational acceleration	g	9.81 m/s^2
Friction coefficients	F	$diag(0.1, 0.1, 0.05)$
Initial load coordinate	$(x(0),\ y(0))$	(55, 30) m
Final load coordinate	$(x(t_f),\ y(t_f))$	(50, 60) m
Total simulation duration	t_f	200 s
Maximum cable velocity	$V_{i,max}, i = 1, 2$	0.3 m/s
Coupling gains	$\eta_{i1}, i = 1, 2$	15
Coupling gains	$\eta_{2i}, i = 1, 2$	200
Proportional gain	$K_{pi}, i = 1, 2$	100
Integral gain	$K_{ij}, j = 1, 2$	0.8
Derivative gain	$K_{di}, i = 1, 2$	5

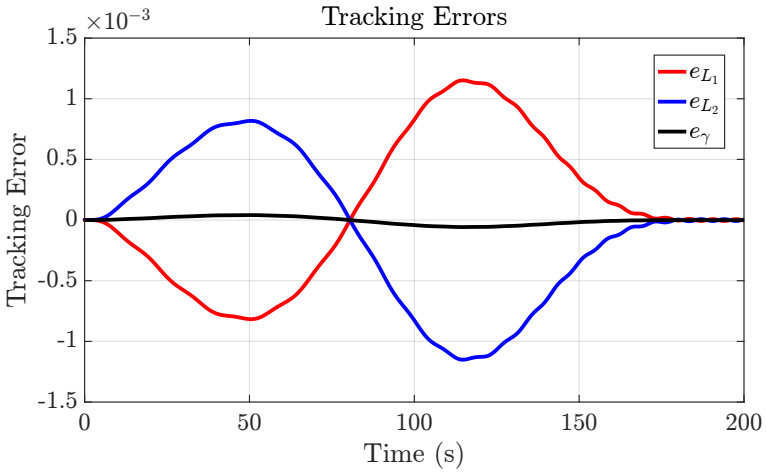

Figure 5.12: Case 2: Tracking errors between actual and desired cable lengths and load angle.

mum cable velocity constraint is fully respected throughout the motion. Meanwhile, Fig. 5.14 presents the time evolution of the load coordinates $x(t)$ and $y(t)$. Both trajectories exhibit smooth transitions without noticeable oscillations, and the load successfully reaches the prescribed target position at the end of the lifting process. Fig. 5.15 depicts the corresponding load trajectory in the Cartesian plane for the asymmetric configuration. Although the cranes are positioned asymmetrically, the reference trajectories of the cable lengths are designed to ensure that the load remains horizontal during the entire motion. As a result, the load follows a smooth curved path instead of a purely vertical line, which reflects the geometric asymmetry of

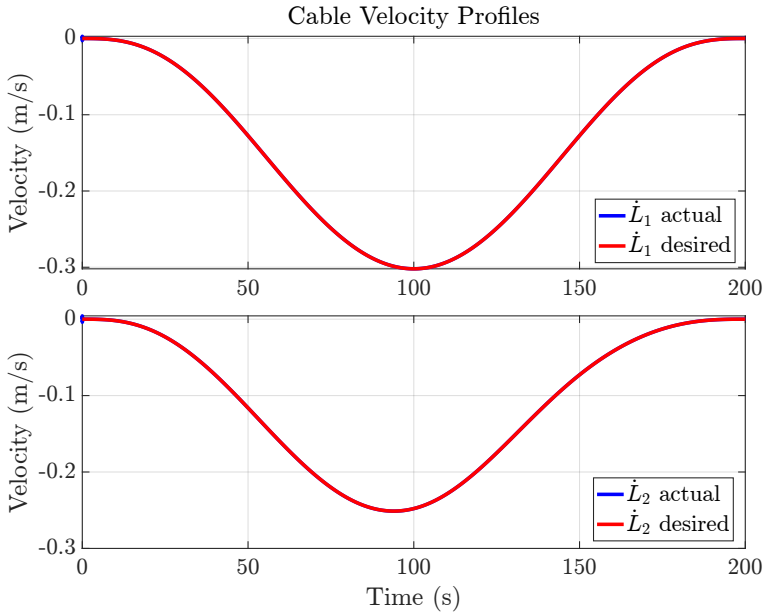

Figure 5.13: Case 2: Actual and desired cable velocity vs time.

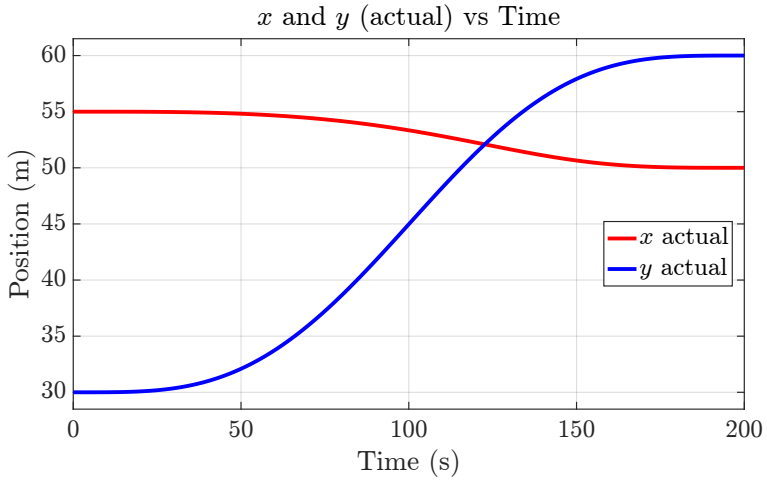

Figure 5.14: Case 2: Coordinate of the load vs. time

the system and the coupled variation of the two cable lengths required to maintain equilibrium. The time markers along the trajectory indicate that the motion starts and ends slowly while accelerating smoothly in the middle, consistent with the desired velocity profile. Fig. 5.16 reports the time evolution of the control inputs τ_1 and τ_2 for Case 2. Similarly to Case 1, after a short initial transient both inputs remain bounded and vary smoothly over the entire lifting interval, indicating a well conditioned control action without aggressive actuation. Compared with the symmetric scenario, the two control inputs no longer overlap exactly, reflecting the asymmetric reference generation adopted in Case 2. Nevertheless, their temporal profiles remain closely matched and exhibit a consistent long-term trend, showing that the control effort is properly distributed between the two actuators despite the geometric asymmetry. Overall,

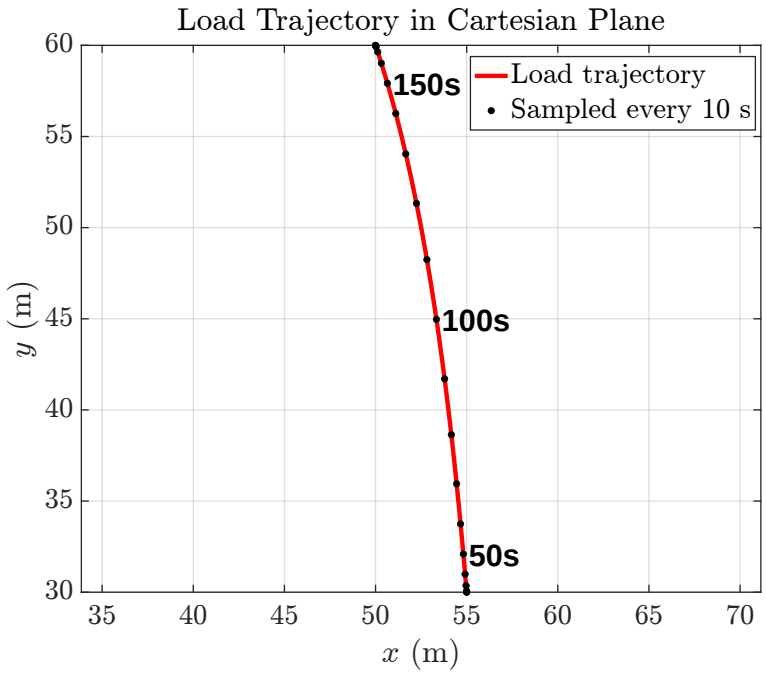

Figure 5.15: Case 2: Load trajectory in Cartesian plane.

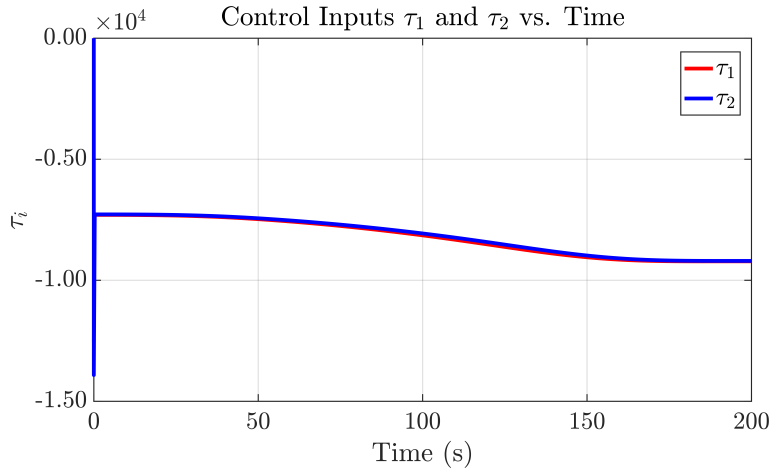

Figure 5.16: Case 1: Time evolution of the control inputs τ_1 and τ_2.

the behaviour of τ_1 and τ_2 is coherent with the load motion observed in Fig. 5.7 and confirms that the proposed control strategy preserves smooth and stable actuation also under asymmetric lifting conditions. These results demonstrate that the proposed trajectory generation method effectively guarantees horizontal lifting and smooth motion even under asymmetric crane configurations.

The simulation results of Case 2 demonstrate that even for a geometrically asymmetric dual crawler crane configuration, the proposed control strategy remains effective in suppressing load oscillations during the lifting process. It ensures smooth trajectory transitions of both the cables and the load while accurately reaching the desired final position at the prescribed time.

Taken together, the two case studies represent the vast majority of practical cooperative hoisting scenarios encountered in real operations. Hence, the proposed method can effectively enhance lifting efficiency while maintaining safe and stable operation of the dual crane system.

5.4.3 Case 3: Three Phase Hoisting Task with Load Rotation

In practical applications, some lifting tasks require not only a horizontal transfer of the load, but also a large rotation of its attitude during the maneuver. A representative example is the installation of a wind turbine tower segment, which is initially stored in a horizontal configuration on the ground or on supports and must be brought to a final vertical configuration at the installation site.

A typical operational procedure can be described as follows. At the beginning of the maneuver, the two crawler cranes are connected to the tower segment through cables that are not vertically aligned with the load. As a result, the initial geometric configuration corresponds to a horizontal orientation of the tower with a load angle $\gamma = 0$, as illustrated in Fig. 5.17.

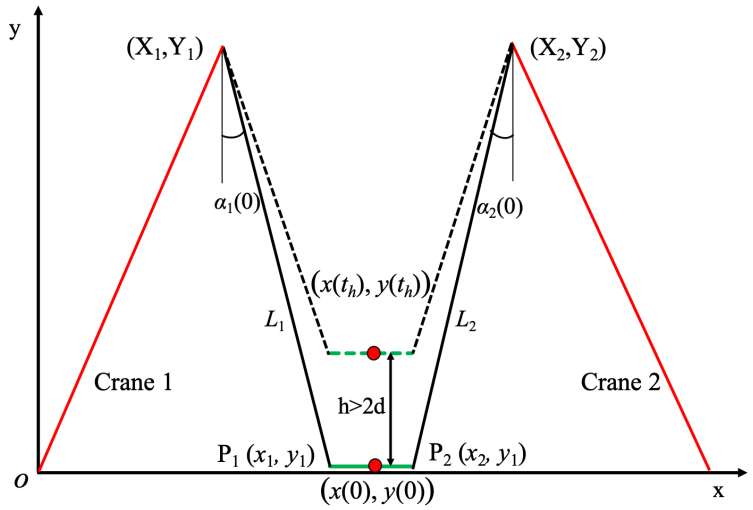

Figure 5.17: Case 3: Illustration of the initial horizontal lifting phase with clearance condition $h > 2d$.

In the first phase, both cranes lift in a coordinated manner by adjusting their cable lengths to raise the tower while maintaining a nearly horizontal attitude. The primary objective of this phase is to increase the vertical position of the tower until its height exceeds its own length. Under the geometric model adopted in this work, this condition can be expressed as $h > 2d$, which guarantees sufficient ground clearance and avoids interference with surrounding structures prior to the onset of rotation.

In the second phase, the rotation of the tower is performed. One crane cable is gradually lengthened, while the other is kept approximately constant or adjusted in a coordinated manner.

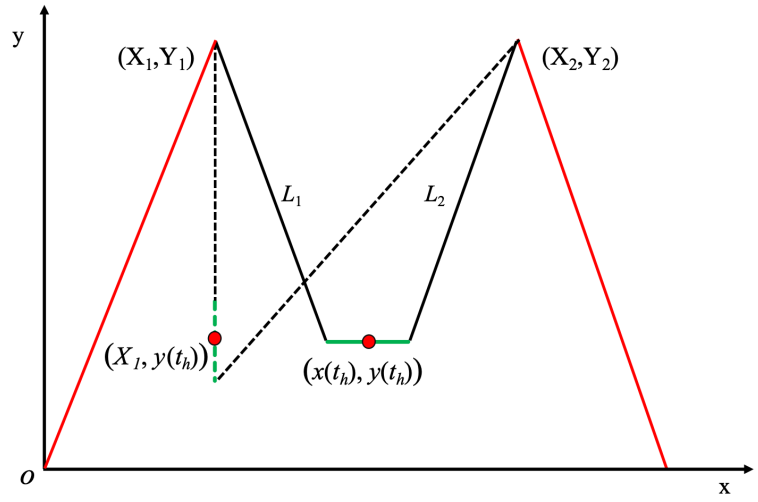

Figure 5.18: Case 3: Illustration of the rotation phase, in which the load angle transitions from $\gamma = 0$ to $\gamma = -\pi/2$ while maintaining the same initial and final vertical position.

This results in a smooth rotational motion of the tower about a moving instantaneous center, as illustrated in Fig. 5.18. Consequently, the load angle γ transitions smoothly from $\gamma = 0$ to $\gamma = -\pi/2$. The rotation phase is designed such that the initial and final vertical positions of the load coincide.

From an operational standpoint, this phase is required to remain quasi-static. The cable length variations must be sufficiently slow and smooth in order to limit angular accelerations and suppress excessive swing. This ensures that the dynamic loads acting on both cranes and on the tower segment remain within acceptable limits throughout the rotation process.

It is worth noting that the admissible workspace defined in Chapter 4 is an open set, which guarantees positive tension in both cables and well-defined equilibrium conditions. However, boundary configurations corresponding to $\gamma = \pm\pi/2$ can be interpreted as limiting cases of this workspace and are of direct relevance in practical installation tasks. In Case 3, the desired final configuration corresponds to such a boundary equilibrium, representing a fully upright tower. The reference trajectories are therefore designed so that the system evolves strictly within the interior of the admissible workspace during the lifting and rotation phases, while the boundary configuration is approached smoothly only at the final stage of the maneuver.

In the final phase of the maneuver, the tower reaches a fully upright configuration. Subsequently, the system performs a coordinated vertical hoisting motion toward the target installation position, as illustrated in Fig. 5.19. During this stage, both cranes remain connected to the load, and the cable lengths are adjusted in a coordinated manner to preserve the upright configuration and ensure a stable and controlled vertical motion.

The simulation of Case 3 is intended to further evaluate the versatility of the proposed control framework under a more demanding cooperative hoisting task. In contrast to the pre-

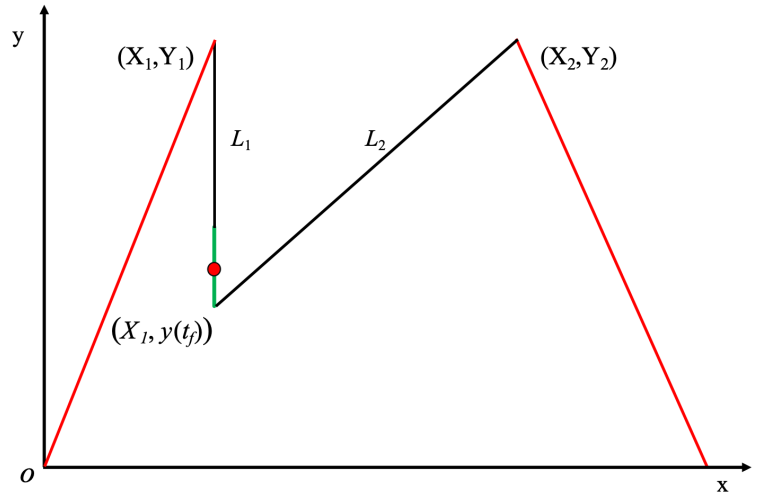

Figure 5.19: Case 3: Illustration of the final vertical hoisting phase with the load in an upright configuration.

vious cases, this scenario involves a combined maneuver consisting of horizontal lifting, large angle rotation, and subsequent vertical hoisting, which significantly increases the geometric complexity and operational difficulty of the system. Such a maneuver is representative of practical installation operations, for example in wind turbine tower erection, where both position regulation and attitude reorientation must be achieved in a coordinated and safe manner.

Owing to the increased complexity of the task and the strict safety requirements associated with large payload manipulation, the maneuver is designed to remain quasi-static throughout all phases. To this end, a relatively long simulation horizon of $t_f = 800, \mathrm{s}$ is adopted, allowing sufficiently smooth variations of the cable lengths and load angle. The simulation parameters and controller gains are reported in Table 5.4.

The simulation is carried out in MATLAB. Based on the specified initial and final coordinates of the load, the corresponding equilibrium configurations are first computed as follows

$$L_1(0) = 104.403, \quad L_2(0) = 104.403, \quad \gamma(0) = 0,$$

$$L_1(t_f) = 40, \quad L_2(t_f) = 100, \quad \gamma(t_f) = -\pi/2.$$

Fig.5.20 shows the time histories of the cable lengths $L_1(t)$, $L_2(t)$, and the load orientation angle $\gamma(t)$ for Case3. It can be observed that the actual cable length trajectories closely follow their corresponding reference profiles throughout the entire maneuver, including the lifting, rotation, and final vertical hoisting phases. The load orientation angle γ also exhibits accurate tracking performance, smoothly transitioning between different configurations as prescribed by the reference trajectory. The corresponding tracking errors are reported in Fig.5.21. Although

Table 5.4: Case 3 parameters of the DCC system.

Parameter and gain	**Symbol**	**Value / Unit**
Coordinate of the boom 1 anchor	(X_1, Y_1)	(20, 100) m
Coordinate of the boom 2 anchor	(X_2, Y_2)	(100, 100) m
Mass of the load	m	2000 kg
Half length of the load	d	10 m
Gravitational acceleration	g	9.81 m/s^2
Friction coefficients	F	$diag(0.1, 0.1, 0.05)$
Initial load coordinate	$(x(0),\ y(0))$	(60, 0) m
Final load coordinate	$(x(t_f),\ y(t_f))$	(20, 50) m
Total simulation duration	t_f	800 s
Maximum cable velocity	$V_{i,max}, i = 1, 2$	0.4 m/s
Coupling gains	$\eta_{i1}, i = 1, 2$	5
Coupling gains	$\eta_{2i}, i = 1, 2$	300
Proportional gain	$K_{pi}, i = 1, 2$	100
Integral gain	$K_{ij}, j = 1, 2$	0.8
Derivative gain	$K_{di}, i = 1, 2$	5

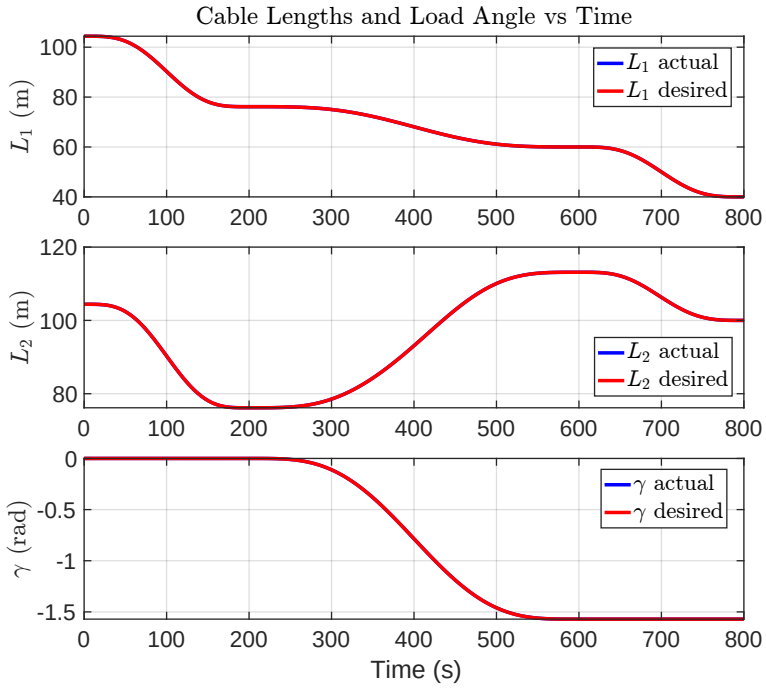

Figure 5.20: Case 3: Actual and desired cable lengths and load angle vs. time.

Case3 involves a more complex motion sequence combining vertical lifting and large-angle rotation, the tracking errors of both cable lengths and the load orientation remain bounded within a small range and gradually converge toward zero.

Fig.5.22 illustrates the time histories of the cable velocities in Case3. Despite the increased

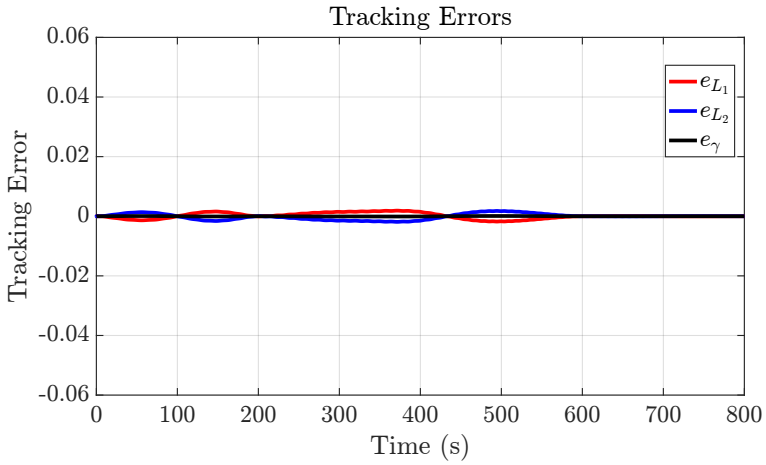

Figure 5.21: Case 3: Tracking errors between actual and desired cable lengths and load angle.

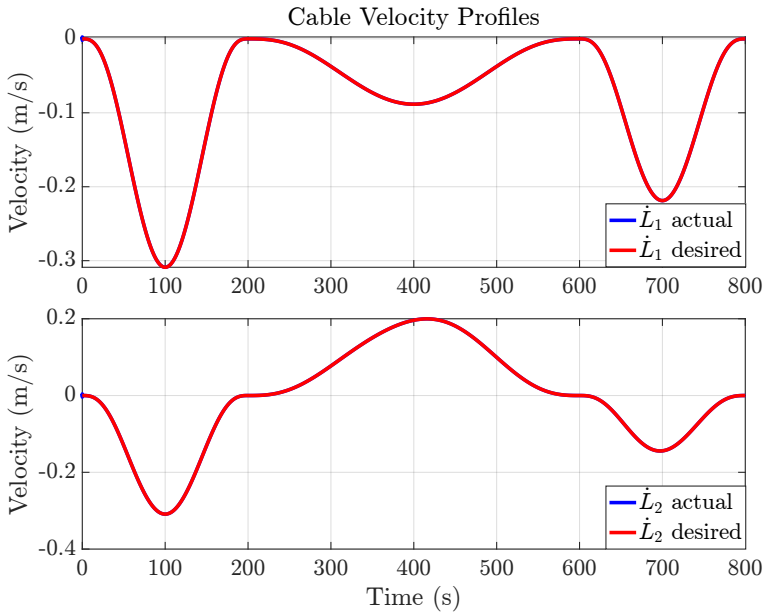

Figure 5.22: Case 3: Actual and desired cable velocity vs time.

maneuver complexity and extended operation time, both cable velocities accurately track their references and remain within the prescribed limits throughout the motion.

Meanwhile, Fig. 5.23 illustrates the time histories of the load coordinates $x(t)$ and $y(t)$. The horizontal and vertical motions exhibit smooth and continuous profiles over the entire maneuver, with no abrupt changes or oscillatory behavior. The load reaches the prescribed target position at the final time, confirming the effectiveness of the reference trajectory design and the closed-loop control performance. Fig. 5.24 shows the corresponding load trajectory in the Cartesian plane. The trajectory clearly reflects the three-phase maneuver, including the initial vertical lifting phase, the rotation phase with coupled horizontal and vertical motion, and the final vertical hoisting phase toward the installation position. The time markers along the

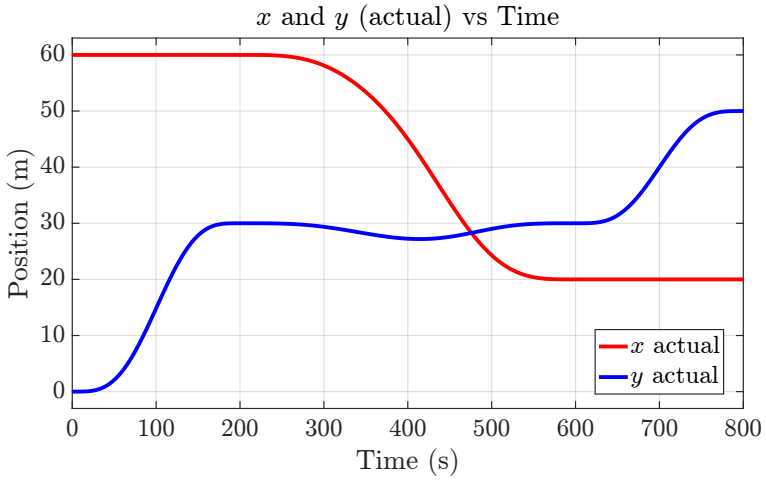

Figure 5.23: Case 3: Coordinate of the load vs time

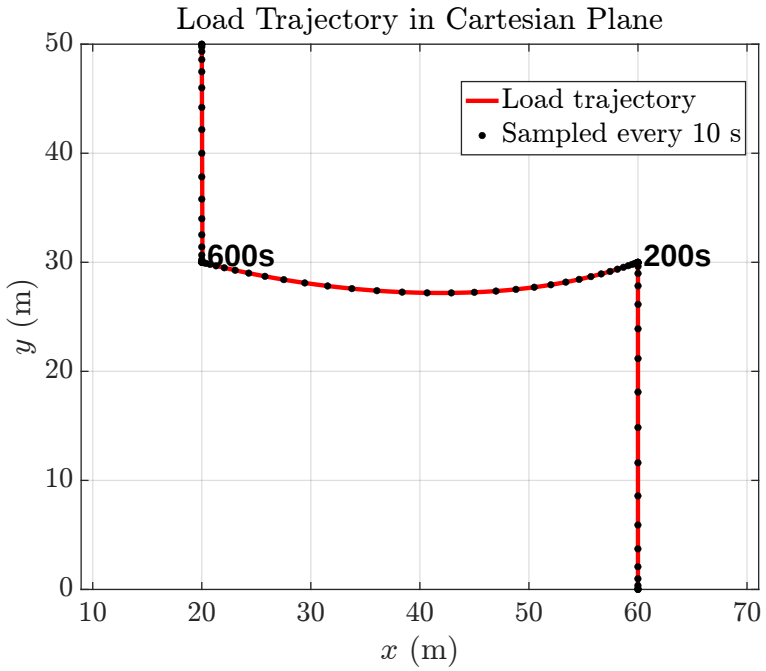

Figure 5.24: Case 3: Load trajectory in Cartesian plane.

trajectory indicate a slow start and stop with a smoother and faster motion in the intermediate phase, which is consistent with the adopted high-order polynomial velocity profiles. The resulting path is smooth and well coordinated, demonstrating that the proposed strategy can handle combined lifting and rotation tasks while maintaining stable and controlled motion.

Fig.5.25 reports the time evolution of the control inputs τ_1 and τ_2 for Case 3. Despite the increased task complexity involving sequential lifting, rotation, and final vertical hoisting, both control inputs remain bounded and exhibit smooth variations over the entire maneuver. After an initial transient, no abrupt changes or high frequency oscillations are observed, indicating that the proposed controller provides well conditioned actuation even under this more demanding

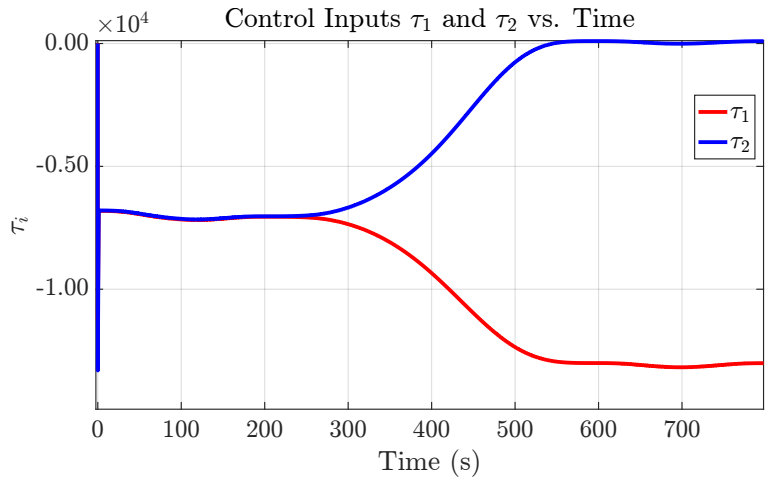

Figure 5.25: Case 3: Time evolution of the control inputs τ_1 and τ_2.

operating scenario.

Overall, the simulation results of Case 3 demonstrate the effectiveness and robustness of the proposed control strategy in handling a complex multi phase cooperative hoisting task. The controller successfully coordinates the cable length variations to achieve safe clearance, controlled rotation, and accurate vertical positioning, while maintaining smooth control inputs and small tracking errors. These results confirm that the proposed approach is suitable for practical cooperative hoisting operations that require combined lifting and large attitude reconfiguration under stringent safety constraints.

5.4.4 Performance Analysis

In order to clarify what it means for the DCC system to perform in an acceptable or good fashion, this section evaluates the behaviour of the controlled system under different reference generation strategies and different lifting speeds. The purpose is to assess whether the controller is able to ensure accurate tracking, limited load swing, and overall stable operation when the desired trajectories are varied.

All simulations are carried out using the same initial and final configurations adopted in Case 2, namely

$$(x(0), y(0), \gamma(0)) = (55\ \text{m}, 30\ \text{m}, 0\ \text{rad}), \qquad (x(t_f), y(t_f), \gamma(t_f)) = (50\ \text{m}, 60\ \text{m}, 0\ \text{rad}).$$

Thus, every experiment begins and ends at the same equilibrium positions as in the Case 2. In addition to the boundary conditions, all simulations share the same physical and modeling parameters used in Case 2, including the boom anchor coordinates, the geometric properties of the load, the friction coefficients, and the controller gains. This ensures that the only variations

among experiments arise from the choice of reference generation mode and the prescribed lifting duration.

To investigate the effect of lifting speed, four total durations are considered: $50\,\mathrm{s}$, $100\,\mathrm{s}$, $200\,\mathrm{s}$, and $400\,\mathrm{s}$. For each duration, four reference generation modes are tested in order to analyse how different types of desired trajectories influence tracking accuracy and load stability. This unified framework allows a systematic comparison of the controller performance across different speeds and reference designs, while keeping all other parameters unchanged.

The four modes differ in which desired signals are prescribed and which variables are recovered from static equilibrium at each time instant.

Mode A $(L_1 \mid y)$. In this mode, the primary desired trajectories $L_{1d}(t)$ and $y_d(t)$ are generated using the seventh–order polynomial procedure described in Algorithm 5. These trajectories satisfy zero initial and final velocity, acceleration, and jerk, ensuring a smooth evolution of the prescribed variables. The remaining desired variables $(L_{2d}(t), \gamma_d(t))$ are computed at each time instant from the *equilibrium equation*, which enforces the static force balance of the load. Since γ is not explicitly constrained in this mode, the resulting angle is determined purely by the geometry of the configuration, and therefore $\gamma_d(t) \neq 0$ in general.

Mode B $(L_1 \mid x)$. As in Mode A, the desired trajectories for $L_{1d}(t)$ and $x_d(t)$ are generated by the seventh–order polynomial profile of Algorithm 5. At each time instant, the variables $(L_{2d}(t), \gamma_d(t))$ are recovered by solving the *equilibrium equation*. Because the load angle is not directly imposed in this mode, the geometric relation leads to a non zero desired angle in general, i.e., $\gamma_d(t) \neq 0$, except for special symmetric cases.

Mode C $(x \mid y)$. In this mode, the desired trajectory $(x_d(t), y_d(t))$ is specified. As before, each of these two signals is generated using Algorithm 5 to ensure smoothness. The static equilibrium relation is then solved at each instant to obtain $(L_{1d}(t), L_{2d}(t), \gamma_d(t))$. Since the desired trajectory does not enforce horizontal lifting, the resulting angle $\gamma_d(t)$ typically deviates from zero except in symmetric configurations.

Mode D $(L_1 \mid \gamma)$. This mode corresponds exactly to the reference design adopted in Case 2. Here, the desired load angle is explicitly prescribed as $\gamma_d(t) = 0$ for all t, so the load is required to remain perfectly horizontal throughout the motion. A smooth trajectory for $L_{1d}(t)$ is generated using Algorithm 5, and the remaining cable length $L_{2d}(t)$ is computed at each time instant by solving the *equilibrium equation*. Since the desired angle is imposed directly, this is the only mode that guarantees horizontal lifting by construction.

The fundamental difference among the four reference generation modes lies in the choice of the variables whose desired trajectories are specified a priori. Each mode reflects a different operational objective that may arise in practical crane installation tasks, while the remaining variables are recovered by enforcing static equilibrium conditions.

Modes A and B are suitable for operations in which either the vertical or horizontal motion of the load is prioritized through the explicit specification of $y_d(t)$ or $x_d(t)$, respectively. These modes offer a structured way to regulate the load motion while allowing the load orientation to be determined implicitly by the system geometry. As a result, they are appropriate for lifting scenarios where strict orientation control is not required, but smooth force redistribution between the cranes is desired. Mode C directly prescribes the Cartesian trajectory of the load center and therefore provides the highest level of flexibility in specifying the desired installation path. This mode is particularly useful when the target position is defined in workspace coordinates. However, since the load orientation is not explicitly constrained, horizontal lifting is not guaranteed except in symmetric configurations. Mode D explicitly enforces a horizontal load orientation by prescribing $\gamma_d(t) = 0$ throughout the motion. This makes it the most suitable choice for installation tasks that require strict attitude control, such as precision assembly or alignment of elongated structures. The reduced flexibility in trajectory design is compensated by the guarantee of horizontal lifting by construction.

From a practical standpoint, the four modes do not represent competing approaches, but rather complementary reference design options. The appropriate mode can be selected according to the specific installation objective, such as prioritizing geometric accuracy, orientation constraints, or operational simplicity.

Two categories of performance indices are introduced.

1. Tracking performance. Tracking accuracy is quantified using two complementary metrics.

First, the *integral mean square error* (IMSE) is defined as

$$\textit{Track–IMSE} = \frac{1}{T}\int_0^T \left(e_{L_1}^2(t) + e_{L_2}^2(t)\right) \mathrm{d}t,$$

where $e_{L_1}(t) = L_1(t) - L_{1d}(t)$ and $e_{L_2}(t) = L_2(t) - L_{2d}(t)$ denote the tracking errors of the two cable lengths. Because the squared error amplifies larger deviations, this index provides a more informative measure of the overall quality of tracking, particularly in highlighting occasional larger discrepancies between the actual and desired trajectories.

Second, the *mean absolute error* (MAE) is retained, defined as

$$\textit{Track–MAE} = \frac{1}{T}\int_0^T \left(|e_{L_1}(t)| + |e_{L_2}(t)|\right) \mathrm{d}t.$$

This metric represents the average deviation between the actual and desired cable lengths over the entire maneuver.

Together, Track-IMSE and Track-MAE quantify both the magnitude and consistency of the tracking errors, and therefore directly reflect the accuracy with which the controller regulates the cable lengths and, consequently, the load position.

2. Load stability performance. Load stability is assessed by monitoring the tracking error of the load angle, $e_\gamma(t) = \gamma(t) - \gamma_d(t)$, using three complementary indices.

First, the integral mean square error (IMSE) is defined as

$$\gamma\text{–IMSE} = \frac{1}{T}\int_0^T e_\gamma^2(t)\,\mathrm{d}t,$$

which emphasises larger deviations and provides a global measure of the quality of angular tracking.

Second, the mean absolute error (MAE) is given by

$$\gamma\text{–MAE} = \frac{1}{T}\int_0^T |e_\gamma(t)|\,\mathrm{d}t,$$

representing the average deviation of the load angle from its desired value across the entire maneuver.

Finally, a *normalised peak error* is introduced as

$$\gamma\text{–PeakAvg} = \frac{1}{T}\max_{t\in[0,T]}|e_\gamma(t)|,$$

which provides a time–scaled measure of the maximum angular deviation and allows a fair comparison across maneuvers of different lifting durations.

Although $\gamma_d(t)$ is not identically zero in Modes A, B, and C, the desired angle profiles remain smooth and of small magnitude because they are generated from static equilibrium. In this setting, smaller values of γ–IMSE, γ–MAE, and γ–PeakAvg indicate reduced load swing and a more stable lifting motion.

The numerical results reported in Tables (5.5 - 5.9), together with the visual summaries in Fig. 5.26 and Fig. 5.27, reveal several consistent performance trends across the four reference generation modes.

- **Tracking accuracy.** The bar charts in Fig. 5.26, based on the Track-IMSE and Track-MAE indicators, show that Mode B achieves the smallest tracking errors for all hoisting durations. Across all metrics, Modes B and C form a clear high performance pair, both significantly outperforming Modes A and D. This behaviour is evident in both the Track-IMSE and Track-MAE tables, where Mode B consistently attains the lowest values, followed closely by Mode C. In contrast, Modes A and D exhibit very similar values and constitute a second group with relatively larger errors, although their performance remains satisfactory in an absolute sense. For all modes, the Track-IMSE and Track-MAE values decrease monotonically as the lifting duration increases, indicating improved performance for slower motions.

Table 5.5: Track–IMSE performance for various reference modes and hoisting speeds.

Mode	Metric	50 s	100 s	200 s	400 s
A $(L_1 \mid y)$	Track-IMSE	2.30e-4	1.18e-5	7.11e-7	4.38e-8
B $(L_1 \mid x)$	Track-IMSE	**6.39e-5**	**3.74e-6**	**2.41e-7**	**1.65e-8**
C $(x \mid y)$	Track-IMSE	7.84e-5	4.43e-6	2.81e-7	1.87e-8
D $(L_1 \mid \gamma)$	Track-IMSE	2.28e-4	1.19e-5	7.22e-7	4.48e-8

- **Load angle stability.** Fig. 5.27 and the angle performance tables (γ-IMSE, γ-MAE, and γ-PeakAvg) confirm the same trend. Among the non-horizontal lifting modes (A, B, and C), Mode B again achieves the smallest accumulated and peak angle deviations. Modes B and C display nearly identical values in all angle metrics, representing the most favourable behaviour among the three non-horizontal lifting modes. Mode D is the only mode that enforces $\gamma_d(t) = 0$ for the entire motion and therefore uniquely guarantees strictly horizontal lifting, although its numerical angle errors are slightly larger than those of Modes B and C. As in the tracking case, all angle metrics improve consistently when the hoisting duration increases from 50 s to 400 s.

- **Overall system performance.** Across all reference modes and lifting durations, the DCC system exhibits stable and smooth closed-loop behaviour. The figures show that both cable length errors and angle deviations evolve without abrupt changes, and the monotonic reduction of all performance indicators with increasing hoisting time confirms the robustness of the controller for slower motions. The consistent grouping of the four modes, with

  $$\text{Mode B} \approx \text{Mode C} \;>\; \text{Mode A} \approx \text{Mode D},$$

  highlights that, under the asymmetric geometric configuration considered in this study, Modes B and C provide the most suitable reference geometry for accurate and stable lifting, while Mode D remains the appropriate choice when strictly horizontal lifting must be maintained for all t.

In summary, both the numerical indicators and the graphical trends confirm that the DCC system achieves high tracking precision, small load-angle deviations, and robust closed-loop behaviour under all reference generation modes. The strong agreement between the quantitative metrics and the visual results further demonstrates the effectiveness and reliability of the proposed control strategy.

Table 5.6: Track–MAE performance for various reference modes and hoisting speeds.

Mode	Metric	50 s	100 s	200 s	400 s
A $(L_1 \mid y)$	Track-MAE	1.67e-2	3.87e-3	9.49e-4	2.36e-4
B $(L_1 \mid x)$	Track-MAE	**9.33e-3**	**2.27e-3**	**5.78e-4**	**1.51e-4**
C $(x \mid y)$	Track-MAE	1.02e-2	2.51e-3	6.34e-4	1.64e-4
D $(L_1 \mid \gamma)$	Track-MAE	1.64e-2	3.84e-3	9.43e-4	2.35e-4

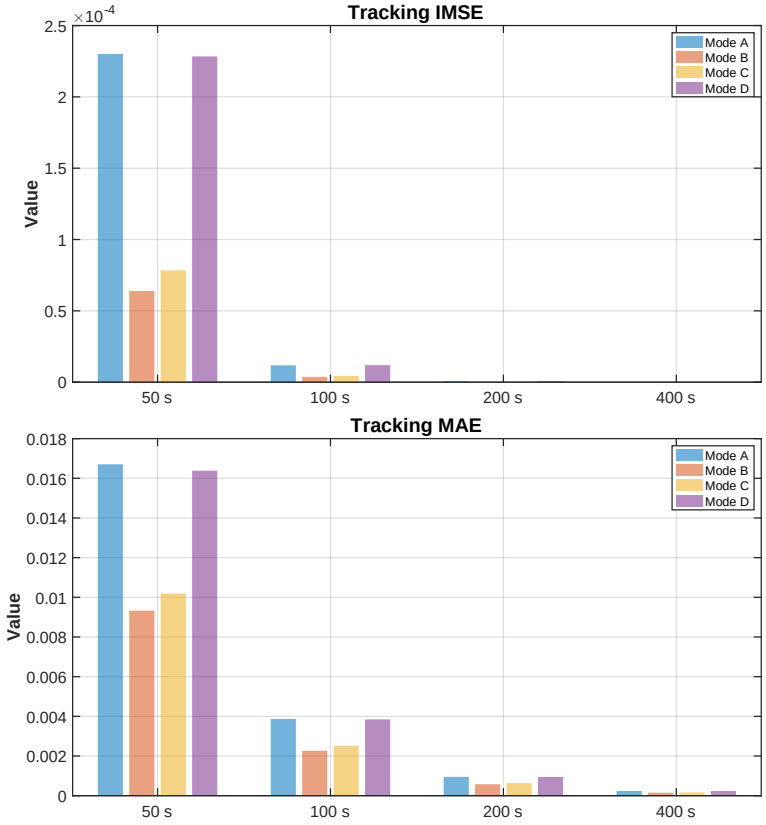

Figure 5.26: Visual comparison of tracking performance for various reference modes and hoisting speeds.

Table 5.7: Load stability γ-IMSE performance for various reference modes and hoisting speeds.

Mode	Metric	50 s	100 s	200 s	400 s
A $(L_1 \mid y)$	γ-IMSE	2.88e-7	1.48e-8	8.88e-10	5.48e-11
B $(L_1 \mid x)$	γ-IMSE	**8.00e-8**	**4.68e-9**	**3.02e-10**	**2.06e-11**
C $(x \mid y)$	γ-IMSE	9.80e-8	5.53e-9	3.51e-10	2.34e-11
D $(L_1 \mid \gamma)$	γ-IMSE	2.86e-7	1.49e-8	9.02e-10	5.60e-11

Table 5.8: Load stability γ-MAE performance for various reference modes and hoisting speeds.

Mode	Metric	50 s	100 s	200 s	400 s
A $(L_1 \mid y)$	γ-MAE	4.18e-4	9.67e-5	2.37e-5	5.90e-6
B $(L_1 \mid x)$	γ-MAE	**2.33e-4**	**5.67e-5**	**1.45e-5**	**3.78e-6**
C $(x \mid y)$	γ-MAE	2.55e-4	6.28e-5	1.59e-5	4.09e-6
D $(L_1 \mid \gamma)$	γ-MAE	4.10e-4	9.61e-5	2.36e-5	5.87e-6

Table 5.9: Load stability γ-PeakAvg performance for various reference modes and hoisting speeds.

Mode	Metric	50 s	100 s	200 s	400 s
A $(L_1 \mid y)$	γ-PeakAvg	2.21e-5	2.30e-6	2.77e-7	3.40e-8
B $(L_1 \mid x)$	γ-PeakAvg	**1.10e-5**	**1.29e-6**	**1.60e-7**	**2.08e-8**
C $(x \mid y)$	γ-PeakAvg	1.13e-5	1.33e-6	1.64e-7	2.11e-8
D $(L_1 \mid \gamma)$	γ-PeakAvg	2.32e-5	2.32e-6	2.88e-7	3.58e-8

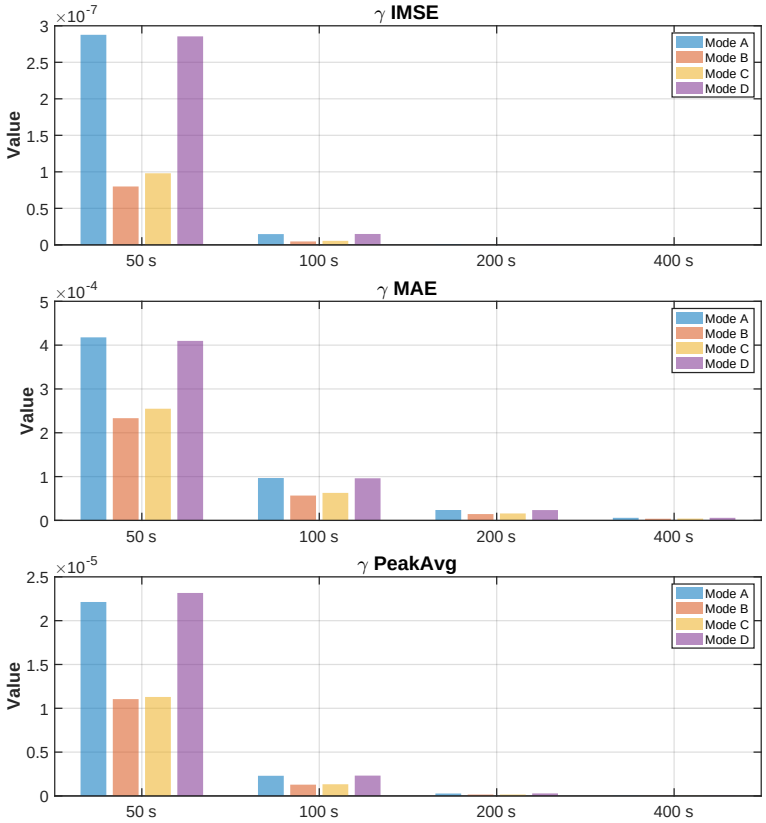

Figure 5.27: Visual comparison of load stability performance for various reference modes and hoisting speeds.

Chapter 6

Conclusions and Future Works

6.1 Conclusions

This dissertation investigates the modeling, planning, and control of DCC cooperative hoisting systems, focusing on improving load stability, and operational safety during cooperative lifting tasks. The main contributions of the work are summarized as follows.

(1) **Cooperative hoisting of DCCs with a point-mass load under rope velocity constraint**

This work develops a DCC system with a point-mass load and proposes a trajectory generation method that regulates rope lengths to ensure that the suspended load follows a predefined path while satisfying velocity constraints. To further enhance lifting efficiency under rope velocity constraints, an adaptive velocity shaping method is developed as an improvement over the direct approximation approach. Instead of relying on a predefined velocity profile, this method dynamically adjusts the motion velocity in real time based on the instantaneous load position. By introducing a position dependent adjustment function, the horizontal velocity of the load is continuously adapted according to the dynamic cable factors. This adaptive mechanism guarantees full compliance with the cable velocity constraints while maintaining a relatively high operational speed and achieving smooth deceleration as the load approaches the target position. Simulation results demonstrate that the proposed adaptive velocity shaping method significantly reduces the total lifting time compared with the original method.

(2) **Dynamic modeling and order reduction of DCCs with rigid rod load**

A complete nonlinear dynamic model of the DCC system with rigid-rod has been developed based on the Euler–Lagrange formulation. An accurate nonlinear dynamic model of a dual crawler crane system lifting a rigid-rod load is developed without adopting any linearization assumptions. The proposed model fully captures the geometric coupling and closed-chain characteristics of the system. By systematically applying motion constraints, the original tenth-order dynamic model (5 DOF) is reduced to a simplified sixth-order form (3 DOF) while preserving the essential nonlinear behaviors. This reduction significantly decreases the complexity of subsequent controller design and provides a reference for the modeling of similar constrained mechanical systems.

(3) **Design of coordinated reference trajectories**

A trajectory planning framework has been proposed to ensure that the desired motion of the DCC system satisfies equilibrium state at each time instant. The reference trajectories for cable lengths and load attitude are generated in cable space by connecting the initial and final equilibrium configurations through smooth velocity profiles. Simulation results confirm that the proposed approach maintains accurate load leveling and keeps sway within acceptable limits in all case studies.

(4) **Development of coordinated control strategy**

A coupled control strategy has been designed to achieve high-precision synchronization between the two cranes. The controller ensures that the actual motion of the system asymptotically converges to the desired reference trajectories, while effectively suppressing load swing and vibration. The proposed control law has been validated through numerical simulations, showing strong robustness against parameter variations.

6.2 Future Works

Although the present study provides a systematic theoretical and simulation framework for DCC cooperative hoisting, several research topics remain open for future investigation.

(1) **Theoretical analysis of closed-loop system stability**

The present work provides a heuristic discussion on the stability of the proposed closed-loop system. A rigorous theoretical stability analysis under the constrained closed-loop dynamics defined by $e_1(t) = e_2(t) = 0$ remains an open challenge due to the complexity and strong nonlinear coupling of the DCC system. This aspect will be addressed in future research. Possible directions include the development of a formal Lyapunov-based framework or other analytical tools capable of characterizing the stability properties of the reduced dynamics on the manifold defined by the error constraints. Such analysis would provide a deeper theoretical foundation for the proposed control scheme and strengthen its guarantees beyond the heuristic arguments presented in this study.

(2) **Alternative control strategies for cooperative hoisting**

Although the present study provides a systematic theoretical and simulation framework for DCC cooperative hoisting, several research topics remain open for future investigation. In addition to the PID based coupled control strategy adopted in this study, the availability of a detailed dynamic model of the cooperating crane system also enables the exploration of alternative control synthesis approaches. Future work may investigate both linear and nonlinear control techniques that have been widely discussed in the literature.

Linear methods, such as linear quadratic or gain scheduled control schemes, could provide systematic design procedures and local performance guarantees based on linearized or parameter-dependent representations of the system dynamics, although their effectiveness may be limited under large configuration variations. Nonlinear control approaches, including feedback linearization, passivity based control, or nonlinear model predictive control, may better exploit the intrinsic nonlinear structure of the crane dynamics and explicitly handle operational constraints, at the cost of increased computational complexity and a stronger reliance on accurate modeling and state estimation. A systematic comparison of these alternative strategies with the PID based approach, from both performance and implementation perspectives, represents an interesting direction for future research.

(3) **Real time trajectory planning and optimization**

To improve on site adaptability, future work should develop computationally efficient trajectory generation algorithms that can operate in real time. Combining optimization-based planning with machine learning may enable adaptive control under uncertain environments.

(4) **Extension to three-dimensional cooperative hoisting**

Future research will consider extending the current two-dimensional DCC system model to a fully three-dimensional framework. In this setting, the spatial motion of each crane and the suspended load will be represented in all six degrees of freedom. Such an extension would not only provide a more realistic description of practical lifting scenarios, but also enable the investigation of multi-crane cooperative hoisting involving more than two cranes, thereby offering a more general foundation for large scale coordinated lifting operations.

Bibliography

[1] E. M. Abdel-Rahman, A. H. Nayfeh, and Z. N. Masoud, "Dynamics and control of cranes: A review," *Journal of Vibration and Control*, 2003.

[2] A. Elsabbagh, E. El-Kashif, and S. Sayed, "Failure investigation of fractured crane crawler track plate," *Engineering Failure Analysis*, 2024.

[3] C. Vazquez, J. Collado, and L. Fridman, "Control of a parametrically excited crane: A vector lyapunov approach," *IEEE Transactions on Control Systems Technology*, 2013.

[4] K. Zavari, G. Pipeleers, and J. Swevers, "Gain-scheduled controller design: Illustration on an overhead crane," *IEEE Transactions on Industrial Electronics*, 2013.

[5] M. Zhang, "Finite-time model-free trajectory tracking control for overhead cranes subject to model uncertainties, parameter variations and external disturbances," *Transactions of the Institute of Measurement and Control*, 2019.

[6] X. Wu and X. He, "Nonlinear energy-based regulation control of three-dimensional overhead cranes," *IEEE Transactions on Automation Science and Engineering*, 2016.

[7] C. Cui, A. Giua, and A. Pisano, "Cooperative hoisting with two crawler cranes under rope-velocity constraints," in *2023 IEEE Conference on Control Technology and Applications (CCTA)*, pp. 978–983, 2023.

[8] H. Ouyang, J. Hu, G. Zhang, L. Mei, and X. Deng, "Decoupled linear model and s-shaped curve motion trajectory for load sway reduction control in overhead cranes with double-pendulum effect," *Proceedings of the Institution of Mechanical Engineers, Part C: Journal of Mechanical Engineering Science*, 2018.

[9] X. Liu, C.-Y. Su, Z. Li, and F. Yang, "Adaptive neural-network-based active control of regenerative chatter in micromilling," *IEEE Transactions on Automation Science and Engineering*, 2017.

[10] L. U. Odhner, R. R. Ma, and A. M. Dollar, "Open-loop precision grasping with underactuated hands inspired by a human manipulation strategy," *IEEE Transactions on Automation Science and Engineering*, 2013.

[11] P. S. Thakar, P. K. Trivedi, B. Bandyopadhyay, and P. S. Gandhi, "A new nonlinear control for asymptotic stabilization of a class of underactuated systems: An implementation to slosh-container problem," *IEEE/ASME Transactions on Mechatronics*, 2017.

[12] X. Li, Y. Pan, G. Chen, and H. Yu, "Continuous tracking control for a compliant actuator with two-stage stiffness," *IEEE Transactions on Automation Science and Engineering*, 2016.

[13] H. Pan, W. Sun, H. Gao, and X. Jing, "Disturbance observer-based adaptive tracking control with actuator saturation and its application," *IEEE Transactions on Automation Science and Engineering*, 2015.

[14] Q. Xu, "Precision motion control of piezoelectric nanopositioning stage with chattering-free adaptive sliding mode control," *IEEE Transactions on Automation Science and Engineering*, 2016.

[15] Z. Zhang, M. Liu, C.-Y. Lee, and J. Wang, "The quay crane scheduling problem with stability constraints," *IEEE Transactions on Automation Science and Engineering*, 2018.

[16] B. Lu, Y. Fang, and N. Sun, "Modeling and nonlinear coordination control for an under-actuated dual overhead crane system," *Automatica*, 2018.

[17] A. D. López Rojas, O. Mendoza-Trejo, E. A. Padilla-García, D. Ortiz Morales, C. A. Cruz-Villar, and P. La Hera, "Design, rapid manufacturing and modeling of a reduced-scale forwarder crane with closed kinematic chain," *Mechanics Based Design of Structures and Machines*, 2022.

[18] X. Kang, L. Chai, and H. Liu, "Anti-swing and positioning for double-pendulum tower cranes using improved active disturbance rejection controller," *International Journal of Control, Automation and Systems*, 2023.

[19] Z. Liu, T. Yang, Y. Fang, and N. Sun, "Predefined-time synchronous control for 3-d dual-boom cranes: Same-plane synchronization, different-plane coordination, and payload regulation," *IEEE/ASME Transactions on Mechatronics*, 2025.

[20] Z. Liu, T. Yang, Y. Fang, and N. Sun, "Optimal trajectory-based control of 3-d dual rotary cranes for payload dynamic regulation in complex environments," *IEEE Transactions on Artificial Intelligence*, vol. 5, pp. 5452–5464, Nov 2024.

[21] J. K. Eberharter and K. Schneider, "Control for synchronizing multi-crane lifts," in *2010 IEEE International Conference on Control Applications*, pp. 1301–1306, 2010.

[22] Z. Liu, T. Yang, Q. Wu, Y. Wu, H. Chen, and N. Sun, "Dynamic modeling for 3-dimensional cooperative dual boom cranes: Analysis and verification," in *2024 IEEE 18th International Conference on Advanced Motion Control (AMC)*, pp. 1–6, Feb 2024.

[23] W. Huang, W. Niu, X. Zhou, and W. Gu, "Anti-sway control of variable rope length container crane based on phase plane trajectory planning," *Journal of Vibration and Control*, 2023.

[24] X. Jin and W. Xu, "Neural network based adaptive robust synchronous control of double-lift overhead crane considering input saturation," *Journal of the Franklin Institute*, 2024.

[25] A. Jianqi, Z. Lusha, X. Yonghua, and W. Min, "Path planning method for dual cranes considering the changes of load ratio," in *2015 34th Chinese Control Conference (CCC)*, pp. 2774–2779, July 2015.

[26] S. Qian, B. Zi, and H. Ding, "Dynamics and trajectory tracking control of cooperative multiple mobile cranes," *Nonlinear Dynamics*, 2015.

[27] N. Najafizadeh Sari, H. Jahanshahi, and M. Fakoor, "Adaptive fuzzy pid control strategy for spacecraft attitude control," *International Journal of Fuzzy Systems*, 2019.

[28] W. Tang, R. Ma, W. Wang, T. Xu, and H. Gao, "Adaptive pid control of overhead cranes based on isoa–nn," *International Journal of Dynamics and Control*, 2024.

[29] Y. Xiong, Q. Wei, Z. Yang, P. Li, and H. Cheng, "Collision-free path planning for dual-arm robots based on improved rrt," in *2024 IEEE 7th Advanced Information Technology, Electronic and Automation Control Conference (IAEAC)*, vol. 7, pp. 433–439, 2024.

[30] Q. Jiang and V. Kumar, "The direct kinematics of objects suspended from cables," in *Proceedings of the ASME 2010 International Design Engineering Technical Conferences and Computers and Information in Engineering Conference (IDETC/CIE)*, vol. 2: 34th Annual Mechanisms and Robotics Conference, Parts A and B, pp. 193–202, Aug. 2010.

[31] M. S. A. D. Ali, N. R. Babu, and K. Varghese, "Collision free path planning of co-operative crane manipulators using genetic algorithm," *Journal of Computing in Civil Engineering*, 2005.

[32] C. Sun, X. Dong, and J. Li, "Cross-coupled sliding mode synchronous control for a double lifting point hydraulic hoist," *Sensors*, 2023.

[33] F. A. Leban, J. Diaz-Gonzalez, G. G. Parker, and W. Zhao, "Inverse kinematic control of a dual crane system experiencing base motion," *IEEE Transactions on Control Systems Technology*, 2015.

[34] O. Barbarisi, C. Del Vecchio, and A. Parisio, "Multiple cranes control with task deadlines and priority constraints," in *2007 European Control Conference (ECC)*, pp. 2031–2038, 2007.

[35] R. Souissi and A. Koivo, "Modelling and control of two co-operating planar cranes," in *[1993] Proceedings IEEE International Conference on Robotics and Automation*, pp. 957–962 vol.3, May 1993.

[36] X. Wang, H. Wang, and D. Wu, "Interactive simulation of crawler crane's lifting based on opengl," in *International Design Engineering Technical Conferences and Computers and Information in Engineering Conference*, vol. 43277, pp. 1533–1540, 2008.

[37] Y. Li, X. Xi, J. Xie, and C. Liu, "Study and implementation of a cooperative hoisting for two crawler cranes," *Journal of Intelligent Robotic Systems*, 2015.

[38] J.-C. Kim, H. Lee, Y. Kim, and D. Lee, "Automatic dual crane cooperative path planning based on multiple rrt algorithm for narrow path finding scenario," *IEEE Access*, 2024.

[39] H. Chen and N. Sun, "Nonlinear control of underactuated systems subject to both actuated and unactuated state constraints with experimental verification," *IEEE Transactions on Industrial Electronics*, 2019.

[40] Z. Liu, Y. Fu, N. Sun, T. Yang, and Y. Fang, "Collaborative antiswing hoisting control for dual rotary cranes with motion constraints," *IEEE Transactions on Industrial Informatics*, 2021.

[41] P. Cai, I. Chandrasekaran, J. Zheng, and Y. Cai, "Automatic path planning for dual-crane lifting in complex environments using a prioritized multiobjective pga," *IEEE Transactions on Industrial Informatics*, 2017.

[42] D. E. Chang, "Stabilizability of controlled lagrangian systems of two degrees of freedom and one degree of under-actuation by the energy-shaping method," *IEEE Transactions on Automatic Control*, vol. 55, no. 8, pp. 1888–1893, 2010.

[43] H. Ouyang, X. Xu, and G. Zhang, "Tracking and load sway reduction for double-pendulum rotary cranes using adaptive nonlinear control approach," *International Journal of Robust and Nonlinear Control*, 2019.

[44] J. Huang, E. Maleki, and W. Singhose, "Dynamics and swing control of mobile boom cranes subject to wind disturbances," *IET Control Theory & Applications*, vol. 7, no. 9, pp. 1187–1195, 2013.

[45] G. Li, X. Ma, Z. Li, P. Guo, and Y. Li, "Kinematic coupling-based trajectory planning for rotary crane system with double-pendulum effects and output constraints," *Journal of Field Robotics*, vol. 40, no. 2, pp. 289–305, 2023.

[46] E. Arnold, J. Neupert, O. Sawodny, and K. Schneider, "Trajectory tracking for boom cranes based on nonlinear control and optimal trajectory generation," in *2007 IEEE International Conference on Control Applications*, pp. 1444–1449, 2007.

[47] Y.-C. Chang, W.-H. Hung, and S.-C. Kang, "A fast path planning method for single and dual crane erections," *Automation in Construction*, 2012.

[48] P. Cai, I. Chandrasekaran, J. Zheng, and Y. Cai, "Automatic path planning for dual-crane lifting in complex environments using a prioritized multiobjective pga," *IEEE Transactions on Industrial Informatics*, 2017.

[49] D. Zameroski, G. Starr, J. Wood, and R. Lumia, "Rapid swing-free transport of nonlinear payloads using dynamic programming," *Journal of Dynamic Systems, Measurement, and Control*, vol. 130, p. 041001, 06 2008.

[50] E. Maleki and W. Singhose, "Swing dynamics and input-shaping control of human-operated double-pendulum boom cranes," *Journal of Computational and Nonlinear Dynamics*, 2012.

[51] P. Cai, I. Chandrasekaran, J. Zheng, and Y. Cai, "Automatic path planning for dual-crane lifting in complex environments using a prioritized multiobjective pga," *IEEE Transactions on Industrial Informatics*, 2017.

[52] C. Yang, Z. Li, R. Cui, and B. Xu, "Neural network-based motion control of an underactuated wheeled inverted pendulum model.," *IEEE Transactions on Neural Networks and Learning Systems*, 2014.

[53] L. Wang, X. Lai, Q. Meng, and M. Wu, "Effective control method based on trajectory optimization for three-link vertical underactuated manipulators with only one active joint," *IEEE Transactions on Cybernetics*, 2021.

[54] X. Zheng, H. Li, C. K. Ahn, and D. Yao, "Nn-based fixed-time attitude tracking control for multiple unmanned aerial vehicles with nonlinear faults," *IEEE Transactions on Aerospace and Electronic Systems*, 0015.

[55] S. Yang and B. Xian, "Energy-based nonlinear adaptive control design for the quadrotor uav system with a suspended payload," *IEEE Transactions on Industrial Electronics*, 2019.

[56] K. Chen, J. Yi, and D. Song, "Gaussian-process-based control of underactuated balance robots with guaranteed performance," *IEEE Transactions on Robotics*, 0016.

[57] S. Yuslinda, H. I. Jaafar, R. Ghazali, and N. Abdul Razif, "The effects of auto-tuned method in pid and pd control scheme for gantry crane system," *International Journal of Soft Computing and Engineering*, vol. 4, pp. 121–125, 01 2015.

[58] N. Sun, T. Yang, Y. Fang, Y. Wu, and H. Chen, "Transportation control of double-pendulum cranes with a nonlinear quasi-pid scheme: Design and experiments," *IEEE Transactions on Systems, Man, and Cybernetics: Systems*, 2018.

[59] L. Zey, D. Briskorn, and N. Boysen, "Twin-crane scheduling during seaside workload peaks with a dedicated handshake area," *Journal of Scheduling*, 2021.

[60] Z. Liu, Y. Fu, N. Sun, T. Yang, and Y. Fang, "Collaborative antiswing hoisting control for dual rotary cranes with motion constraints," *IEEE Transactions on Industrial Informatics*, 2021.

[61] Z. Liu, N. Sun, T. Yang, G. Liu, and Y. Fang, "Assembly-oriented finite-time coordinated control of underactuated dual rotary cranes for payload position and attitude regulation," *IEEE Transactions on Automation Science and Engineering*, 2023.

[62] X. Shen, J. An, and T. Terano, "Calculation method of load distribution for two-crane cooperative lift," in *2018 37th Chinese Control Conference (CCC)*, pp. 7851–7855, 2018.

[63] P. Cai, Y. Cai, I. Chandrasekaran, and J. Zheng, "Parallel genetic algorithm based automatic path planning for crane lifting in complex environments," *Automation in Construction*, vol. 62, pp. 133–147, 2016.

[64] D. Qian, S. Tong, and S. Lee, "Fuzzy-logic-based control of payloads subjected to double-pendulum motion in overhead cranes," *Automation in Construction*, 2016.

[65] D. Liu, J. Yi, D. Zhao, and W. Wang, "Adaptive sliding mode fuzzy control for a two-dimensional overhead crane," *Mechatronics*, 2005.

[66] L.-H. Lee, C.-H. Huang, S.-C. Ku, Z.-H. Yang, and C.-Y. Chang, "Efficient visual feedback method to control a three-dimensional overhead crane," *IEEE Transactions on Industrial Electronics*, 2013.

[67] M. I. Solihin, n. Wahyudi, and A. Legowo, "Fuzzy-tuned pid anti-swing control of automatic gantry crane," *Journal of Vibration and Control*, 2009.

[68] S. H. Jung and K. H. Kim, "Load scheduling for multiple quay cranes in port container terminals," *Journal of Intelligent Manufacturing*, 2006.

[69] P. Hirsch, A. Palfi, and M. Gronalt, "Solving a time constrained two-crane routing problem for material handling with an ant colony optimisation approach: an application in the roof-tile industry," *International Journal of Production Research*, 2012.

[70] A. V. Perig, A. N. Stadnik, A. A. Kostikov, and S. V. Podlesny, "Research into 2d dynamics and control of small oscillations of a cross-beam during transportation by two overhead cranes," *Shock and Vibration*, 2017.

[71] A. M. Abdullahi, Z. Mohamed, H. Selamat, H. R. Pota, M. Zainal Abidin, F. Ismail, and A. Haruna, "Adaptive output-based command shaping for sway control of a 3d overhead crane with payload hoisting and wind disturbance," *Mechanical Systems and Signal Processing*, vol. 98, pp. 157–172, 2018.

[72] S. Garrido, M. Abderrahim, A. Gimenez, R. Diez, and C. Balaguer, "Anti-swinging input shaping control of an automatic construction crane," *IEEE Transactions on Automation Science and Engineering*, vol. 5, no. 3, pp. 549–557, 2008.

[73] J. Peng, J. Huang, and W. Singhose, "Payload twisting dynamics and oscillation suppression of tower cranes during slewing motions," *Nonlinear Dynamics*, vol. 98, no. 2, pp. 1041–1048, 2019.

[74] R. Mar, A. Goyal, V. Nguyen, T. Yang, and W. Singhose, "Combined input shaping and feedback control for double-pendulum systems," *Mechanical Systems and Signal Processing*, 2017.

[75] S. Sano, H. Ouyang, H. Yamashita, and N. Uchiyama, "Lmi approach to robust control of rotary cranes under load sway frequency variance," *Journal of System Design and Dynamics*, vol. 5, no. 7, pp. 1402–1417, 2011.

[76] N. Uchiyama, H. Ouyang, and S. Sano, "Simple rotary crane dynamics modeling and open-loop control for residual load sway suppression by only horizontal boom motion," *Mechatronics*, vol. 23, no. 8, pp. 1223–1236, 2013.

[77] J. Vaughan, J. Yoo, N. Knight, and W. Singhose, "Multi-input shaping control for multi-hoist cranes," in *2013 American Control Conference*, pp. 3449–3454, June 2013.

[78] X. Zhao and J. Huang, "Distributed-mass payload dynamics and control of dual cranes undergoing planar motions," *Mechanical Systems and Signal Processing*, 2019.

[79] Z. N. Masoud and K. A. Alhazza, "Frequency-modulation input shaping control of double-pendulum overhead cranes," *Journal of Dynamic Systems, Measurement, and Control*, vol. 136, p. 021005, 12 2013.

[80] S. Arabasi and Z. Masoud, "Frequency-modulation input-shaping strategy for double-pendulum overhead cranes undergoing simultaneous hoist and travel maneuvers," *IEEE Access*, vol. 10, pp. 44954–44963, 2022.

[81] D. Chwa, "Sliding-mode-control-based robust finite-time antisway tracking control of 3-d overhead cranes," *IEEE Transactions on Industrial Electronics*, 2017.

[82] L. A. Tuan and S.-G. Lee, "Sliding mode controls of double-pendulum crane systems," *Journal of Mechanical Science and Technology*, 2013.

[83] G. Bartolini, A. Pisano, E. Punta, and E. Usai, "A survey of applications of second-order sliding mode control to mechanical systems," *International Journal of Control*, 2003.

[84] Q. H. Ngo and K.-S. Hong, "Sliding-mode antisway control of an offshore container crane," *IEEE/ASME Transactions on Mechatronics*, vol. 17, no. 2, pp. 201–209, 2012.

[85] N. B. Almutairi and M. Zribi, "Sliding mode control of a three-dimensional overhead crane," *Journal of Vibration and Control*, vol. 15, no. 11, pp. 1679–1730, 2009.

[86] G. Bartolini, A. Pisano, and E. Usai, "Second-order sliding-mode control of container cranes," *Automatica*, vol. 38, no. 10, pp. 1783–1790, 2002.

[87] M. Zhang, X. Ma, X. Rong, X. Tian, and Y. Li, "Adaptive tracking control for double-pendulum overhead cranes subject to tracking error limitation, parametric uncertainties and external disturbances," *Mechanical Systems and Signal Processing*, 2016.

[88] N. Sun, T. Yang, H. Chen, Y. Fang, and Y. Qian, "Adaptive anti-swing and positioning control for 4-dof rotary cranes subject to uncertain/unknown parameters with hardware experiments," *IEEE Transactions on Systems, Man, and Cybernetics: Systems*, 2019.

[89] W. Yu, M. A. Moreno-Armendariz, and F. O. Rodriguez, "Stable adaptive compensation with fuzzy cmac for an overhead crane," *Information Sciences*, 2009.

[90] A. T. Le and S.-G. Lee, "3d cooperative control of tower cranes using robust adaptive techniques," *Journal of the Franklin Institute*, 2017.

[91] O. Sawodny, H. Aschemann, and S. Lahres, "An automated gantry crane as a large workspace robot," *Control Engineering Practice*, 2002.

[92] S. H. Zabihifar, H. Navvabi, and A. S. Yushchenko, "Dual adaptive neural network controller for underactuated systems," *Robotica*, 2021.

[93] Y. Chu, V. Æsøy, S. Ehlers, and H. Zhang, "Integrated multi-domain system modelling and simulation for offshore crane operations," *Ship Technology Research*, 2015.

[94] L. Zhao, M.-I. Roh, and S.-H. Ham, "Antisway control of a crane on an offshore support vessel based on the hardware-in-the-loop simulation," *International Journal of Offshore and Polar Engineering*, 2018.

[95] D. Liu and W. Guo, "Tracking control for an underactuated two-dimensional overhead crane," *Journal of Applied Research and Technology*, 2012.

[96] T.-S. Wu, M. Karkoub, W.-S. Yu, C.-T. Chen, M.-G. Her, and K.-W. Wu, "Anti-sway tracking control of tower cranes with delayed uncertainty using a robust adaptive fuzzy control," *Fuzzy Sets and Systems*, 2016.

[97] S. Zabihifar and A. Yuschenko, "Hybrid force/position control of a collaborative parallel robot using adaptive neural network," in *Interactive Collaborative Robotics* (A. Ronzhin, G. Rigoll, and R. Meshcheryakov, eds.), (Cham), pp. 280–290, Springer International Publishing, 2018.

[98] P. Hamill, *A Student's Guide to Lagrangians and Hamiltonians*. Cambridge, UK: Cambridge University Press, 2014.

[99] A. Fasano and S. Marmi, *Analytical Mechanics: An Introduction*. Oxford, UK: Oxford University Press, 2006.

[100] K. J. Åström and T. Hägglund, *PID Controllers: Theory, Design, and Tuning*. Research Triangle Park, NC, USA: Instrument Society of America, 2nd ed., 2006.

[101] W. Rudin, *Principles of Mathematical Analysis*. New York: McGraw-Hill, 3rd ed., 1976.

[102] S. Lang, *Analysis I*. Reading, Massachusetts: Addison-Wesley, 2nd ed., 1986.

[103] I. Shah and F. U. Rehman, "Smooth second order sliding mode control of a class of underactuated mechanical systems," *IEEE Access*, vol. 6, pp. 7759–7771, 2018.

[104] J. G. Ziegler and N. B. Nichols, "Optimum settings for automatic controllers," *Transactions of the American society of mechanical engineers*, vol. 64, no. 8, pp. 759–765, 1942.

[105] K. J. Åström and T. Hägglund, *Advanced PID control*. ISA-The Instrumentation, Systems and Automation Society, 2006.

[106] S. Shahruz and S. Behtash, "Design of controllers for linear parameter-varying systems by the gain scheduling technique," *Journal of Mathematical Analysis and Applications*, vol. 168, no. 1, pp. 195–217, 1992.

[107] J. S. Shamma, *Analysis and Design of Gain Scheduled Control Systems*. PhD thesis, Massachusetts Institute of Technology, Cambridge, MA, 1988.

[108] J. S. Shamma and M. Athans, "Guaranteed properties of gain scheduled control for linear parameter-varying plants," *Automatica*, vol. 27, no. 3, pp. 559–564, 1991.

[109] G. Corriga, A. Giua, and G. Usai, "An implicit gain-scheduling controller for cranes," *IEEE Transactions on Control Systems Technology*, vol. 6, no. 1, pp. 15–20, 1998.

Acknowledgment

I would like to express my sincere gratitude to all those who have supported me during my PhD period.

First and foremost, I wish to thank my supervisors, Prof. Alessandro Giua and Prof. Alessandro Pisano, for their patient and insightful guidance throughout my doctoral studies. Whenever I encountered difficulties, they always provided valuable advice and constructive suggestions. Prof. Giua has been remarkably patient in explaining complex problems in a clear and accessible way, which greatly helped me deepen my understanding. His constant encouragement has given me confidence and motivation to make steady progress, and I am also deeply grateful for the personal support he offered during my life in Cagliari. Prof. Pisano's guidance has been equally meticulous and well structured. He taught me how to approach and solve problems step by step, and his advice on both research practice and academic writing has been invaluable. From them, I have learned how to think creatively and critically. It has truly been an honor and a privilege to complete my PhD under their supervision.

I would also like to express my heartfelt gratitude to my parents, Xiaozong Cui and Jianping Mao, whose unconditional love and support have made this achievement possible. They have always encouraged me to pursue my goals and comforted me whenever I faced difficulties or pressure. I am also deeply grateful to my brother, Chenxi Cui, and my sister in law, Ruirui Zhang, for their constant understanding, encouragement, and support throughout this journey. Together, they are my strongest support and my eternal source of strength.

My deepest appreciation goes to my girlfriend, Ms. Sinan Zhang, for her love, care, and constant encouragement. She has been my emotional anchor, always offering understanding and support whenever I felt discouraged or exhausted.

Finally, I would like to thank all the members of our laboratory team, Wenjie Zhao, Tianyu Liu, Yike Li, Tao Meng, Zohreh Shahrouei, and Marco Ledda for their kind help and companionship. Their support made my time in Cagliari much easier and far less lonely.

Cagliari, November 2025

Chenhao Cui